



Title	3D Tomography of Ionospheric Anomalies immediately before and after Large Earthquakes
Author(s)	Muafiry, Ihsan Naufal
Citation	北海道大学. 博士(理学) 甲第14645号
Issue Date	2021-09-24
DOI	10.14943/doctoral.k14645
Doc URL	<a href="http://hdl.handle.net/2115/83579">http://hdl.handle.net/2115/83579</a>
Type	theses (doctoral)
File Information	Ihsan_Naufal_Muafiry.pdf



[Instructions for use](#)

# **3D Tomography of Ionospheric Anomalies**

## **immediately before and after Large Earthquakes**

(巨大地震直前直後の電離圏異常の三次元トモグラフィー)



By

**Ihsan Naufal Muafiry**

Supervisor: Prof. Kosuke Heki

A dissertation submitted in partial fulfillment

of the requirements for the degree of

Doctor of Philosophy

Department of Natural History Science

Graduate School of Science, Hokkaido University

September 2021

## Table of contents

Abstract .....	5
Acknowledgments.....	7
Chapter 1: Introduction .....	9
1.1 GNSS for Positioning.....	9
1.2 GNSS for Ionospheric Studies .....	10
1.3 Ionospheric Structure .....	12
1.4 Solid Earth and Ionosphere .....	14
1.5 Ionospheric Disturbance due to the Sea Surface Motion .....	16
1.6 Earthquake Precursors in Ionosphere.....	18
1.7 3D Tomography for Ionospheric Electron Density Anomalies .....	19
1.8 Research Objectives .....	20
Chapter 2: Data and Method.....	21
2.1 GNSS Network in Japan .....	21
2.2 GNSS Network in South Korea .....	22
2.3 GNSS Networks in South America.....	24
2.4 GNSS-TEC Method .....	25
2.5 Strategies to Isolate Anomalies from GNSS-TEC Data .....	28
2.6 Ionospheric 3D Tomography Method.....	29

Chapter 3: 3D Tomography of the Ionospheric Anomalies immediately before Earthquakes: The 2011 Tohoku-oki Earthquake .....	35
3.1 Introduction: History of Debate .....	36
3.2 Data set.....	39
3.3 Data Processing Strategy .....	40
3.3 Resolution tests .....	49
3.4 Tomography results .....	53
3.5 Growth and polarity balances of the preseismic anomalies.....	62
3.6 Discussion on the physical mechanism of the preseismic anomalies .....	63
Chapter 4: 3D Tomography of the Ionospheric Anomalies Before the 2010 Maule Earthquake, Chile: Comparison with the 2011 Tohoku-oki and 2015 Illapel Earthquake .....	68
4.1 Introduction: Structure of preseismic ionospheric anomalies.....	69
4.2 Data set.....	70
4.3 Data processing strategy .....	72
4.4 Resolution test.....	73
4.5 Tomography result.....	76
4.6 Comparison with the 2011 Tohoku-oki and 2015 Illapel Earthquakes .....	83
Chapter 5: 3D Tomography of the Ionospheric Anomalies after Earthquakes: The 2011 Tohoku-oki Earthquake .....	86

5.1	Introduction: Tsunamigenic ionospheric anomalies .....	87
5.2	Data set.....	87
5.3	Data processing strategy .....	87
5.4	Resolution tests .....	89
5.5	Tomography result.....	91
5.6	Physical mechanism of post-seismic anomalies .....	91
5.7	Origin of variety of waveforms.....	92
	Chapter 6: Conclusions and Recommendation .....	94
6.1	Conclusions.....	94
6.2	Recommendation .....	97

# 1 **Abstract**

2           A dense network of ground global navigation satellite system (GNSS) receivers detected  
3 ionospheric total electron content (TEC) changes starting ~40 minutes before the 2011 Tohoku-  
4 oki ( $M_w$  9.0) earthquake around the ruptured fault, together with the long-lasting postseismic TEC  
5 drop. In this study, I robustly estimate three-dimensional (3D) distribution of both pre- and post-  
6 seismic ionospheric anomalies of the 2011  $M_w$  9.0 Tohoku-oki and the 2010  $M_w$  8.8 Maule  
7 earthquakes by tomographic inversions of electron density anomalies. For the 2011 case, I set up  
8 more than 6,000 blocks, as large as  $1.0^\circ$  (east-west)  $\times$   $0.9^\circ$  (north-south)  $\times$  60 km (vertical), over  
9 the Japanese Islands, the Sea of Japan, and the Korean Peninsula, up to 870 km altitude. I used  
10 slant-TEC residuals obtained using 8 satellites and 1,493 ground stations as inputs to the 3D  
11 tomographic inversion. For the Maule earthquake, TEC data are obtained from 6 GNSS satellites  
12 and 89 ground stations mainly in Chile and Argentina. I set up  $>3,500$  blocks, with the size of  $1.0^\circ$   
13 (east-west)  $\times$   $1.2^\circ$  (north-south)  $\times$  75 km (vertical) for altitudes 75-750 km. I adopted objective  
14 standards in determining reference curves of TEC from which the anomalies are defined. I  
15 regularized the inversion by introducing two different constraints, the continuity constraint and  
16 constraints around zero with altitude-dependent allowances. Performances of the 3D tomography  
17 have been confirmed by various resolution tests for artificial patterns.

18           I compare the spatial and temporal distribution of the 3D structure of ionospheric electron  
19 density anomalies immediately before these two megathrust earthquakes together with those of  
20 another large earthquake (the 2015  $M_w$  8.3 Illapel) studied by He and Heki (2018). The results of  
21 the three cases showed that the preseismic ionospheric anomalies have following common  
22 features; (1) they are composed of pairs of low-altitude positive and high-altitude negative electron  
5

23 density anomalies, (2) they occur above the land area close to the submarine faults, and (3) they  
24 have clear onsets a few tens of minutes before earthquakes (~40 min before 2011 Tohoku-oki, and  
25 Maule, and ~20 minutes before the Illapel earthquakes) and grow with decaying rates.

26 I hypothesize the physical process consistent with such 3D structure as follows. Electric  
27 fields made by surface positive charges reach the ionosphere. The field generates electromotive  
28 forces and makes electrons move down along geomagnetic fields, and this upward current makes  
29 eastward/westward magnetic field in regions to the south/north of the epicenter before earthquakes  
30 in northern/southern hemisphere. The current will continue until the induced electric field cancels  
31 the external field made by surface charges, making the electric potential uniform along the  
32 magnetic field. The current will depend on the along-field component of the external electric field  
33 and the density of free electrons as a function of altitude. The nonuniform electric currents would  
34 result in convergence/divergence of electrons and make positive/negative electron density  
35 anomalies at the lower/higher ionosphere along the magnetic field, the structure consistent with  
36 those found for these three earthquakes by 3D tomography. I will also compare strengths and  
37 dimensions of the electron density anomalies before these three earthquakes and discuss future  
38 perspective of preseismic ionospheric anomalies.

39

## 40 **Acknowledgments**

41 In the name of Allah, God, the greatest one,

42 First of all, I praise to Allah subhanahuwata'ala for the things He has given to me. Since in  
43 the last three years period of my study, it is not only a journey of achieving a highest degree, but  
44 also is becoming my greatest experience ever in my life. Indeed, the second place for all of these,  
45 I would acknowledge my parents who have always been supporting and praying for me to go  
46 further just for the sake of knowledge. Third place is without a doubt, I thank to my little family  
47 (my wife and my children) who have been accompanying and supporting my journey in Japan as  
48 well as coloring my new life.

49 Over the three years, an incredible number of people have been helping me a lot in my  
50 journey. They deserve the gratitude of a thousand pages. First, I would like to express my sincere  
51 gratitude to Prof. Kosuke Heki, my supervisor, who has given me opportunity to become greater  
52 and smarter researcher. I learned many lessons and all of those are really valuable for my carrier  
53 path. He taught me about programming with its technical aspects, making a presentation,  
54 presenting slides, writing a scientific paper, and gave me chances to speak at international  
55 conferences. Sensei inspires me, and I could not have written this thesis without that inspiration.  
56 Thanks again sensei as always.

57 My sincere gratitude to Prof. Masato Furuya, Prof. Kiyoshi Yomogida, Prof. Kazunori  
58 Yoshizawa, and Dr. Yoichiro Takada for the advices delivered to my study during weekly solid-  
59 earth science seminar or after the seminar. Those are definitely encouraging me to become better

60 and better in scientific field. Also, my colleagues at Space Geodesy and Seismology Laboratories.  
61 I received many new perspectives of earth-sciences after discussing with them.

62 I thank the Geospatial Information Authority (GSI) for GEONET data (available from  
63 [terras.gsi.go.jp](http://terras.gsi.go.jp)) and Electric Navigation Research Institute (ENRI) for the inter-frequency bias  
64 data for GEONET stations (access [www.enri.go.jp](http://www.enri.go.jp) or write to Takeyasu Sakai [sakai@enri.go.jp](mailto:sakai@enri.go.jp) to  
65 obtain the bias). I also thank Byung-Kyu Choi, Korea Astronomy and Space Science Institute, for  
66 the Korean RINEX data files on March 11, 2011. One needs to write to [bkchoi@kasi.re.kr](mailto:bkchoi@kasi.re.kr) to access  
67 the Korean data. I thank Dr. He Liming, Northeast University, for helpful comments. It is also  
68 grateful to have GIM data from University of Berne, Switzerland. Thanks for providing them.

69 And finally, I thank to The Ministry of Education, Culture, Sports, Science and Technology  
70 (MEXT) who supports me financially during my PhD study in Hokkaido University.

71

## 72 **Chapter 1: Introduction**

### 73 **1.1 GNSS for Positioning**

74           The era of precise positioning system available worldwide started by the launches of the  
75 global navigation satellite system (GNSS) satellites in late 1980s. The Global Positioning Systems  
76 (GPS), maintained by the United States, is the first GNSS with a constellation of satellites orbiting  
77 the earth at altitude ~20,000 km. GPS is designed to extract the positions and velocities of moving  
78 objects in three-dimensional (3D) space continuously all over the world regardless of weather and  
79 time. Such information used to be only for military purposes and closed for civilian services.  
80 Nowadays, the technology is available for everyone, thus the position of any objects around the  
81 globe can be obtained using various GNSS including GPS.

82           There are several GNSS newer than GPS. The Russian GNSS, called Globalnoya  
83 Navigatsionnaya Sputnikovaya Sistema (GLONASS) is orbiting the earth at altitudes somewhat  
84 lower than those of GPS, ~19,000 km above the earth's surface. Galileo (European Navigation  
85 System) flies at ~23,000 km altitude whereas some of the Chinese GNSS satellites (Beidou, BDS)  
86 and the Japanese navigation satellites (Quasi-Zenith Satellite System, QZSS) employ much higher  
87 geostationary and quasi-zenith orbits, respectively. Wherever they are, all the GNSS satellites  
88 transmit microwave signals to earth to enable global navigation.

89           By measuring distances between an object (equipped with a GNSS receiver) and satellites,  
90 we can exactly tell where the object is. GNSS satellites transmit digital information about e.g.  
91 satellite orbits, clocks, as well as the satellite condition, using two L-band microwave carriers,  
92 which are often called L1 and L2 (and sometimes additional L5).

93           The national datum for surveying and mapping in a country is often maintained by GNSS,  
94 for example by building control points with precise GNSS surveying. The latitude and longitude  
95 measured by GNSS at one control point are defined on a reference ellipsoid of the earth, and the  
96 height can be directly measured relative to the ellipsoid instead of the local mean sea level. The  
97 standard ellipsoidal model widely used for GNSS is World Geodetic System 1984 (WGS-84). By  
98 establishing ties to reference systems, GNSS has improved the accuracy and consistency with the  
99 national datum so that it can be used for further scientific applications.

100           The microwave signals from GNSS satellites face delays caused by two layers of the  
101 earth's atmosphere before they reach receivers on the ground. The first layer is the ionosphere  
102 (ionized upper atmosphere) and the second is the troposphere (both water vapor and dry  
103 atmosphere). Atmospheric delays that occur in microwaves cause serious positioning errors, and  
104 precise positioning by GNSS needs to consider these atmospheric delays in processing the GNSS  
105 data. On the other hand, existence of such delays in the microwave signals enables us to study  
106 changes in these two layers. This thesis makes use of the atmospheric delays, especially those in  
107 the ionosphere, to investigate the dynamics within the ionosphere.

## 108 **1.2 GNSS for Ionospheric Studies**

109           Total Electron Content (TEC) signifies the number of electrons within a column of  $1 \text{ m}^2$   
110 along the signal path in the ionosphere and is expressed with TEC unit (TECU, 1 TECU equivalent  
111 to  $10^{16}$  electrons/ $\text{m}^2$ ). It is an integration of electron density,  $n_e (s)$  along line-of-sight (LoS)  
112 connecting the satellite with the ground receiver as shown in equation (1).

113

114 
$$TEC = \int_{satellite}^{receiver} n_e(s) ds \quad (1)$$

115 TEC is a useful quantity to indicate the total amount of free electrons in the ionosphere. A  
116 convenient way to measure TEC is to utilize GNSS data, using a technique called GNSS-TEC or  
117 GPS-TEC. Further details of the ionosphere and the GPS-TEC technique will be explained later.  
118 In comparison with conventional methods like ionosondes, GNSS-TEC method has much better  
119 resolution both in space and time in regions where dense GNSS networks are available (Heki,  
120 2021).

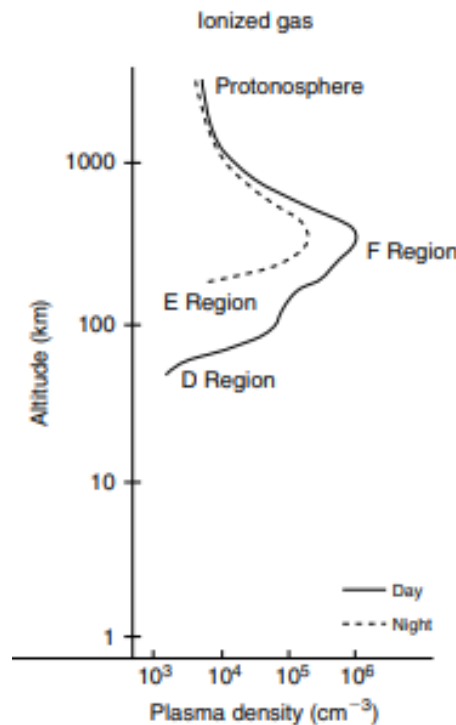
121 GNSS-TEC technique has been playing an important role in studying ionospheric  
122 disturbances of space weather origin. Such disturbances include the large scale travelling  
123 ionospheric disturbances (LSTID) and medium scale travelling ionospheric disturbances (MSTID)  
124 in the mid-latitude region (e.g. Saito, 1998; Otsuka et al., 2011), as well as the sporadic-E,  
125 extremely high electron density patches occurring in the E-region of the ionosphere (Muafiry and  
126 Heki, 2018).

127 The GNSS-TEC method has enabled researcher to detect ionospheric disturbances  
128 triggered by lithospheric phenomena. For example, those associated with large earthquakes are  
129 known as the coseismic ionospheric disturbance (CID) (Calais and Minster, 1995; Heki and Ping,  
130 2005; Cahyadi and Heki, 2015). Acoustic waves excited by coseismic vertical crustal movements  
131 propagate upward and disturb the ionosphere as CID. I will further discuss this topic later in the  
132 thesis. In addition earthquakes, Heki (2006) detected ionospheric disturbances excited by acoustic  
133 waves by a 2004 Vulcanian volcanic explosion of the Asama volcano in central Japan. Kundu et

134 al. (2021) detected ionospheric disturbances caused by an artificial explosion in 2020 August in  
135 Beirut, Lebanon.

### 136 1.3 Ionospheric Structure

137 Ionosphere is the uppermost layer of the earth's atmosphere where significant amounts of  
138 neutral gasses are ionized due to solar radiation. Such photoionization produces electrons and  
139 positive ions (Kelley, 2009). The ionosphere ranges in altitude from ~80 km up to several  
140 hundreds of kilometers. They are divided into the D (~80 km), E (~100 km), and F (higher) regions.  
141 The peak electron density occurs at altitude of ~300 km in the F-region (Kelley, 2009). During the  
142 night, D and E regions become ambiguous, but they emerge again soon after sunrise.



143

144 **Figure 1.** Typical vertical profile of ionosphere (Kelley, 2009)

145           In 1931, Sydney Chapman, in USA, presented a mathematical model for the formation of  
146 ionized layers based on the photoionization processes. He is the first who derived the distribution  
147 of ionization as a function of height based on absorption of solar radiation. In Chapter 2.6, I  
148 introduce his simple expression of electron production as functions of height and the solar zenith  
149 angle. The Chapman function will be used in constraining the solution around zero in the 3D  
150 tomography calculations in this study.

151           The existence of the ionosphere was recognized for the first time when radio waves are  
152 realized to propagate over large distances. In 1882, Balfour Stewart in Scotland suggested the  
153 existence of an ionized region in the atmosphere by measuring the variation of geomagnetic field  
154 using a compass. In 1901, Guglielmo Marconi, Italy, sent radio waves from England to Canada  
155 demonstrating that the ionosphere acted like a mirror for high frequency (HF) radio waves.

156           Ionosphere has been extensively utilized for long-distance radio communications using HF  
157 radio waves, which are bounced back to ground and enable global-scale propagation. Higher  
158 frequency (e.g. VHF) radio waves penetrate ionosphere and cannot be used for  
159 telecommunications. Owing to the usefulness of the ionosphere for public, people have long been  
160 monitoring ionosphere with various sensors including ionosondes, satellites, and radars.

161           I consider that recent discoveries of ionospheric disturbances related to large earthquakes  
162 greatly enhanced the implication of the ionospheric studies. Among others, I pick up a recent topic  
163 of ionospheric anomalies preceding large earthquakes. Considering a long unsuccessful history of  
164 earthquake prediction, TEC changes immediately before large earthquakes found shortly after the  
165 2011 Tohoku-oki earthquake by Heki (2011) could become a key phenomenon toward the

166 operation of practical earthquake prediction and mitigation of earthquake disasters in the future. I  
167 will discuss the link between earthquakes and ionosphere in more detail in Chapter 1.6.

#### 168 **1.4 Solid Earth and Ionosphere**

169 The lithosphere is the uppermost part of the solid earth from the surface (0 km altitude)  
170 way down to the depth ~100 km. Lithosphere is divided into tectonic plates, which consist of  
171 oceanic and continental plates. The asthenosphere below the lithosphere allows tectonic plates to  
172 move around and interact with each other causing variety of phenomena along their boundaries.

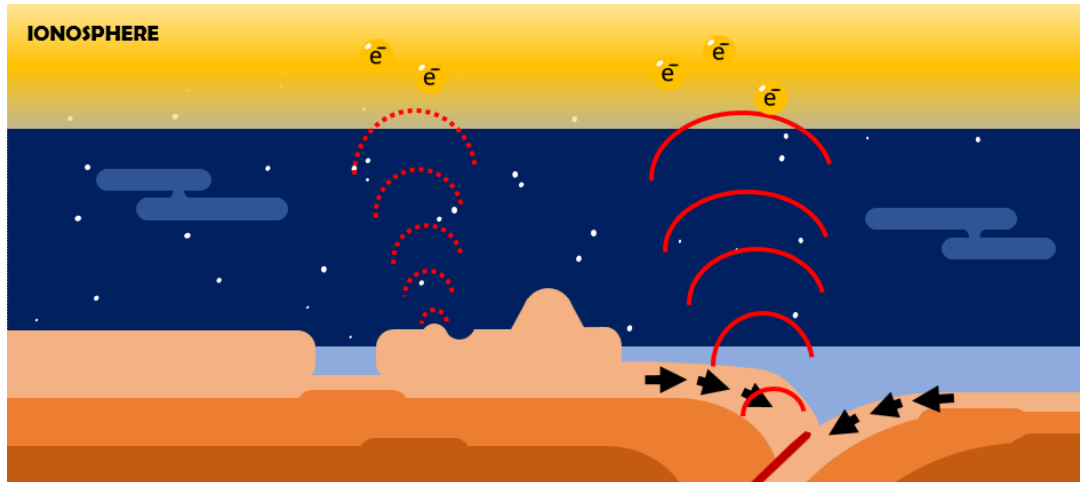
173 There are three types of plate boundaries. The first one is the divergent boundary, i.e., one  
174 plate goes away from another plate due to extensional force acting along the boundary. Divergent  
175 plate boundaries usually exist in the ocean floor as submarine mountain ranges, such as the Mid-  
176 Atlantic Ridge and the East Pacific Rise. The second boundary is the convergent boundary, where  
177 the plates collide with each other. Compressional forces between the two plates cause large  
178 earthquakes along such convergent boundaries. Such boundaries include the Japan Trench off the  
179 Pacific coast of NE Japan, and the Sumatra subduction zone running to the west of the Sumatra  
180 Island. Plate convergence often causes mountain building, and an island arcs is formed at one side  
181 of the convergent boundary. The last type is the translational plate boundary, where one plate  
182 moves sideways along the plate boundary (transform faults). The San Andreas fault zone in the  
183 western United States (US) is the typical plate boundary of this type.

184 Recently, solid earth was found to disturb the ionosphere in several different ways. For  
185 example, vertical movement of the surface during an earthquake faulting excites acoustic waves  
186 in the atmosphere. This wave propagates upward and reach the F-layer of the ionosphere and

187 makes a N-shaped pulse in TEC (Heki, 2021). This typically occurs ~10 minutes after the  
188 earthquake and can be as early as ~8 minutes after earthquake (Astafyeva et al., 2011). This kind  
189 of ionospheric anomaly is often called coseismic ionospheric disturbance (CID) and propagates  
190 horizontally at the F region sound speed 0.8-1.0 km/s.

191         Since the first detection of CID with GNSS by Calais and Minster (1995), there have been  
192 numbers of studies discussing the characteristics and underlying physics of CID. For example,  
193 Heki and Ping (2005) showed that the directivity of CID is controlled by the geomagnetic field by  
194 studying CID due to the 2003 Tokachi-oki earthquake, Hokkaido, for the first time using a dense  
195 network of GNSS. Such a directivity arises because of the Lorentz force acting on the movement  
196 of free electrons associated with the propagation of acoustic wave within neutral atmosphere in F-  
197 region. In the mid-latitude region in the northern hemisphere, such particle motions become  
198 perpendicular with the magnetic field at the northern side of the epicenter resulting in suppression  
199 of electron oscillations to the north of the epicenter.

200         Astafyeva and Heki (2009) studied the diversity of the CID waveforms for earthquakes  
201 with different focal mechanisms by studying the three large earthquakes 1994, 2006, and 2007  
202 with different focal mechanisms in the Kuril Islands. They demonstrated that a normal fault  
203 earthquake could give rise to CID starting with a negative change of TEC, in contrast to CID by  
204 reverse fault earthquakes starting with positive changes. For these earthquakes, Astafyeva et al.  
205 (2009) also identified the co-existence of two different kinds of acoustic waves, i.e., CID due to  
206 direct acoustic waves from the epicenter, and those excited by vertical crustal movements  
207 associated with the passage of the Rayleigh surface wave. The latter can be distinguished from the  
208 former by the propagation speed (~4 km/s) much faster than the former.



209

210 **Figure 2.** The acoustic wave (red circular wave) excited by coseismic vertical crustal movement  
 211 may propagate upward and disturb the ionosphere as CID. Surface Rayleigh wave triggers  
 212 secondary acoustic wave (dashed red circular wave).

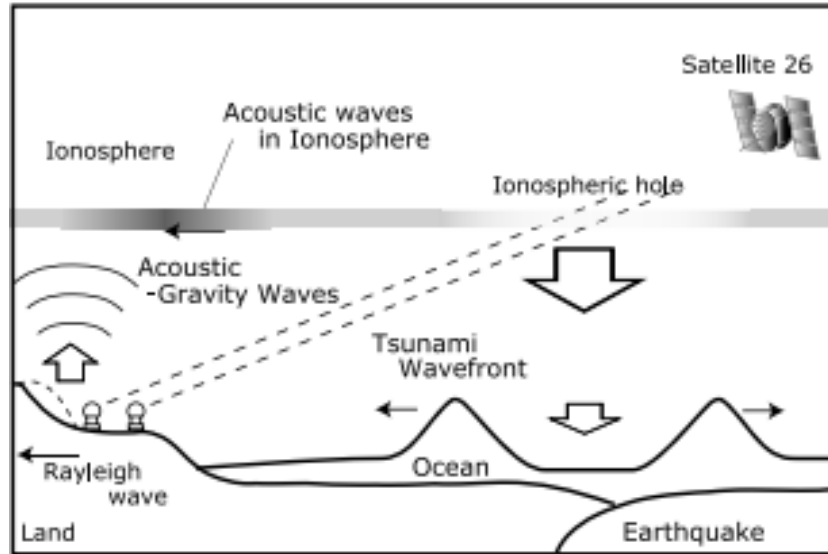
213

214 The CID by the Rayleigh surface waves has smaller geometric decay allowing the wave to  
 215 reach farther distance propagation. Heki (2021) shows clear signatures of the Rayleigh wave  
 216 generated by the 2004  $M_w$  9.2 Sumatra-Andaman earthquake in GEONET data in Japan ~40  
 217 minutes after the main shock. This kind of ionospheric disturbances help us infer surface wave  
 218 velocities in a region with limited number of seismometers.

### 219 **1.5 Ionospheric Disturbance due to the Sea Surface Motion**

220 Initial ocean motion generated by subduction zone earthquake causes acoustic disturbance  
 221 in ionosphere. There, the electron motion constrained by geomagnetic field makes long-lasting  
 222 electron depletion (formation of an ionospheric hole) above the tsunami source area (Kakinami et  
 223 al., 2012; Shinagawa et al., 2013; Zettergren and Snively, 2019). Such an ionospheric hole shows  
 224 TEC decrease right above the region of maximum uplift (due to the meter-scale downwelling of

225 the sea surface, Figure 3). The anomaly in the ionosphere starts right after the arrival of the acoustic  
226 wave and stays above the rupture area with little migration.



227

228 **Figure 3.** The coupling between ionosphere and sea surface and formation of the ionospheric hole  
229 after a large earthquake (Kakinami et al., 2012)

230

231 Rolland et al. (2010) found that the tsunami of the 2006  $M_w$  8.3 Kuril earthquake excited  
232 internal gravity waves and subsequent ionospheric disturbances with amplitudes 0.15-0.50 TECU.  
233 The tsunami waves generated by the 2004  $M_w$  9.2 Sumatran-Andaman earthquake also caused  
234 similar disturbances in the upper atmosphere above the Hawaiian Islands (Liu et al., 2006). There,  
235 the maximum peak-to-trough change was  $\sim 0.16$  TECU. Such waves were also detected by  
236 altimeters on board the Jason-1 and Topex/Poseidon satellites and yielded TEC changes of 0.2-0.6  
237 TECU in 30 seconds (Occhipinti et al., 2006).

## 238 **1.6 Earthquake Precursors in Ionosphere**

239 Ionospheric precursors of large earthquake are divided into long-term and short-term  
240 anomalies. The long-term precursors are detectable more than 1 day prior to the earthquake. Liu  
241 et al. (2001) found anomalous diurnal variation of ionospheric TEC from GNSS observations  
242 above the epicentral region of the 1999 Chi-chi earthquake ( $M_w7.7$ ), Taiwan. They showed that  
243 the diurnal variation amplitude decreased three to four days before the earthquake. Based on the  
244 analyses of many past earthquakes, Le et al. (2011) and Thomas et al. (2017) gave positive and  
245 negative conclusions, respectively, on the statistical significance of such precursory changes. On  
246 the other hand, the short-term anomaly first found by Heki (2011) occurs immediately before the  
247 main shock. This is the phenomenon I discuss in this thesis. For both long- and short-term  
248 anomalies, underlying physical mechanisms have remained ambiguous and controversial.

249 Searches for ionospheric anomalies related to large earthquakes involved satellites orbiting  
250 the earth. Using the data from the DEMETER (Detection of Electro-Magnetic Emissions  
251 Transmitted from Earthquake Regions) satellite launched by France, Němec et al. (2008) and Li  
252 and Parrot (2013) reported statistically significant anomalies in lower ionospheric electron density  
253 shortly before earthquakes. Newly launched China Seismo-Electromagnetic Satellite (CSES) has  
254 been used to investigate the TEC precursors. Song et al. (2020) found anomalies several days  
255 before the 2018  $M_w$  6.4 Lombok Earthquake. Adopting the moving median method (MMM) to the  
256 electron density data, they found precursory electron density enhancements occurred 2-5 days  
257 before this earthquake.

258 **1.7 3D Tomography for Ionospheric Electron Density Anomalies**

259 Computerized Tomography (CT) for ionospheric imaging has been developed over the last  
260 three decades. It was started by Austen et al. (1988), who tried to demonstrate the feasibility of  
261 CT to image ionospheric electron density distributions. He reconstructed two-dimensional (2D)  
262 image of electron density using TEC data obtained along the path from the naval navigation  
263 satellite systems (NNSS) toward several ground-based receivers. The results demonstrated that CT  
264 can be applied to study the ionosphere.

265 In the last decade, tomographic approaches to the ionosphere has advanced owing to the  
266 improved computation techniques and new data sets they used. For example, Tang et al. (2015)  
267 presented clear images of the ionosphere in 3D during an ionospheric storm under high  
268 geomagnetic activity. They utilized multiple observation techniques including radio-occultation,  
269 satellite-borne altimetry, conventional ionosonde, and the GPS-TEC technique.

270 After that, another ionospheric 3D tomography study was reported by Chen et al. (2016).  
271 There, they used only the GPS-TEC data to study the 3D spatial structure of MSTID. Taking  
272 advantage of the dense network of the receivers, they could successfully reconstruct electron  
273 density irregularities with 3D tomography. As another example, Garcia et al. (2005) imaged  
274 coseismic ionospheric perturbation by the Denali earthquake using GPS-TEC data. Although the  
275 anomaly was very large in space and GPS stations were not so dense, they could reveal the 3D  
276 structure to a certain extent.

277 Investigation of the electron density distribution in ionosphere is crucial in understanding  
278 physical mechanisms of ionospheric disturbances. The computerized ionospheric tomography is

279 an effective and promising approach to study 3D structures of ionospheric electron density,  
280 particularly in the region where dense GNSS networks are available like the Japanese Islands  
281 (Seemala et al., 2014; Chen et al., 2016; Saito et al., 2016).

## 282 **1.8 Research Objectives**

283 This thesis aims to map the ionospheric electron density anomalies related to large  
284 earthquakes by using the 3D tomography method and TEC data sets from ground GNSS networks.  
285 There are four specific ionospheric anomalies to be investigated here:

- 286 1. The ionospheric anomalies prior to the 2011  $M_w$  9.0 Tohoku-oki earthquake
- 287 2. The ionospheric anomalies prior to the 2010  $M_w$  8.8 Maule earthquake
- 288 3. The ionospheric anomalies after the 2011 Tohoku-oki earthquake
- 289 4. The ionospheric anomalies after the 2010 Maule earthquake

290 Then, I will discuss the differences in the preseismic ionospheric anomalies of the 3  
291 different earthquakes, i.e. the 2011  $M_w$  9.0 Tohoku-oki and the 2010  $M_w$  8.8 Maule earthquakes  
292 studied here, and the 2015  $M_w$  8.3 Illapel earthquake reported in He and Heki (2018). I finally  
293 discuss physical mechanisms for the short-term precursory changes in ionosphere, based on the  
294 3D tomography results obtained in this study.

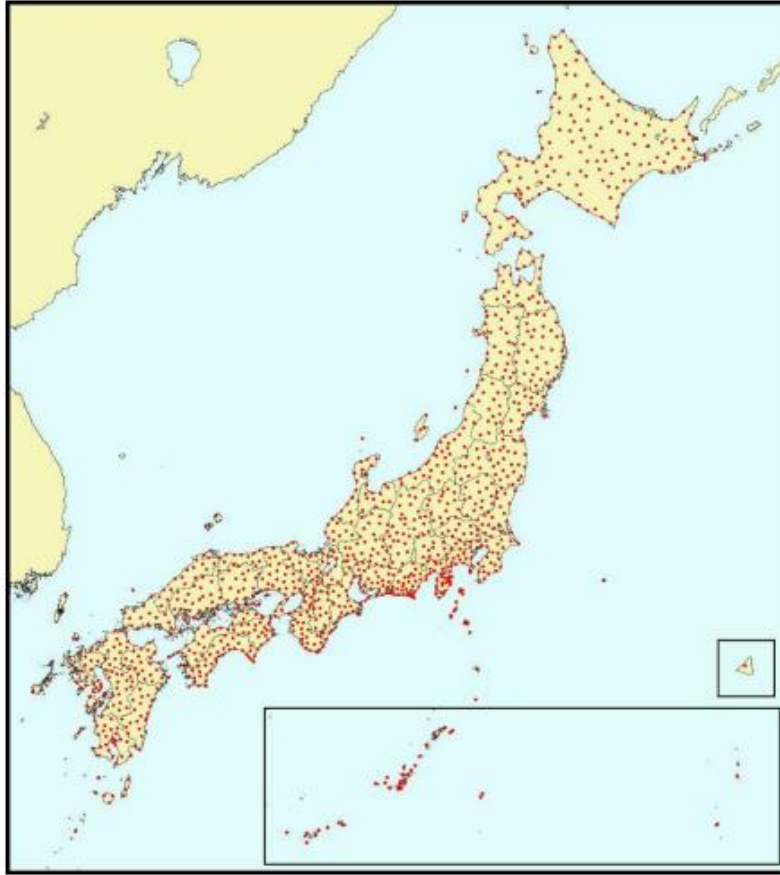
295

296

## 297 **Chapter 2: Data and Method**

### 298 **2.1 GNSS Network in Japan**

299 Geospatial Information Authority of Japan (GSI) operates the nationwide dense GNSS-  
300 network that covers the Japanese archipelago with ~1,300 stations with an average interval of ~20  
301 km. This network is used to study crustal deformation and to serve as “electronic reference points”  
302 in local geodetic surveys in Japan. This nationwide GNSS array is called GEONET (GNSS Earth  
303 Observation Network). The raw observation data and daily coordinates of the GEONET station  
304 are open to public on-line ([terras.gsi.go.jp](http://terras.gsi.go.jp)) in Japan. The raw data files in the receiver-independent  
305 exchange (RINEX) format provide data with the 30 second sampling interval. In this study, I  
306 downloaded the RINEX files from all the GEONET stations available for the studied dates.

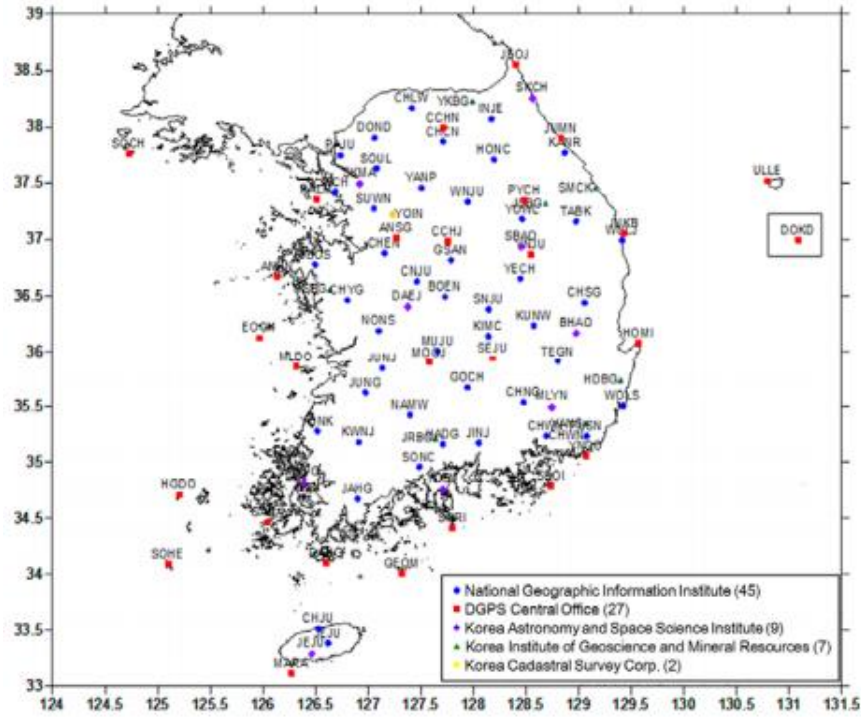


307

308 **Figure 4.** ~1,300 GEONET stations (red dots) are available in Japan (Tsuji and Hatanaka, 2018)

### 309 **2.2 GNSS Network in South Korea**

310 National Geographic Information Institute (NGII) of South Korea operates Korean GNSS  
311 Network (KGN) that covers the South Korea with over 45 stations with separations of 20-50 km.  
312 This network has been operated since March 1995 to investigate crustal deformation in the Korean  
313 Peninsula and its vicinity and serves as the national datum for precise positioning system (Kwon,  
314 2012). The raw GNSS data in the RINEX format files are recorded with the time interval of 30  
315 seconds (Choi and Hong, 2019).



316

317

**Figure 5.** The dense GNSS network in South Korea (Kwon, 2012)

318

319

320

321

322

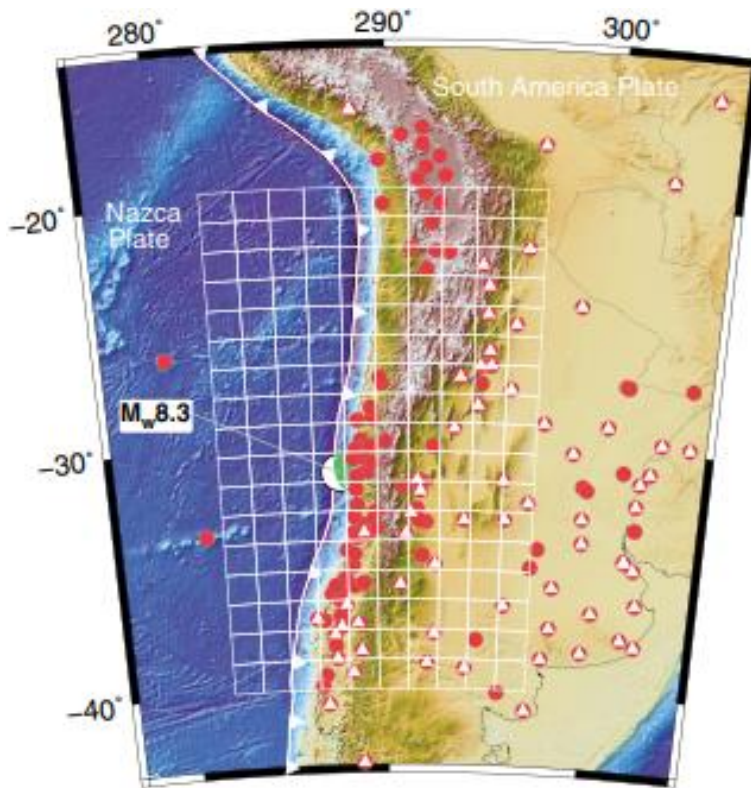
In this study, 53 stations of the Korean GNSS network are used for studying the ionospheric anomalies before and after the 2011  $M_w$  9.0 Tohoku-oki earthquake. Although the target of this study is ionosphere above the Tohoku region (far away from Korea), the availability of far-field station for this study is important to reinforce the spatial resolution of the 3D tomography of the ionosphere, especially in the western part of studied area.

323

324

325 **2.3 GNSS Networks in South America**

326 The RINEX data used in this study for South America are obtained from several different  
327 organizations including the Centro Sismológico Nacional of Universidad de Chile, the Red  
328 Argentina de Monitoreo Satelital Continuo (RAMSC) network of Instituto Geográfico Nacional  
329 de Argentina (IGNA), the Rede Brasileira de Monitoramento Contínuo dos Sistemas GNSS  
330 (RBMC) network of Instituto Brasileiro de Geografia e Estatística (IBGE), International GNSS  
331 Service ([www.igs.org](http://www.igs.org)), and University NAVSTAR Consortium ([www.unavco.org](http://www.unavco.org)).



332

333 **Figure 6.** 146 GNSS stations in South America used by He and Heki (2018) for 3D ionospheric  
334 tomography of ionospheric anomalies before the 2015 Illapel earthquake.

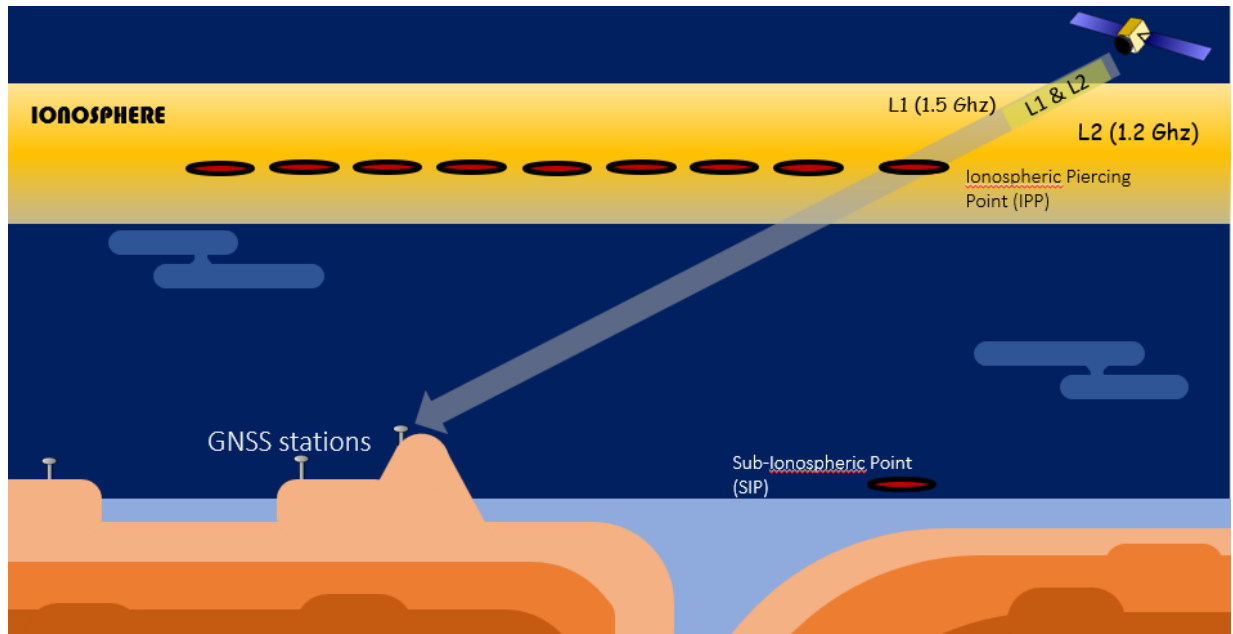
335           There are 146 GNSS stations in South America and 65 of them can track GLONASS as  
336 well as GPS. These data are used to analyze the TEC changes before the 2015  $M_w$  8.3 Illapel, and  
337 89 of those GNSS stations were used to study the 2010  $M_w$  8.8 Maule earthquakes.

#### 338 **2.4 GNSS-TEC Method**

339           The slant TEC (STEC) is observed for a pair of GNSS satellite and receiver and  
340 corresponds to the total number of electrons integrated along the line-of-sight (LoS). The STEC is  
341 derived from the change in the phase differences  $\Delta L_4$  between the L1 and L2 microwave carrier  
342 phases (expressed in length). In this study, equation (2) is used to convert L4 changes into STEC  
343 changes:

$$344 \quad \Delta STEC = \left( \frac{1}{40.308} \right) f_1^2 f_2^2 / (f_1^2 - f_2^2) \Delta L_4 \quad (2)$$

345           There,  $f_1$  (1575.42 MHz),  $f_2$  (1227.6 MHz) are the frequencies of the two carrier waves (L1  
346 and L2) in the L-band from GPS satellites, respectively (such frequencies are slightly different for  
347 other GNSS). The phase difference of the two frequencies ( $\Delta L_4$ ) are often called the ionospheric  
348 linear combination or geometry-free linear combination. The coefficient 40.308 is to convert  
349 ionospheric delays into TEC in TEC unit (TECU,  $10^{16}$  electrons/m<sup>2</sup>).



350

351 **Figure 7.** Illustration of L1 and L2 microwave signals propagating from GNSS satellites to GNSS  
 352 receivers. IPP is the intersection of LoS with the hypothetical thin layer in ionosphere, and its  
 353 ground projection is called SIP.

354

355           When GNSS satellites transmit microwave signals in both L1 and L2 frequencies, LoS will  
 356 have an intersection point with the ionosphere. This intersection is called as ionospheric pierce  
 357 point (IPP) and its projection onto the earth surface is named as sub-ionospheric point (SIP).  
 358 Although the actual ionosphere is distributed over a wide range of altitudes, we assume a thin  
 359 hypothetical layer at the height of largest electron density (~300 km) to calculate IPP and SIP  
 360 coordinates, usually expressed with the geocentric cartesian coordinates fixed to the solid earth.  
 361 There are 32 GPS satellites at this moment, and the number of satellites have been increasing  
 362 drastically by the development of GNSS other than GPS. The increase of numbers of ground  
 363 stations and GNSS satellites is important in the performance of the 3D tomography technique used  
 364 in this study.

365 We need to remove the satellite and receiver inter-frequency biases (IFB) caused by  
366 different electric path lengths of L1 and L2 circuits within satellites and receivers. For the  
367 GEONET stations, such biases can be downloaded from Electric Navigation Research Institute  
368 (ENRI) website ([www.enri.go.jp](http://www.enri.go.jp)) (Sakai, 2005). After correcting for these biases, we can convert  
369 STEC to vertical TEC (VTEC) by multiplying them with the cosine of the incidence angle of LoS  
370 to ionosphere. For the stations in South Korea and South America, the receiver biases are  
371 determined by minimum scalloping method by Rideout and Coster (2006). In this method, a  
372 receiver IFB of a certain station is obtained by minimizing the scatter of VTEC during a period  
373 from midnight to dawn obtained with various satellites observed at that GNSS station. Satellite  
374 IFBs are obtained from the header information of the Global Ionosphere Maps (GIM) downloaded  
375 from University of Berne ([aiub.unibe.ch/CODE](http://aiub.unibe.ch/CODE)).

376 I first isolated the absolute STEC by removing IFBs. Then, such STEC is converted to  
377 VTEC by multiplying it with the cosine of the incident angles of LoS with a thin layer at 300 km  
378 altitude. I use equation (3) to calculate VTEC:

$$379 \quad \text{VTEC} = (\text{STEC} - d)\cos\theta, \quad (3)$$

380 where  $\theta$  and  $d$  represent the incidence angle of LoS at IPP altitude, and IFB (sum of satellite IFB  
381 and receiver IFB) for this satellite-receiver pair, respectively. Such VTEC data do not contain  
382 apparent U-shaped changes caused by elevation angle variations and are much easier to interpret  
383 than STEC.

## 384 **2.5 Strategies to Isolate Anomalies from GNSS-TEC Data**

385 In this study, I use TEC changes obtained from the time series of VTEC. Anomalous  
386 behavior of VTEC needs to be extracted from the observed data. Here I adopt the following two  
387 types of strategies to isolate the ionospheric anomalies:

388 1. Modelling the temporal change of VTEC with a polynomial of time which is estimated  
389 using the least-squares method. For example, if the polynomial degree is two, the model is  
390 expressed by equation (4):

$$391 \text{VTEC}(t) = at^2 + bt + c, \quad (4)$$

392 where  $a$ ,  $b$ , and  $c$  are parameters to be estimated using the least squares method. The  
393 estimated models will serve as reference curves, and differences from these curves are  
394 defined as the anomalies. There are two key factors we need to care when we obtain the  
395 most appropriate models. First one is the choice of the polynomial degree. I use the L-curve  
396 method to choose the best degree, i.e., I compare the root-mean-squares of the residuals  
397 and employ the degree with which the residual showed a large drop (and insignificant drop  
398 for higher degrees). Second factor is the start and the end of the exclusion time window to  
399 avoid the leakage of the earthquake-related anomalies into the reference curves. Proper  
400 selection of the windows is important to avoid artificial anomalies. I will discuss these two  
401 factors in more detail in the next chapter.

402 2. Making the difference between medians of VTEC from two periods (before and after the  
403 start of the anomalies). I use this method when it is difficult to estimate reference curves in  
404 an objective manner. Further explanation to this topic will be discussed later.

405 In this study, I use the first strategy when I analyze preseismic ionospheric changes for the  
406 2011  $M_w$  9.0 Tohoku-oki, 2015  $M_w$  8.3 Illapel, and the 2010  $M_w$  8.8 Maule earthquakes. On  
407 the other hand, the second strategy is used to isolate the postseismic electron depletion of the  
408 2011  $M_w$  9.0 Tohoku-oki earthquake. Each strategy is used to obtain ionospheric anomalies as  
409 VTEC residuals. In this study, such VTEC residuals are converted back to STEC residuals and  
410 are used as the input to the 3D tomography calculations.

## 411 **2.6 Ionospheric 3D Tomography Method**

412 The first step to perform 3D tomography is to set up voxels covering the studied region  
413 and the target altitude range. The electron density anomaly within a block is assumed  
414 homogeneous, and such anomalies are estimated for all the voxels. I employ different setting of  
415 voxels for different earthquake cases considering the anticipated region of the anomaly signals and  
416 the GNSS station distribution. Smaller voxels would result in a better spatial resolution of the  
417 results. However, dense distribution of LoS penetrating the blocks is needed to make the  
418 tomography results meaningful.

419 Thus, the second step is to collect as many LoS passing through the blocks as possible. If  
420 the ground GNSS stations track multi-GNSS, i.e., not only GPS but also GLONASS, Galileo and  
421 QZSS, such data should also be used as the input to the tomography. In fact, Muafiry et al. (2018)  
422 used both GPS and GLONASS data to perform 3D tomography of sporadic E irregularities.

423 TEC anomaly of an LoS ( $y_i$ ) from a certain satellite to a certain receiver is composed of  
424 the sum of the products of the electron density anomalies ( $L_j$  for the  $j$ -th block) and the penetration  
425 lengths ( $A_{ij}$ ) for blocks located along the LoS as expressed by equation (5).

426 
$$y_i = \sum_j A_{ij} L_j + e_i \quad (5)$$

427 There,  $e_i$  represents the measurement error of the  $i$ -th pair, and I assumed it as 0.05 TECU  
 428 for all the measurements. This corresponds to a typical error for differential GNSS VTEC  
 429 measurements (Coster et al., 2013). Equation (5) serves as the observation equation and the matrix  
 430  $A_{ij}$  becomes the Jacobian matrix.

431 First, I need to calculate the penetration lengths of LoS with voxels ( $A_{ij}$ ) using simple  
 432 geometric calculations. Generally speaking, one LoS has two (penetrated) or zero (not penetrated)  
 433 intersection points with the surface of one voxel, and  $L_j$  is the distance between the entry point to  
 434 the exit point for penetrated voxels. I use the GNSS station positions available in the header  
 435 information of the RINEX files. The instantaneous satellite coordinates are calculated using the  
 436 broadcast orbit information of the GNSS satellites. Then, the coordinates of the intersection points  
 437 of LoS with the block surfaces can be calculated. Let  $x, y, z$  be the coordinate of points along a  
 438 certain LoS, they can be expressed as follows:

439 
$$x = x_a + \varepsilon (x_s - x_a) \quad (6)$$

440 
$$y = y_a + \varepsilon (y_s - y_a) \quad (7)$$

441 
$$z = z_a + \varepsilon (z_s - z_a) \quad (8)$$

442 where  $x_a, y_a, z_a$  represent the receiver coordinate  $x_s, y_s, z_s$  represent the satellite coordinate. The  
 443 parameter,  $\varepsilon$ , changes over a range from zero to one ( $0 < \varepsilon < 1$ ), i.e.,  $(x, y, z)$  signify the receiver  
 444 and satellite coordinates when  $\varepsilon$  is 0 and 1, respectively. Coordinates of points on the up-down,

445 east-west, and north-south surfaces of the block should satisfy the following three equations,  
 446 respectively.

$$447 \quad x^2 + y^2 + z^2 = (R + H)^2 \quad (9)$$

$$448 \quad \frac{y}{x} = \mathbf{\tan} \varphi \quad (10)$$

$$449 \quad \frac{z^2}{(x^2+y^2)} = \mathbf{\tan}^2 \theta \quad (11)$$

450 There,  $R$  is the radius of the Earth at this latitude,  $H$ ,  $\varphi$ ,  $\theta$  are the height, longitude and  
 451 latitude of the horizontal, vertical (north-south), vertical (east-west) surfaces of a block. Here I  
 452 assumed that the earth is a sphere without flattening. The coordinates of the LoS penetration points  
 453 with these surfaces could be obtained by substituting  $x$ ,  $y$ ,  $z$  in (9)-(11) with those in (6)-(8), and  
 454 solving for the parameter  $\varepsilon$ .

455 Now, the elements of the Jacobian matrix ( $A_{ij}$ ) in equation (5) has been obtained, and I  
 456 will proceed to estimate the set of parameters  $L_j$  to obtain the electron density anomalies within  
 457 individual voxels. The observation equation (5) can be written in a matrix form as:

$$458 \quad \mathbf{y} = \mathbf{Ax} + \mathbf{e} \quad (12)$$

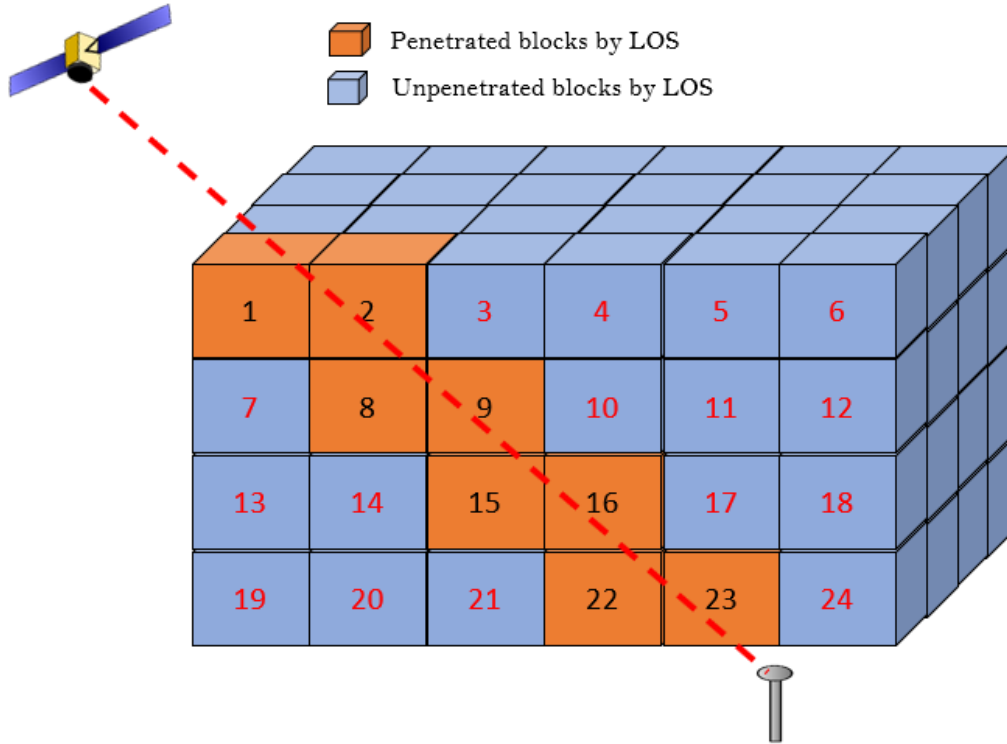
459 where  $\mathbf{y}$  is the vector composed of STEC anomalies  $y_i$ ,  $\mathbf{A}$  is the Jacobian matrix composed of  $A_{ij}$ ,  
 460  $\mathbf{x}$  is the vector composed of unknown parameters  $x_j$  (electron density anomalies of individual  
 461 blocks), and  $\mathbf{e}$  is the measurement errors. The vector  $\mathbf{x}$  is derived by solving the normal equation:

$$462 \quad \mathbf{x} = (\mathbf{A}^T \mathbf{A})^{-1} \mathbf{A}^T \mathbf{y} \quad (13)$$

463 after the Cholesky's decomposition, i.e., by decomposing the normal matrix  $A^T A$  into lower  
464 triangular matrix  $L$  and its transpose.

$$465 \quad \mathbf{A}^T \mathbf{A} = \mathbf{L} \mathbf{L}^T \quad (14)$$

466 Even if the LoS are densely distributed, they may not penetrate all the blocks, especially  
467 above the oceanic and above areas without sufficient stations. Hence, certain constraints need to  
468 be introduced to regularize the least-squares inversion. Here, a continuity constraint is used, i.e., it  
469 is assumed that neighboring blocks have the same electron density anomalies with a certain  
470 allowance for the difference. Suppose block number  $j$  is at the east side of block number  $i$ , then  
471 assuming  $x_i$  and  $x_j$ , the electron density anomalies of these blocks, satisfy  $x_i - x_j = 0$ . One block  
472 normally has six neighboring blocks (up, down, north, south, east, and south), and all these pairs  
473 are added to the normal matrix as virtual observations (Nakagawa and Oyanagi, 1982). The block  
474 pairs that are not juxtaposed is not constrained. I used the allowance for this constraint of  $0.10 \times$   
475  $10^{11}$  el/m<sup>3</sup> (this unit is equivalent to 1 TECU, or  $10^{16}$  electrons/m<sup>2</sup>, for penetration length of 100  
476 km).



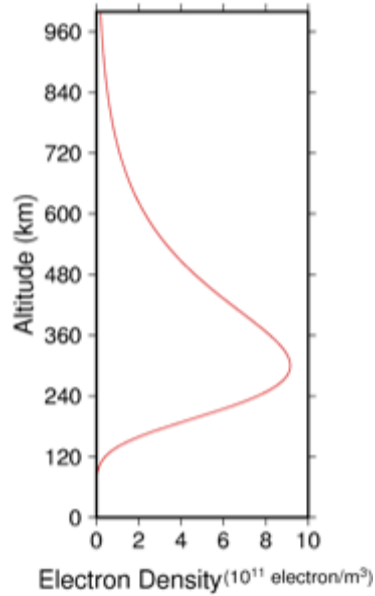
477

478 **Figure 8.** Illustration of blocks (voxels) in 3D tomography and penetration of LoS with a part of  
 479 the blocks.

480

481 As an additional constraint, I weakly constrained the electron density anomalies around  
 482 zero with an altitude-dependent allowance. According to the Chapman distribution, electron  
 483 density at height  $h$  is proportional to  $\exp(1 - A - e^{-A})/2$ , where  $A$  equals to  $(h-h_{\max})/H$ . There,  $h_{\max}$   
 484 is the electron density peak altitude (300 km) and  $H$  is assumed 80 km. The allowance for this  
 485 second constraint was assumed to be proportional to this distribution, and set as large as 1 % of  
 486 the electron density at that altitude. This implies that I constrain the electron density strongly  
 487 around zero for altitudes in the D and E regions, where electron density is lower, and weakly

488 around zero in the F region of the ionosphere, where electron density is higher. This is to avoid  
489 estimation of unrealistically large electron density anomalies in very high or very low altitudes.



490

491 **Figure 9.** The Chapman functions showing altitude dependence of ionospheric electron densities.

492

493 **Chapter 3: 3D Tomography of the Ionospheric Anomalies immediately before**

494 **Earthquakes: The 2011 Tohoku-oki Earthquake**

495

496 *The content of this chapter was published in Journal Geophysical Research Space Physics, Muafiry, I.N.and K. Heki, 3D*

497 *tomography of the ionospheric anomalies immediately before and after the 2011 Tohoku-oki ( $M_w$ 9.0) earthquake, J. Geophys. Res.*

498 *Space Phys., 125, e2020JA027993, doi:10.1029/2020JA027993, 2020*

499

### 500 **3.1 Introduction: History of Debate**

501 Differential ionospheric delays (phase advances) of the two microwave carriers from  
502 GNSS satellites enable us to study ionospheric TEC and its change in high temporal and spatial  
503 resolutions. TEC data represents the number of electrons integrated along the LoS connecting  
504 satellites and ground receivers. Vertical crustal movements associated with large earthquakes  
505 trigger direct acoustic waves propagating upward. They reach the F-region of the ionosphere 8-10  
506 minutes after earthquakes and disturb ionosphere causing changes in TEC.

507 Such a coseismic ionospheric disturbance (CID) has been first studied with GNSS by  
508 Calais and Minster (1995) and with a dense GNSS network by Heki and Ping (2005). Later,  
509 Astafyeva et al. (2011) studied immediate ionospheric response to the 2011 Tohoku-oki  
510 earthquake, and Rolland et al. (2013) clarified mechanisms of several important properties such as  
511 the CID directivity. Cahyadi and Heki (2015) proposed an empirical law connecting the earthquake  
512 magnitude and the CID amplitudes, and Astafyeva and Shults (2019) explored the way to study  
513 smaller earthquakes with CID. As reviewed in Heki (2021), the Japanese dense network GEONET  
514 (GNSS Earth Observation Network) produces TEC data with high spatial (~20 km) and temporal  
515 (30 s) resolution and contributed to our understanding of ionospheric disturbances related to  
516 earthquakes.

517 Shortly after the 2011 March 11 Tohoku-oki ( $M_w$ 9.0) earthquake, Heki (2011) reported the  
518 occurrence of positive (and partly negative) changes in TEC starting ~40 minutes before the  
519 earthquake near the epicenter using GEONET. Heki (2011) also reported the occurrences of  
520 similar anomalies before the 2004 Sumatra-Andaman ( $M_w$  9.2), 2010 Maule ( $M_w$  8.8), and the  
521 1994 Hokkaido Toho-oki ( $M_w$  8.3) earthquakes.

522           Then three papers published after that (Kamogawa and Kakinami, 2013; Utada and  
523 Shimizu, 2014; Masci et al., 2015) doubted the reality of the TEC changes before the 2011 Tohoku-  
524 oki earthquake. Coseismic acoustic disturbance makes not only short-term N-shaped TEC changes  
525 but also airglow (Inchin et al., 2020) and long-lasting electron depletion in the ionosphere  
526 (Kakinami et al., 2012; Shinagawa et al., 2013; Zettergren and Snively, 2019). In Heki (2011), the  
527 TEC anomalies were defined as the departure from the reference curves. The major criticism by  
528 these three papers is that the enhancement is an artefact that emerged by using the data after the  
529 earthquake (including the long-lasting TEC drop) in defining the reference curves.

530           Rebuttals to those three papers have been published in the same journal (Heki and  
531 Enomoto, 2013; 2014; 2015). For example, Heki and Enomoto (2015) showed the reality of the  
532 positive bending of TEC before earthquakes using the Akaike information criterion (AIC). They  
533 confirmed statistical significance of the bending immediately before large earthquakes (e.g. 40  
534 minutes before the 2011 Tohoku-oki earthquake), demonstrating that such bending could be  
535 detected even without using the data after earthquake occurrences. They further demonstrated that  
536 the leading times and the intensities of the bending depend on  $M_w$  from seven large earthquakes  
537 with reasonable amount of available GNSS data.

538           In a mean time, a new algorithm to detect such preseismic TEC changes was proposed by  
539 focusing the spatial correlation of preseismic TEC data (Iwata and Umeno, 2016). This work,  
540 together with Heki and Enomoto (2015), substantiate the existence of the preseismic anomalies.  
541 Subsequently, He and Heki (2017) lowered the threshold of earthquake magnitudes and compiled  
542 similar TEC enhancements prior to 18 earthquakes worldwide with  $M_w$  7.3-9.2 and confirmed

543 systematic  $M_w$  dependence of preseismic ionospheric anomalies, i.e. the anomalies for earthquakes  
544 of larger  $M_w$  start earlier and grow stronger (relative to background TEC).

545         The physical mechanism responsible for these preseismic signals is only partly understood.  
546 Evidences obtained so far suggest it electromagnetic, assuming e.g. positive surface charges  
547 responsible for the ionospheric electron redistribution. Mobile positive holes generated by the  
548 breakage of the peroxy bonds that are ubiquitous in rocks (Freund, 2011) offer a scenario consistent  
549 with the TEC observations. The holes are a quantum mechanical state and spread as fast as a few  
550 hundreds of meters per second from seismogenic depths to the surface (Freund, 2013). Regarding  
551 the ionospheric electron redistribution by surface charges, several mechanisms have been  
552 proposed, e.g., Kuo et al. (2014) and Kelley et al. (2017). This issue will be discussed in detail  
553 later.

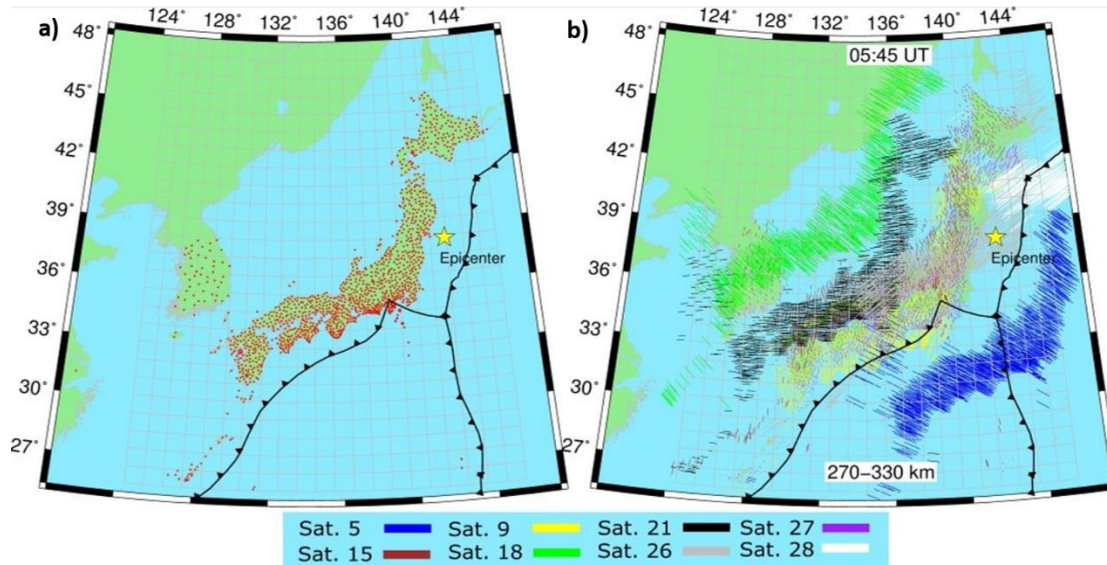
554         To understand the underlying physical process, it is effective to investigate the spatial  
555 structure and temporal evolution of the preseismic electron density anomalies. Recently, He and  
556 Heki (2018) studied the spatial structure of the electron density anomalies before the 2015 Illapel  
557 earthquake, Chile ( $M_w$  8.3), using 3D tomography technique. The result suggested that the  
558 preseismic changes were composed of two parts, ionosphere electron density increase and  
559 decrease. They emerged ~20 minutes before earthquake and are situated at lower and higher  
560 altitudes, respectively, along the geomagnetic field. The same 3D tomography technique has been  
561 applied for studies of 3D structures of electron density changes by the 2017 total eclipse in North  
562 America (He et al., 2018) and sporadic-E irregularities in Japan (Muafiry et al., 2018).

563           In this study, an improved version of the 3D tomography technique is applied to anomalies  
564 immediately before the 2011 Tohoku-oki earthquake. The explanation about our 3D tomography  
565 method is explained in detail in Chapter 2. Here, the anomaly signals are stronger than the 2015  
566 Illapel earthquake and would help us better understand the 3D structure and the evolution of the  
567 ionospheric electron density anomalies. The leading time of the preseismic anomaly of the 2011  
568 earthquake is longer (~40 minutes) than the 2015 earthquake (~20 minutes). This makes us select  
569 the objective procedure to isolate the TEC anomalies carefully, and this issue has been partly  
570 discussed in Chapter 2 and will be discussed again later on. At the end of Chapter 3, a simple  
571 mechanism to redistribute ionospheric electrons by surface charges is also proposed.

572

### 573 **3.2 Data set**

574           GNSS data from the entire GEONET is used, a dense array of continuous GNSS receiving  
575 stations in Japan. I also add data from the GNSS network in South Korea, with 53 stations and ~40  
576 km average separation (Choi and Hong, 2019), to reinforce the resolution in the western part of  
577 the studied area. In total, I used 1,284 GNSS stations to study the preseismic anomalies of the 2011  
578 Tohoku-oki earthquake (Figure 10a). I used 8 GPS satellites (PRN 05, 09, 15, 18, 21, 26, 27, 28)  
579 visible from the studied region immediately before the mainshock (05:45 UT). Unfortunately,  
580 GEONET did not track GNSS other than GPS in 2011. Other data set has been explained in detail  
581 in Chapter 2.



582

583 **Figure 10.** Maps showing the GNSS station distribution (red dots) and the voxels for 3D  
 584 tomography above Japan, the Sea of Japan, and the Eurasian Continent including the Korean  
 585 Peninsula (a). Yellow star indicates the epicenter of the 2011 Tohoku-oki ( $M_w$ 9.0) Earthquake.  
 586 Black curves illustrate boundaries between tectonic plates in and around the Japanese Islands. The  
 587 short lines indicate the LoS of satellite-station pairs at the altitude 270-330 km (one layer of voxels)  
 588 one minute before the earthquake (b). Color of the lines indicates satellite numbers.

### 589 3.3 Data Processing Strategy

590 As described in Chapter 2, the study of preseismic anomaly will be using reference curves  
 591 to isolate the VTEC anomalies. This method has been often criticized by two reasons, (1)  
 592 postseismic drops influence the reference curves and cause artificial enhancements, and (2) it is  
 593 inappropriate to use the TEC data after the earthquake for earthquake prediction studies. As for  
 594 (1), I avoid the influence of the postseismic drop by excluding the part of VTEC time series when  
 595 SIP (the ground projection of the intersection of LoS with a thin layer at 300 km altitude) is above  
 596 the focal area (see Figure 11 inset maps). Considering the mechanism of postseismic TEC drops  
 597 by downward plasma transport and recombination (Kakinami et al., 2012; Shinagawa et al., 2013)  
 598 and numerical simulation of its long-term behavior (Zettergren and Snively, 2019), it is unlikely

599 that the area of postseismic drop occurs in areas far from the focal area, and its influence can be  
600 mostly avoided by excluding VTEC data with SIP overlapping the focal region. This will be  
601 discussed again later in this section.

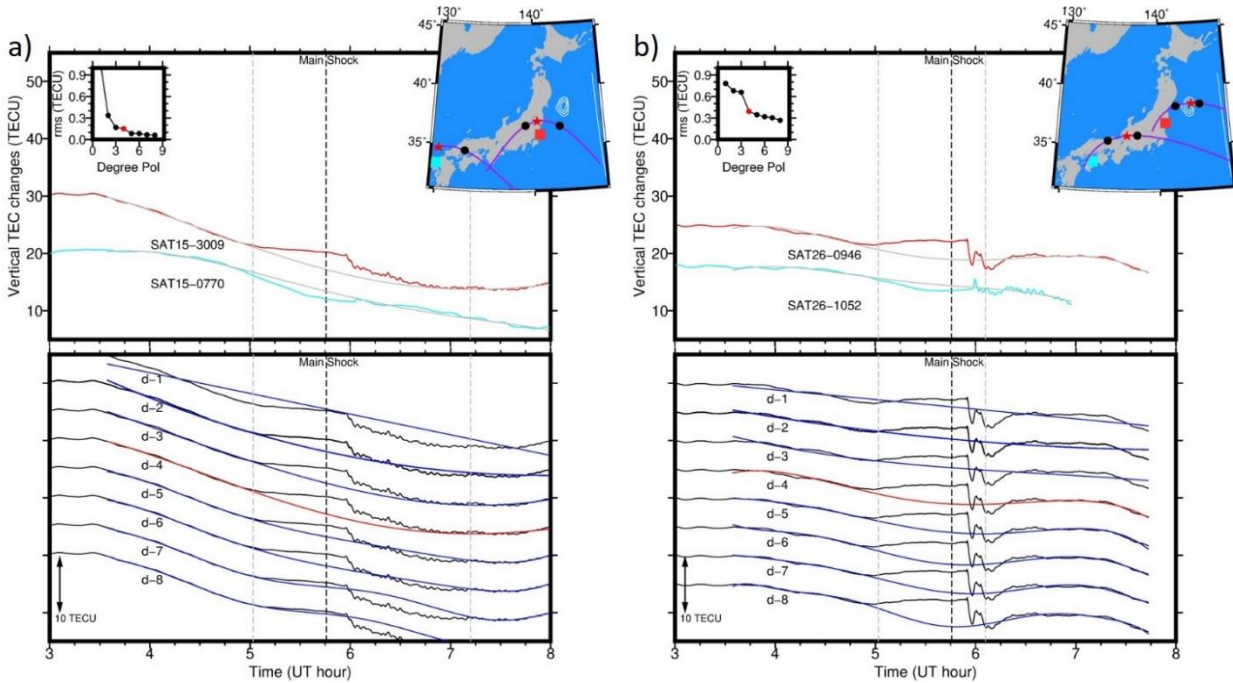
602         Regarding (2), a series of studies on this topic, from Heki (2011) to this thesis, do not aim  
603 at practical earthquake prediction by observing GNSS-TEC in a near future. It would be more  
604 important to answer the question if earthquakes know their final sizes when they start (i.e. the  
605 question whether earthquakes are predictable or not) at this moment. From this point of view, the  
606 reference curve method is appropriate to study preseismic signals because earthquakes would not  
607 leave permanent changes (like coseismic steps in station coordinates) in TEC.

608         There are numbers of difference in the method to obtain the TEC anomalies from the early  
609 study (Heki, 2011). Here I explain the three main differences, (1) input data, (2) selection of  
610 exclusion windows, and (3) determination of polynomial degrees. For point (1), biased STEC is  
611 converted to absolute VTEC beforehand and the reference curves are estimated to model the  
612 absolute VTEC time series as explained in Chapter 2. This is different from Heki (2011), where  
613 both polynomial coefficients and the bias are estimated simultaneously using STEC time series as  
614 the input data. The new method enables us to model the time series using higher order polynomials  
615 and to optimize the polynomial degrees using the L-curve method.

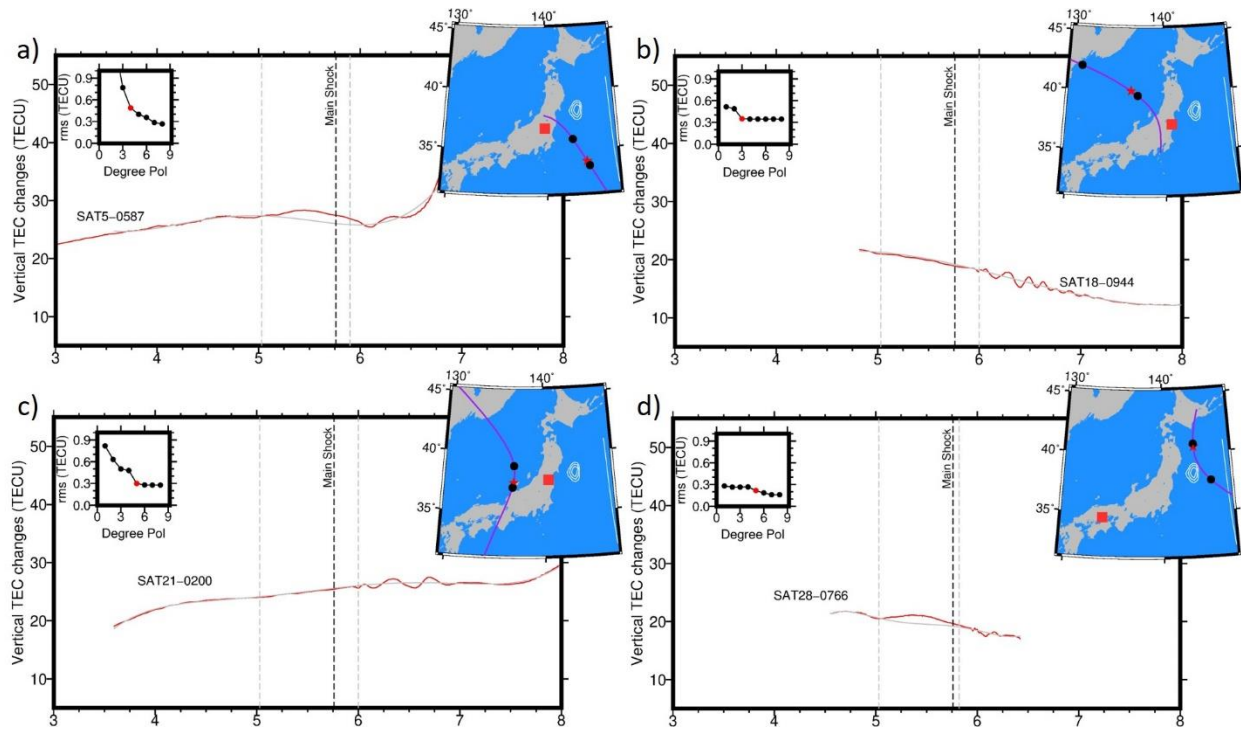
616         Another difference is that here I include the satellites that do not show significant  
617 anomalies. For example, GPS Sat.18 was not studied in Heki (2011) because they showed little  
618 TEC anomalies. However, such data are important to show where preseismic anomalies do “not”  
619 emerge. After all, I used 8 GPS satellites including four new satellites 5, 18, 21, and 28 in addition

620 to 9, 15, 26, and 27 studied in Heki (2011). In Figure 12a-d, I show time series, similar to Figure  
621 11, of four examples with these new satellites. There I fit the data with polynomials with degrees  
622 determined by the L-curves in the insets. The geometry of the station position, satellite SIP track  
623 (calculated assuming 300 km as the height of the thin ionosphere), and the epicenter are given in  
624 inset maps. Satellites 18 (c) and 21 (d) do not show significant preseismic anomalies (only  
625 coseismic acoustic disturbances) although the excluding windows are used in the polynomial  
626 fitting. The data from Satellites 5 (a) and 28 (d) include weak preseismic anomalies together with  
627 coseismic acoustic disturbances. These LoS do not penetrate the postseismic negative anomaly  
628 and do not show postseismic TEC drops.

629



630  
 631 **Figure 11.** Fitting reference curves of VTEC changes for satellite-receiver pairs of GPS Sat.15-  
 632 3009 (a) and Sat.26-0946 (b) showing positive preseismic anomalies (upper panel, red curves). I  
 633 also show two different pairs showing negative anomalies for comparison (upper panel, cyan  
 634 curves). Vertical dashed lines indicate the exclusion window in fitting the model with polynomials.  
 635 Red stars and black circles attached to the SIP tracks in the inset maps show the SIP positions at  
 636 the main shock and at the start and end of the exclusion window (I assumed 300 km to calculate  
 637 the SIP positions). Red and cyan rectangles indicate the locations of the two receivers. The maps  
 638 also include the coseismic slip distribution drawn with the contours of 3-meters step (Ozawa et al.,  
 639 2011). The L-curves in the left insets show the root-mean-square (rms) of the VTEC residuals  
 640 obtained by fitting curves of various polynomial degrees. I employed the red curves in the lower  
 641 panels, i.e. degree 4 for (a) and (b), that showed significant rms drops in the L-curves.



642

643 **Figure 12.** VTEC time series (red curves) and models with polynomials (grey curves) for satellite-  
 644 receiver pairs with four newly used GPS satellites, i.e. Sat.5-0587 (a), Sat.18-0944 (b), Sat.21-  
 645 0200 (c), and Sat.28-0766 (d). See the caption of Figure 11 for other symbols.

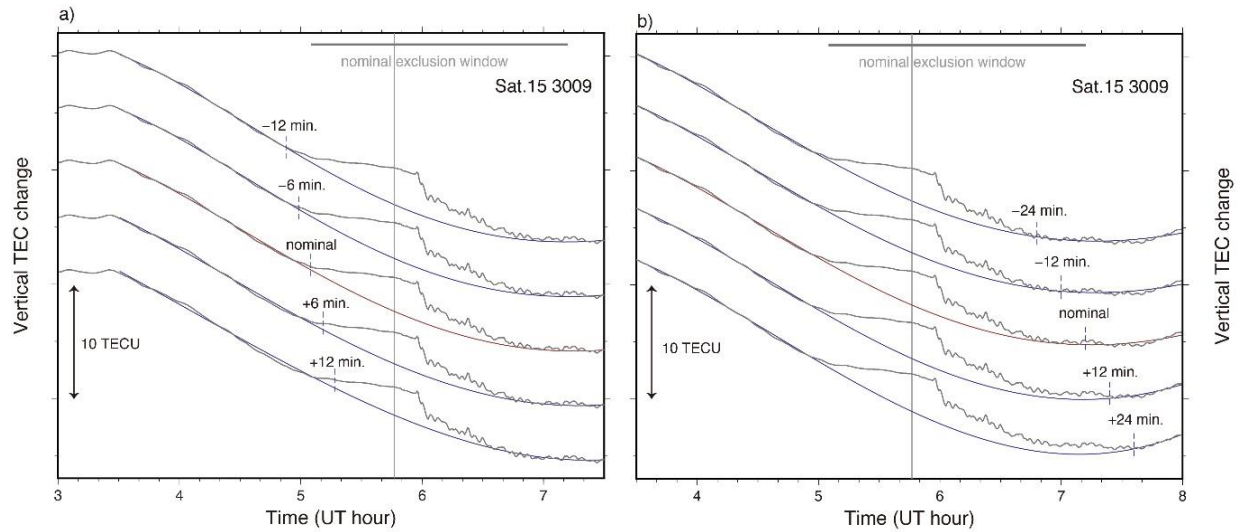
646

647           Regarding point (2), Heki (2011) excluded a time window 5.2-6.0 UT possibly influenced  
 648 by the pre-, co-, and postseismic ionospheric disturbances in fitting the reference curves for all the  
 649 four satellites. Here, I fit the polynomial to absolute VTEC using the excluding windows with the  
 650 start and end times determined from external information. The selection of the end of this exclusion  
 651 window is especially important because reference curves estimated using the period influenced by  
 652 the long-lasting postseismic TEC drop may give rise to artificial preseismic TEC increase. In  
 653 Figure 13, I demonstrate that the VTEC anomalies during the preseismic period 5:05-5:46 UT is  
 654 not so sensitive to the excluding window settings using the case of Figure 2a.

655 For the start of the exclusion window, I employed the onset of the preseismic anomaly 5:05  
656 UT for all the satellites (~40 minutes prior to the main shock). This time was obtained by Heki and  
657 Enomoto (2015) by searching significant positive bending in VTEC time series using AIC. As  
658 shown in Figure 13a, changing this starting time by  $\pm 12$  minutes does not make significant  
659 differences in the reference curves for this pair of the satellite and the station.

660 Regarding the end time of the exclusion window, it is assumed that the postseismic drop  
661 (ionospheric hole) occurs by coseismic vertical crustal movement and hence over the ruptured  
662 fault. This will be confirmed later in Chapter 5 and supported by a numerical simulation, e.g.  
663 Figure 4a of Zettergren and Snively (2019). I determined the end time of the exclusion window by  
664 drawing the SIP trajectories to know the time for SIP to go out of the affected area (defined as the  
665 area above the fault with slips exceeding 3 m). Naturally, the end times depend on satellites (see  
666 Figure 11 inset maps). Table 1 lists the exclusion time windows for individual satellites used in  
667 this study (windows depend on regions of the stations, too, for some satellites).

668



669

670 **Figure 13.** The numerical experiments to move the starting (a) and ending (b) times of the  
 671 exclusion window in estimating the reference curves for the same data as in Figure 11a (station  
 672 3009, satellite 15). In (a), the starting time is set to 4:53, 4:59, 5:05 (nominal), 5:11, and 5:17 UT,  
 673 fixing the ending time to the nominal value (7:12UT). In (b) the ending time is set to 6:48, 7:00,  
 674 7:12 (nominal), 7:24, and 7:36 UT, fixing the starting time to the nominal value (5:05 UT). The  
 675 reference curve changes only slightly suggesting that the selection the excluding window is not a  
 676 crucial factor to calculate the VTEC anomalies for this case.

677

678 **Table 1.** List of the exclusion time windows, and the polynomial degrees optimized by the L-curve  
 679 method for individual satellites used in this study. Some satellites have 2 values for the polynomial  
 680 degrees<sup>1,2</sup> and the end of the exclusion windows<sup>3,4</sup>, applied for 2 different areas in Japan.

681

GPS satellite number	Degree of polynomial	Start of the exclusion window (UT)	End of the exclusion window (UT)
5	4	5:05  (common)	5:54
9	5 <sup>1</sup> and 7 <sup>2</sup>		6:30
15	2 <sup>1</sup> and 4 <sup>2</sup>		7:12
18	3		6:00
21	5		6:00
26	4		6:06 <sup>3</sup> and 6:25 <sup>4</sup>
27	5 <sup>1</sup> and 2 <sup>2</sup>		6:48
28	5		5:48

694 <sup>1</sup>for northern Hokkaido (north of 43.5N), <sup>2</sup>for other parts, <sup>3</sup>for stations east of 139.5E, <sup>4</sup>for stations  
 695 west of 139.5E

696

697           It should be noted that this study does not rely on the decay of the hole, which may last for  
698 hours, but avoid the spatial overlap of the hole with the LoS. This procedure enables us to isolate  
699 the VTEC anomalies caused by the earthquake robustly to a certain extent. Using the Figure 11a  
700 case, Figure 13b demonstrates that moving the ending time of the exclusion window by 24 minutes  
701 backward and forward let positive anomalies immediately before the earthquake change by only -  
702 3.7% and +10.8%, respectively. This suggests that the uncertainty in the ending time of a few tens  
703 of minutes is not crucial in isolating the preseismic VTEC anomalies.

704           For the satellites whose SIP does not go over the focal area (e.g. Sat. 18), I fixed the end  
705 of the excluding window at 10 minutes after the earthquake. For a few satellites (e.g. Sat.5 and  
706 Sat.28) with short postseismic VTEC data, I had to set up earlier end times for a part of stations  
707 (e.g. 5 minutes after the earthquake). I did not set up a specific elevation cut-off angle and assumed  
708 a thin layer at 300 km for STEC-VTEC conversion regardless of the elevations.

709           As for the point (3), the L-curve method is used to determine the optimum degree of  
710 polynomials curve (see Figure 7 of He and Heki, 2017). Root-mean-squares (rms) is calculated  
711 using the post-fit residuals outside the exclusion windows. Their dependences on the polynomial  
712 degree are shown in the left insets of Figure 11. The lower-left edge of the L-curve is considered  
713 to provide the most appropriate degree of polynomial to fit the VTEC changes. Table 1 also shows  
714 the degrees of polynomials for different satellites employed here. In Figure 11, the total time span  
715 of 5 hours is used for satellites 15 and 26 (the time spans are shorter for other satellites). The time  
716 spans also influence the best polynomial degree, i.e. the best degree tends to be higher for a longer  
717 time span. However, the shapes of the anomalies within the exclusion windows are not much  
718 influenced by the total time spans.

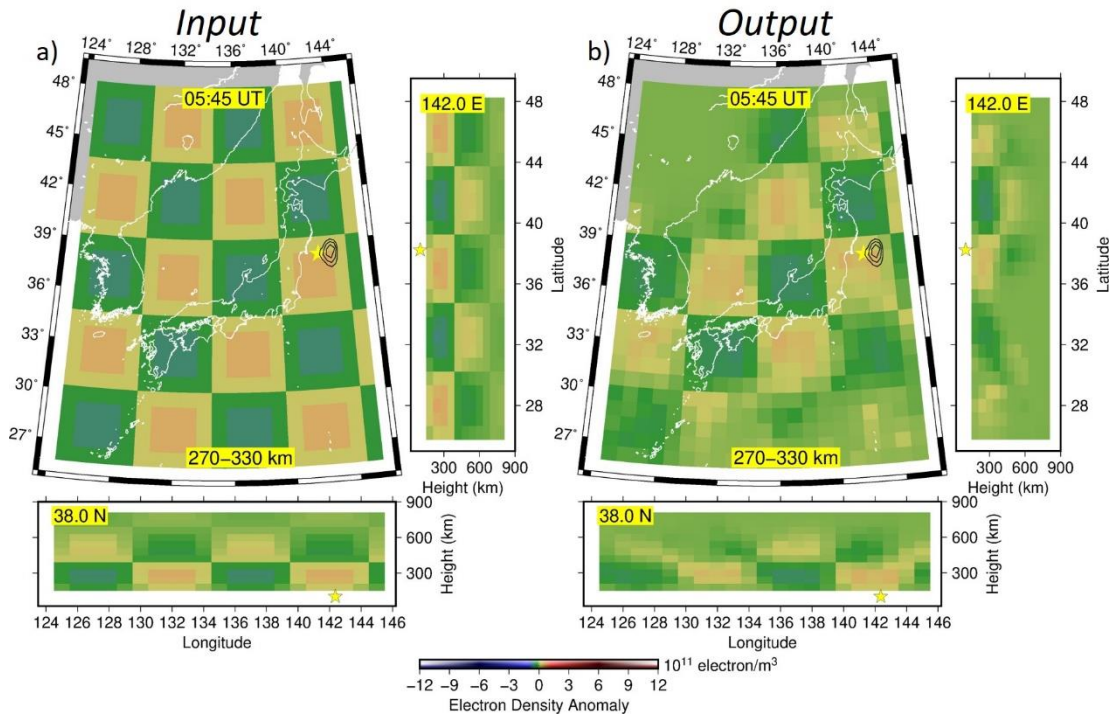
719           The departure from these reference curves (TEC anomalies) is used as the input for the 3D  
720 tomography calculation. In doing so, the VTEC anomalies were converted back to the STEC  
721 anomalies by dividing with cosine of the incidence angle of LoS to the 300 km layer. In short, I  
722 took advantage of VTEC for its simplicity in fitting the reference curves (because the apparent  
723 changes caused by elevation angle variations are already removed). However, the values after  
724 converting to STEC anomalies are used for 3D tomography.

725           As emphasized in Heki and Enomoto (2013) and He and Heki (2016), preseismic TEC  
726 anomalies take either positive or negative values. In Figure 11, I show examples of VTEC time-  
727 series showing positive and negative preseismic TEC anomalies with red and cyan curves,  
728 respectively. The difference would originate from the difference of the parts in ionosphere these  
729 LoS penetrate, i.e. the former would have penetrated more positive parts than negative parts of the  
730 electron density anomalies, and vice versa. The explanation on the variety of waveform of VTEC  
731 in penetrated LoS will be discussed in Chapter 5.

### 732 **3.3 Resolution tests**

733           For the 2011 Tohoku-oki earthquake case, ~6,800 blocks are set up over the Japanese  
734 Islands, the Sea of Japan, and the Korean Peninsula, with the size of  $1.0^\circ$  (east-west)  $\times$   $0.9^\circ$  (north-  
735 south)  $\times$  60 km (vertical) for altitudes 90-870 km (Figure 10). Now the dataset (VTEC residual) is  
736 ready, and the 3D tomography inversion could be performed to map the ionospheric electron  
737 density anomalies before the earthquake using the method explained in Chapter 2. However, it is  
738 often preferable to test the performance of the program and the resolution achieved by the available  
739 data set beforehand, by applying the program to synthetic data. Such a test is important to discuss

740 if the block size is appropriate. It is also important to know in which region the inversion results  
741 have enough resolution. This depends on spatial distribution of available LoS, i.e., it is essential  
742 that multiple LoS penetrate certain areas to infer the electron density anomalies there.



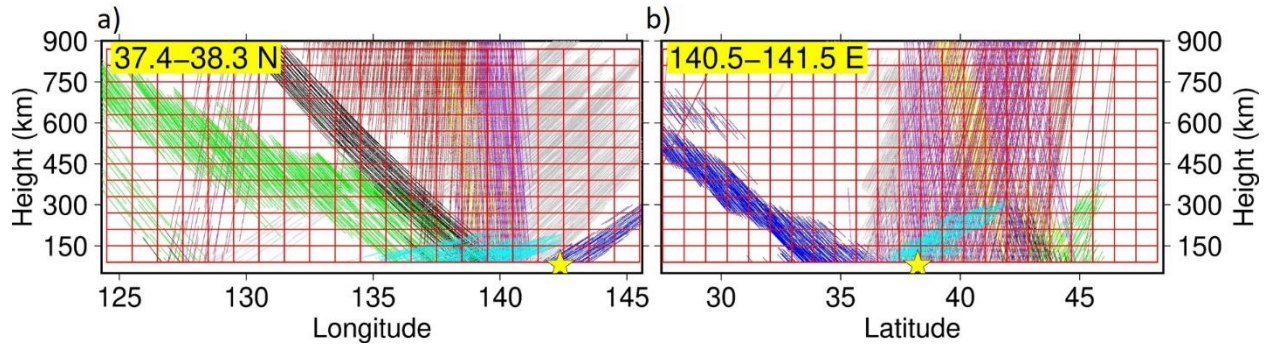
743  
744 **Figure 14.** The resolution test with the classical checkerboard pattern. The assumed electron  
745 density anomalies (a) and the output of the 3D tomography (b) are given in map view and north-  
746 south, east-west profiles.

747  
748 The accuracy of the 3D tomography can be assessed by performing the 3D tomographic  
749 inversion to recover artificial distribution of electron density anomalies using synthetic data. I first  
750 perform a test using the classical checkerboard pattern. I assumed the same satellite and station  
751 geometry as the epoch 05:45 UT on 2011 March 11, 1 minute before the Tohoku-oki earthquake,

752 to synthesize the input STEC data for the 3D tomography. In recovering the 3D distribution of  
753 electron density anomalies, I applied the constraints explained in the previous chapter.

754 Figure 14a shows the assumed checkerboard pattern. It is composed of the electron density  
755 anomalies of  $\pm 2.00 \times 10^{11}$  el/m<sup>3</sup>. I let the anomaly change gradually between the positive and  
756 negative parts to make the pattern consistent with the continuity constraint. I also assumed the  
757 amplitudes of the anomalies to decay in very high and low altitude to make it compatible with the  
758 constraint around zero with altitude-dependent tolerances, assumed proportional to the a-priori  
759 electron density profile predicted by the Chapman distribution.

760 Figure 14b shows the recovered pattern for the blocks at the altitude range 270-330 km.  
761 The pattern is well recovered particularly over the land (i.e. the Japanese Islands) and the offshore  
762 area within ~200 km from the coast, including the area above the rupture. Similarly, in the vertical  
763 section the resolution remains good in the altitudes 150-510 km, although the amplitudes of the  
764 recovered anomalies are ~2/3 of the input model possibly originating from the constraint around  
765 zero. On the other hand, resolution is poor where we do not have enough LoS penetrations (Figures  
766 10b and Figure 15). Such regions include the Pacific Ocean to the south of the rupture and the  
767 region above North Korea and Russia. The checkerboard-test generally shows a high performance  
768 of our 3D tomography in the region of interest. As suggested by Figure 15, vertical resolution is  
769 poor even above NE Japan for the highest layers of the blocks.

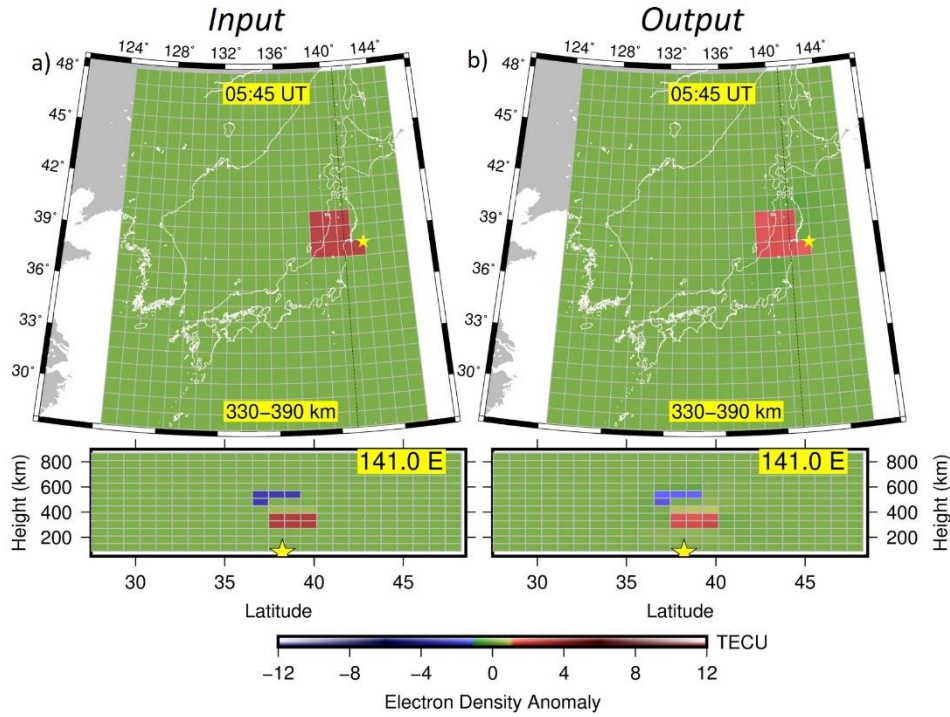


770

771 **Figure 15.** Vertical walls running east-west (a) and north-south (b) are assumed with the thickness  
 772 of one block, and the LoS penetrating those walls are plotted with lines with colours corresponding  
 773 to satellites (same colour as in Figure 10b, except for satellite 28 whose colour was changed into  
 774 cyan for visual clarity). Electron density anomalies of voxels penetrated by many LoS with  
 775 different angles are easier to be estimated than those penetrated by small number of LoS with  
 776 similar directions.

777

778 I next assessed the robustness of our result for later discussions on preseismic electron  
 779 density anomalies, by recovering patterns composed of a pair of positive and negative ( $\pm 3.00 \times$   
 780  $10^{11}$  el/m<sup>3</sup>) anomalies in low and high altitudes, respectively, in neutral background (Figure 16a).  
 781 The results (Figure 16b) well reproduced the assumed pattern of the positive anomaly again  
 782 reduced to  $\sim 2/3$  amplitude of the input model due to the constraints. Similarly, the positive and  
 783 negative anomaly patterns in the latitudinal profiles are well recovered with only weak smears in  
 784 surrounding blocks not exceeding a few percent of the assumed anomaly. The results of the two  
 785 resolution tests show that our 3D tomography results are accurate enough in the region of interest,  
 786 where the TEC anomalies appeared immediately before and after the 2011 Tohoku-oki earthquake.



787

788 **Figure 16.** Second resolution test for a pair of compact positive and negative anomalies above NE  
 789 Japan. The upper and bottom panels are horizontal view and latitudinal profile of the anomalies of  
 790 the assumed pattern (a) and the output of the 3D tomography (b).

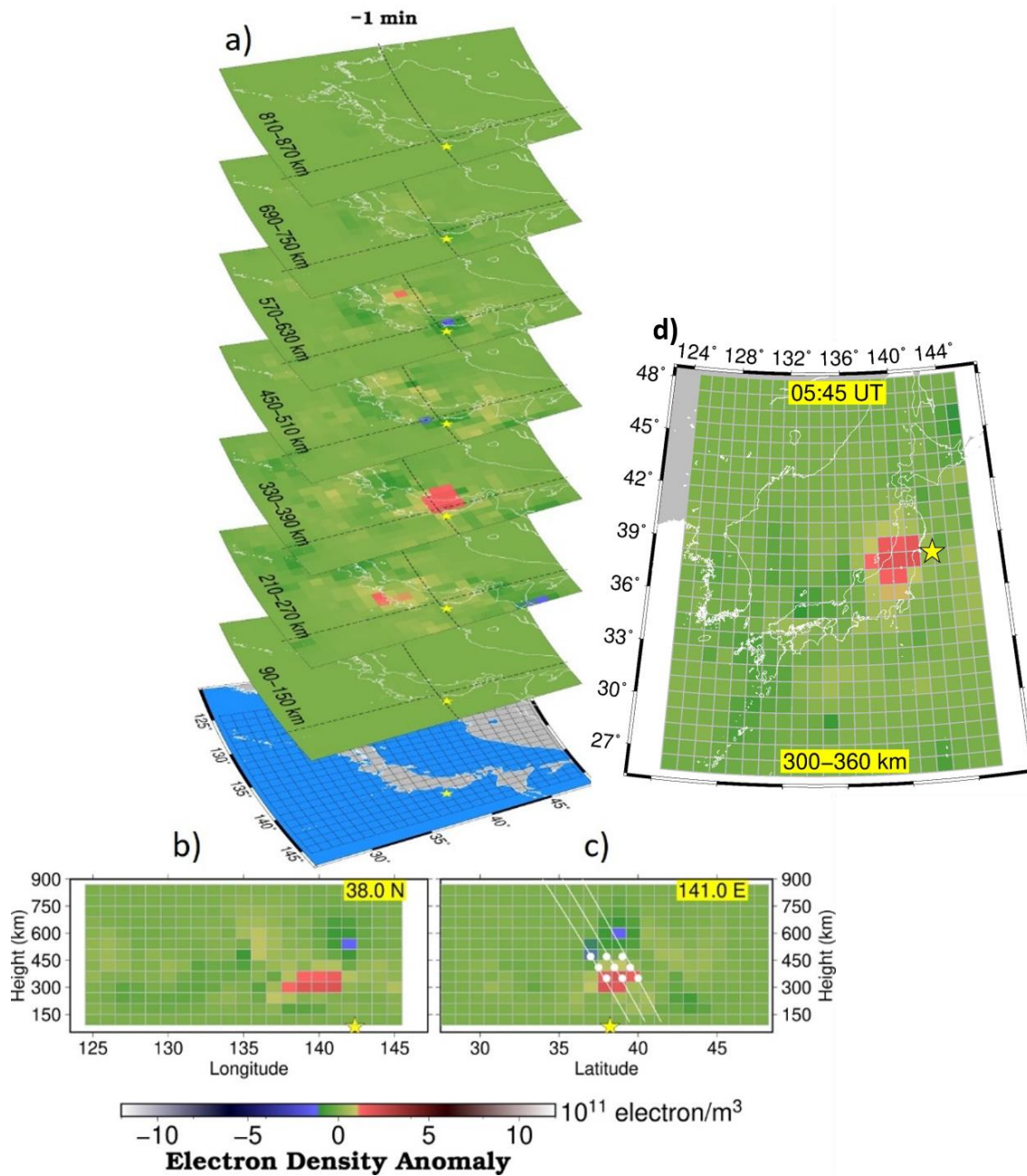
791

### 792 3.4 Tomography results

793 Figure 17a shows the map view of the 3D tomography result for altitudes of 90-870 km at  
 794 05:45 UT, 1 minute before the 2011 Tohoku-oki earthquake, with longitudinal and latitudinal  
 795 profiles. In Figure 18 I show the results at five epochs before the earthquake (40, 30, 20, 10, and  
 796 1 minute before the earthquake). I confirmed beforehand by resolution tests that the performance  
 797 of the tomography remains high for all these epochs. The results present that the strong positive  
 798 electron density anomalies occurred at 270-330 km and 330-390 km altitude layers and the  
 799 anomalies grow large without notable pattern change or spatial drifts toward the main shock. In

800 fact, the latitude of the voxel showing the largest positive anomaly stays around 38°N during the  
801 40 minutes period.

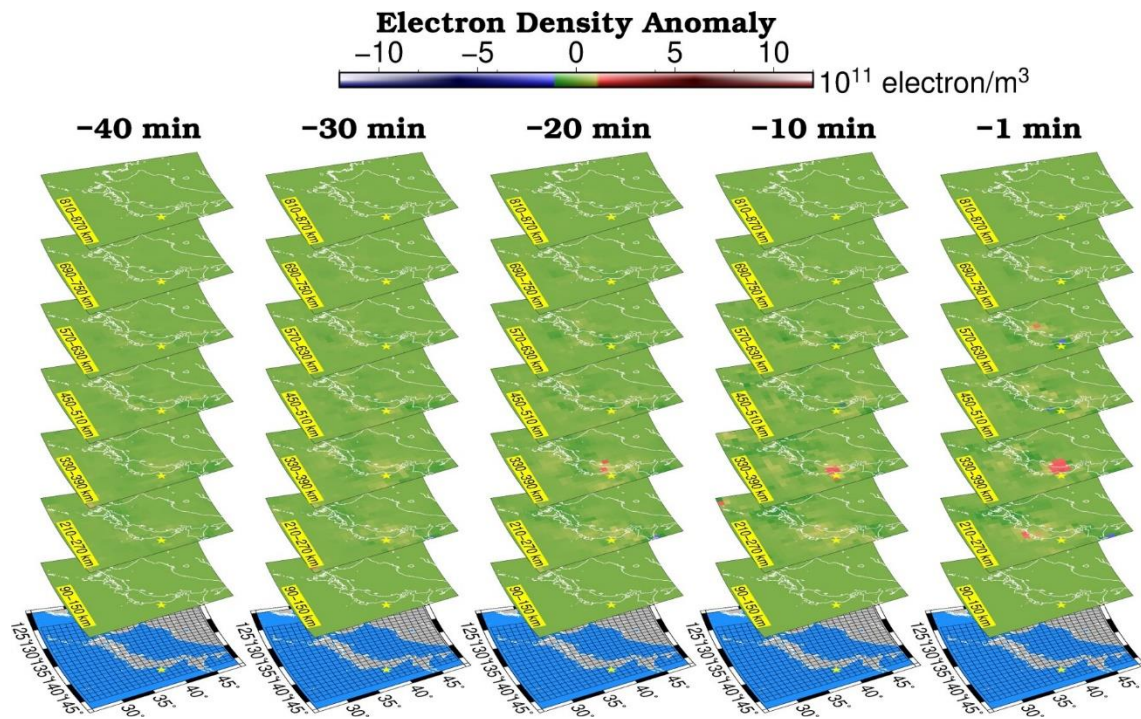
802



803

804 **Figure 17.** 3D tomography results of electron density anomalies 1 minute before the Tohoku-oki  
 805 earthquake (a). The east-west and north-south profiles are also shown in (b) and (c), respectively.  
 806 The white lines in (c) show the geomagnetic fields, and yellow stars show the latitude and  
 807 longitude of the epicenter. White circles in (c) show selected positions used to draw Figure 22.  
 808 The results for other epochs are given in Figure 18. An enlarged plan view showing positive  
 809 electron density anomaly is given in (d).

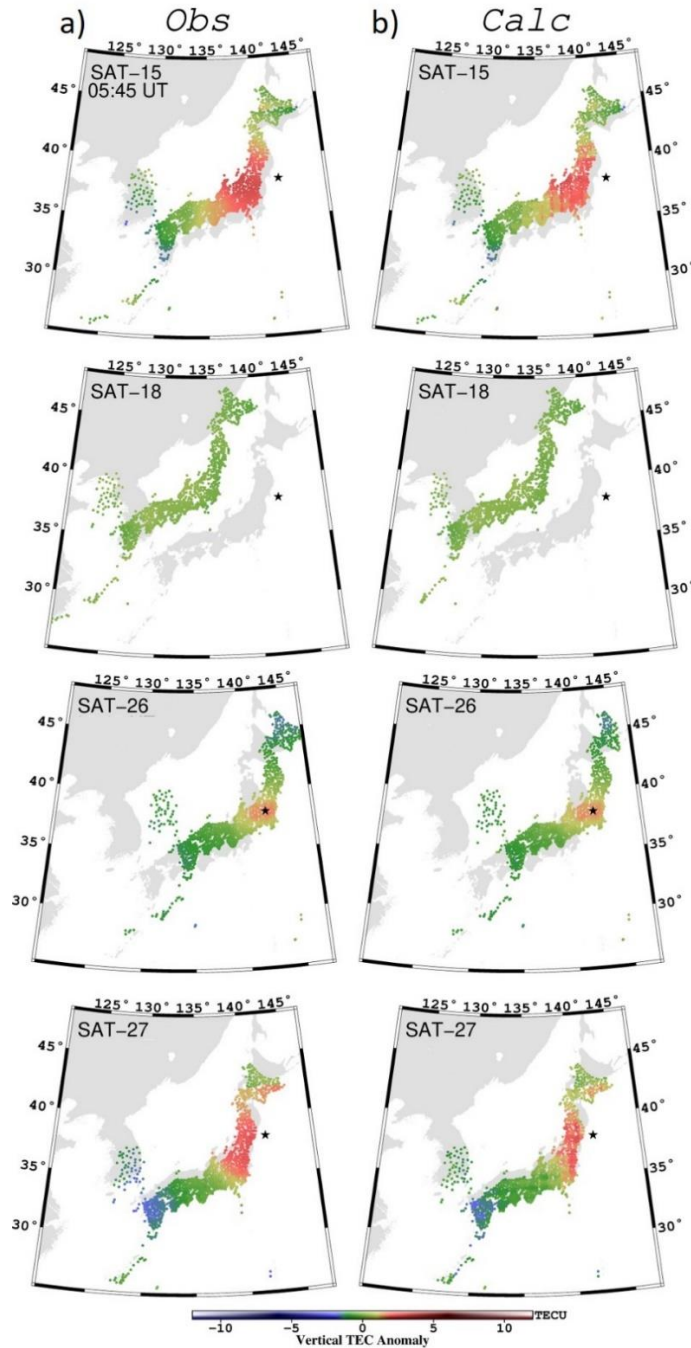
810 An important feature is that the positive anomaly lies above the land of NE Japan rather  
 811 than right above the focal area (Figure 17d). Its implication will be discussed later. The  
 812 longitudinal and latitudinal profiles (Figure 17b, c) show that the positive anomaly is the strongest  
 813 at altitude 270-390 km. Above this positive anomaly lies the negative anomaly at altitude ~600  
 814 km. These two anomalies are diffuse, and it is not very clear if they lie along the geomagnetic  
 815 field. Nevertheless, the pattern resembles to the earlier report for the 3D structure of the preseismic  
 816 anomalies of the 2015 Illapel earthquake (He and Heki, 2018), a pair of positive (height 150-225  
 817 km) and negative (height 450-525 km) anomalies located along the geomagnetic field.



818  
 819 **Figure 18.** 3D tomography results of electron density anomalies for altitudes 90-870 km at five  
 820 epochs, 40, 30, 20, 10, and 1 minute before the 2011 Tohoku-oki earthquake.

821

822           Figure 19 compares the observed and calculated anomalies for four satellites, 15, 18, 26,  
823 and 27, at the epoch 1 minute before the main shock. The “observed” anomalies (Figure 19a) are  
824 those obtained as the departure from the reference curves to VTEC time series, and they are plotted  
825 at their SIP. On the other hand, the “calculated” anomalies (Figure 19b) were derived as the sum  
826 of the products of the estimated electron density anomalies (Figure 17) and the penetration lengths  
827 of voxels along the LoS. Such calculated STEC anomalies are converted to VTEC for comparison  
828 with the observed anomalies. These two are expected to nearly coincide if the 3D tomography  
829 inversion is successful. We can see that the observed TEC anomalies are well reproduced by the  
830 estimated 3D electron density anomalies shown in Figure 17.

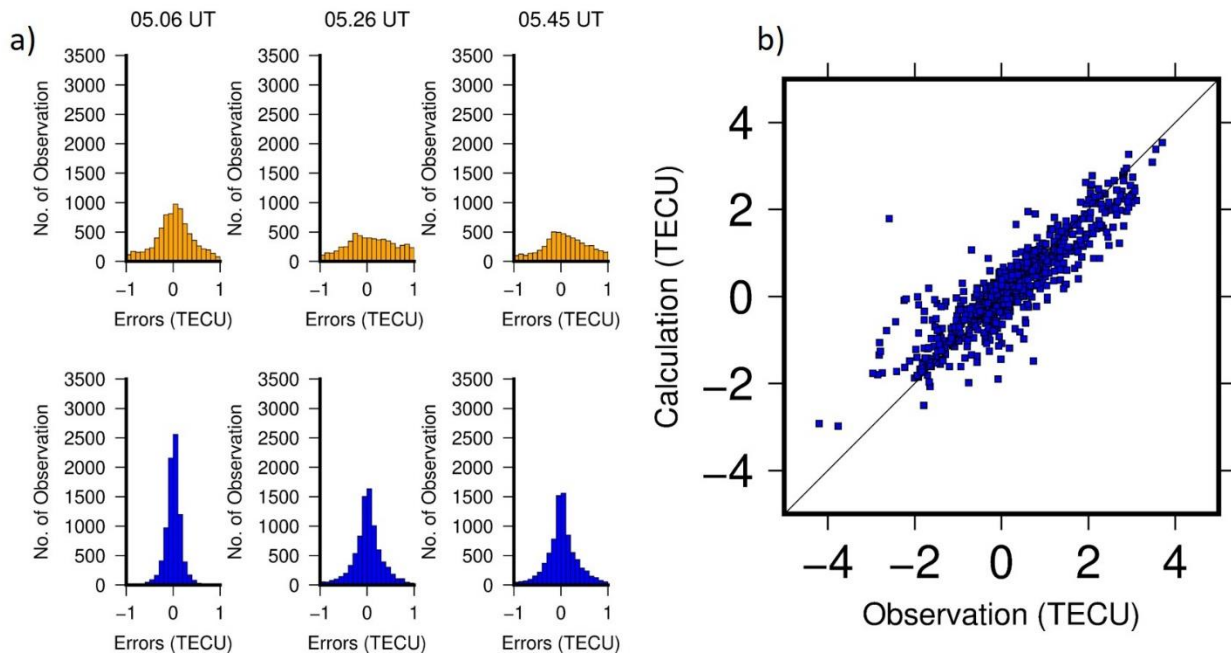


831

832 **Figure 19.** Comparison of the observed (a) and calculated (b) VTEC anomalies for 4 GPS satellites  
 833 at the epoch at 05:45 UT, 1 minute before the earthquake. They are mostly consistent with each  
 834 other showing that the estimated 3D electron density anomaly structure well explains the observed  
 835 TEC changes.

836           Next, I perform two additional assessments of the accuracy; (1) confirming the reduction  
837 of the variances of the original STEC anomalies to those of the post-fit residuals (the difference  
838 between the calculated and the observed values compared in Fig.19), and (2) checking the  
839 consistency of the subset data not used for 3D tomography with the result of the 3D tomography  
840 estimated using the rest of the data. Figure 20a shows the results of (1) for three different time  
841 epochs. Original STEC residuals have large variance around zero, but the post-fit STEC residuals  
842 of the 3D tomography show much reduced scatter around zero. Together with Figure 19, this would  
843 imply that the estimated 3D distribution of the electron density anomalies well explains the  
844 observed STEC.

845           Figure 20b shows the result of a validation test for the epoch 05:45 UT. I removed  
846 randomly selected 10% of the original input data as the validation data subset. Next, I used the  
847 remaining 90% as the input to our 3D tomography method. Then, I calculated the STEC for the  
848 removed 10% subset using the estimated 3D electron density anomaly distribution. They are  
849 expected to coincide with each other. Figure 20b shows that the coincidence is as good as ~0.51  
850 TECU.



851

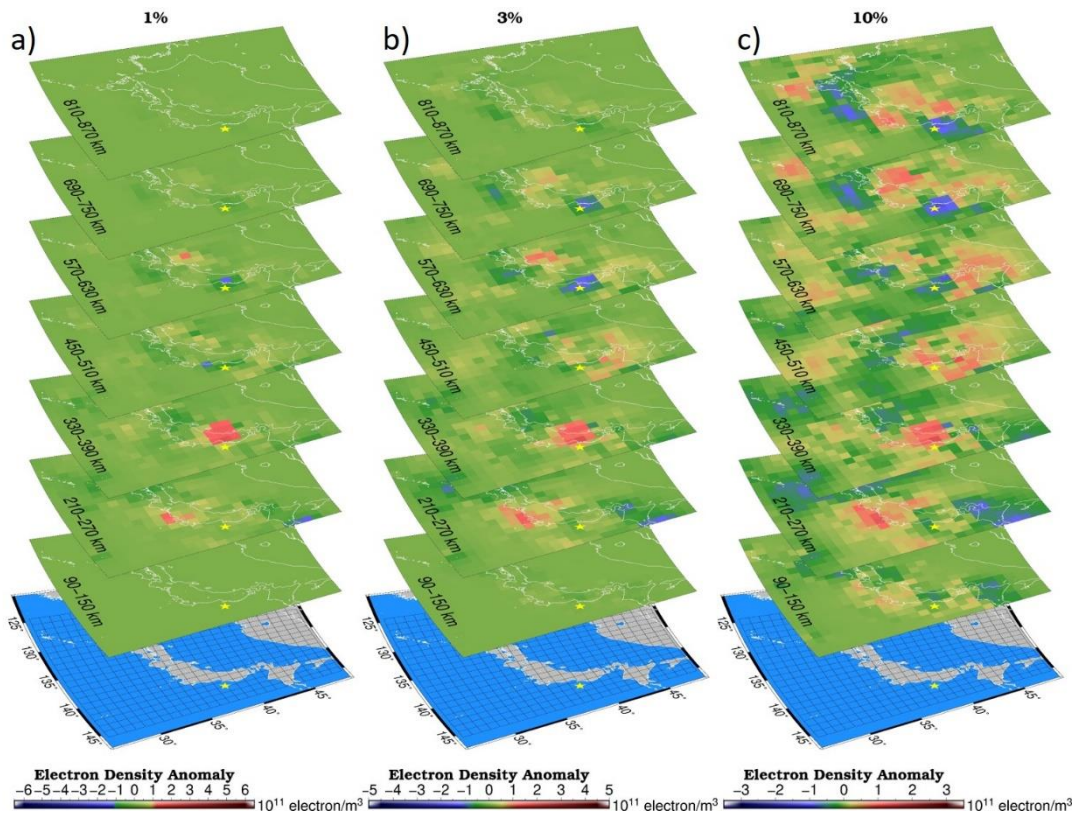
852 **Figure 20.** (a) The histograms of the STEC input to the 3D tomography (upper panel in orange),  
 853 and the post-fit residuals (lower panel in blue) at three-time epochs (40 minutes, 20 minutes, and  
 854 1 minute before earthquake). (b) Comparison between the randomly removed 10% subset of the  
 855 observed STEC data at 05:45 UT (horizontal axis) and those calculated using the 3D electron  
 856 density anomalies estimated with the remaining 90% data (vertical axis). The rms of the scatter  
 857 around the 45 degrees line is  $\sim 0.51$  TECU.

858

859 Figure 21 compares the tomography results based on three different settings of the  
 860 constraint around zero, i.e., 1, 3, 10% of the Chapman distribution. It can be seen that the positive  
 861 anomaly  $\sim 300$  km high and negative anomaly  $\sim 600$  km high persistently appear for those solutions.  
 862 At the same time, a weaker constraint tends to yield complicated patterns in layers near the top of  
 863 the blocks.

864 In Figure 15, I showed the distribution of the LoS connecting ground GNSS stations and  
 865 the GPS satellites penetrating the vertical walls running east-west (a) and north-south (b) with the

866 one-block thickness. We can see that blocks with altitude up to 600 km above NE Japan are  
867 penetrated by many LoS with multiple satellites having different penetration angles. On the other  
868 hand, the highest layers are penetrated only by nearly vertical LoS, suggesting difficulty in  
869 constraining altitudes of electron density anomalies there. I think that such irregular anomalies  
870 emerging in the highest layers for weak constraint cases are not real.



871  
872 **Figure 21.** 3D tomography results of electron density anomalies at the epoch 1 minute before the  
873 mainshock with different strength of constraints around zero, i.e. 1 % (a), 3 % (b), and 10 % (c) of  
874 the Chapman distribution of the electron density.

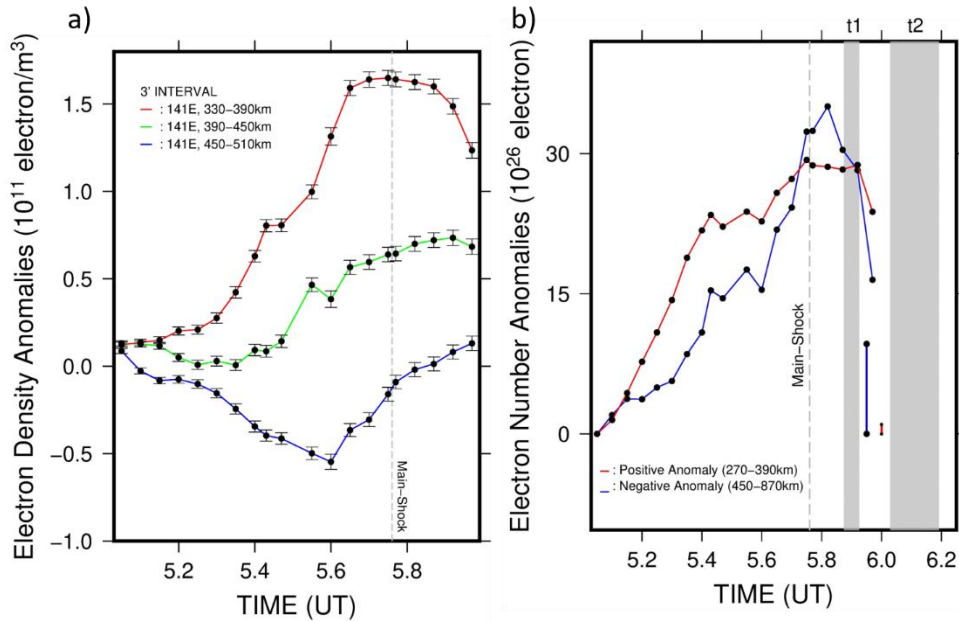
875

### 876 **3.5 Growth and polarity balances of the preseismic anomalies**

877 To further study the evolution of the electron density anomalies immediately before the  
878 earthquake, in Figure 22a, I plot the electron density anomalies at points with three different  
879 altitudes, 330-390 km, 390-450 km, and 450-510 km (white circles in Figure 17c) connected with  
880 the geomagnetic field. The three altitudes correspond to the center of positive anomaly, middle  
881 point between the positive and negative anomalies, and the center of negative anomaly,  
882 respectively.

883 Figure 22a shows the averages of three blocks at low, medium, and high altitudes every 3  
884 minutes before and after the earthquake. The positive anomalies show larger values than negative  
885 anomalies. However, this does not necessarily mean the dominance of the spatially integrated  
886 positive anomalies. Figure 22b indicates the total amount of positive and negative electron density  
887 anomalies obtained by integrating them in space. They are well balanced, suggesting that the  
888 growth of the anomalies occurred as the electron transport rather than net increase or decrease of  
889 electrons.

890 The build-up of the positive and negative anomalies starts ~40 minutes before the  
891 earthquake. They grow until ~20 minutes before the main shock and remain nearly constant until  
892 the earthquake. After the earthquake, the anomalies remain stationary for ~10 minutes and start to  
893 decay. I have no idea on the fluctuations of the curve around 5.4-5.6 UT and sudden increase of  
894 the negative anomaly after 5.6 UT in Figure 22b. They may reflect a certain instability coming  
895 from the VTEC observation errors. It should be noted that I did not perform in our tomography  
896 any temporal smoothing which would be an effective remedy to reduce such instability.



897

898 **Figure 22.** (a) The evolution of the average estimated electron density anomalies of the three  
 899 different blocks at the 3 altitudes, 360 km, 420 km, 480 km (see Fig.17c for positions), with 3-  
 900 minutes interval. The error bars are the average of the formal errors of the 3 voxels sampled at the  
 901 3 altitudes. (b) shows the integrated amount of positive and negative anomalies at lower (270-390  
 902 km) and higher (450-870 km) altitude voxels, respectively. To the right side of (b), I show the  
 903 spatially integrated increase in negative (blue) and positive (red) postseismic electron density  
 904 anomalies measured as the difference between the two periods shown in grey squares (see Figure  
 905 34 in Chapter 5).

906

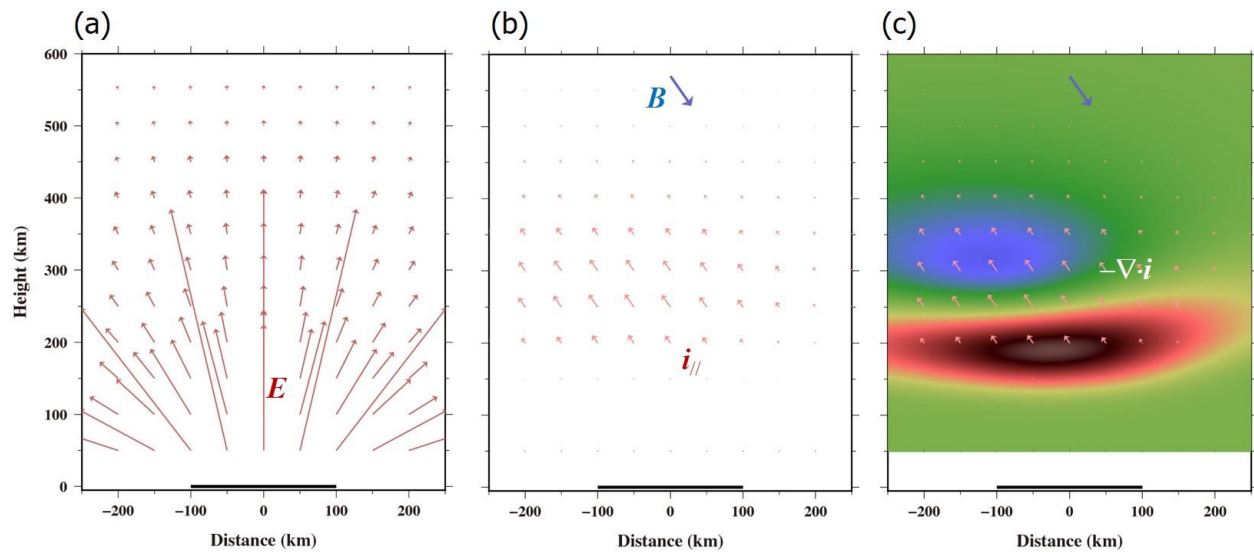
### 907 3.6 Discussion on the physical mechanism of the preseismic anomalies

908 The result showed that the total amounts of the positive and negative electron density  
 909 anomalies increased in a similar manner (Figure 22b) suggesting little changes in the total number  
 910 of electrons in the preseismic stage. Hence, such changes would have occurred without net increase  
 911 or decrease of electrons, e.g., by electron transportation, rather than enhanced ionization  
 912 (generation of new free electrons) or recombination (loss of free electrons).

913 Another important fact is that the strong positive anomalies before the 2011 earthquake  
914 emerge only above land (Figure 17d). This suggests that the electron redistribution is due to electric  
915 fields made by surface electric charges. Such surface charges would be relatively stable on land,  
916 but they diffuse rapidly in the ocean due to high electric conductivity of sea water (areal density  
917 of the surface charges would be determined by the balance between the production at depth and  
918 the diffusion at the surface). Considering these features, I discuss possible physical mechanisms  
919 connecting the surface electric charges to the preseismic ionospheric electron redistributions.

920 Two hypotheses have been proposed before to explain how surface electric charges  
921 redistribute ionospheric electrons. Kuo et al. (2014) showed that the anomaly can be generated by  
922 an upward electric current from stressed rock. This leads to the westward Hall electric field  $E$ .  
923 This  $E$ , together with the geomagnetic field  $B$ , drives downward  $E \times B$  drift of the ionospheric  
924 plasma and makes a pair of positive and negative electron density anomalies. This model, however,  
925 needs large electric fields near ground to let substantial electric current flow through the highly  
926 resistive lower atmosphere. Kelley et al. (2017) proposed that the  $E \times B$  drift could be driven  
927 directly by electric fields made by surface electric charges. Their model needs the surface electric  
928 fields only  $\sim 1/500$  of the fair-weather field to produce the anomalies observed before the 2011  
929 Tohoku-oki earthquake.

930



931

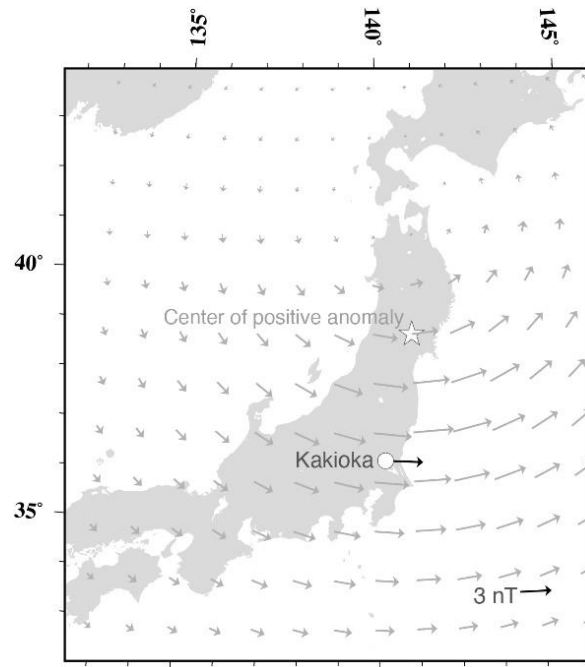
932 **Figure 23.** A two-dimensional image of the preseismic electron redistribution by surface electric  
 933 charges. (a) Positive charges distributed on the surface (grey line at the bottom) make upward  
 934 electric field  $E$ , and (b) the component parallel with the geomagnetic field  $B$  exerts electromotive  
 935 forces and drives electric current  $i_{//}$  along the geomagnetic field where there are enough free  
 936 electrons. (c) Convergence and divergence of the electron flow makes positive (red) and negative  
 937 (blue) electron density anomalies, respectively. This is a qualitative model, and scales to convert  
 938 the illustrated quantities to real values are not given.

939

940 Muafiry and Heki (2020) proposed a new model focusing on the induced polarization, that  
 941 would occur together with the process proposed by Kelley et al. (2017). Figure 23 qualitatively  
 942 illustrates the idea. Electric fields  $E$  made by surface charges would reach the ionosphere (Figure  
 943 23a). The field generates electromotive forces and makes electrons move along geomagnetic  
 944 fields. If surface charges are positive, electron movements will be downward, and the current will  
 945 be upward ( $i_{//}$  in Figure 23b). The current will continue until the induced electric field cancels the  
 946 external field made by surface charges, making the electric potential uniform along the magnetic  
 947 field. The current will depend on the along- $B$  component of the external electric field and the  
 948 density of free electrons as a function of altitude. The non-uniform electric currents would result  
 65

949 in convergence/divergence of electrons and make positive/negative electron density anomalies at  
950 the lower/higher ionosphere along the magnetic field (Figure 23c), the structure found in Chile  
951 (He and Heki, 2018) and in Japan (this thesis) by the 3D tomography.

952 The model is qualitative, and it is not supposed to give actual figures for quantities such as  
953 areal density of surface charges and  $E$ . This stems from the limitation of the GNSS-TEC method,  
954 i.e., GNSS can sense only electrons and cannot count positive ions. In fact, substantial amount of  
955 positive ion would move together with electrons to keep the plasma “nearly” neutral (there should  
956 be deviation from neutral, however, to cancel the external electric fields by the induced fields). In  
957 short, the 3D tomography results do not allow us to directly infer  $E$  or  $i_{//}$ .



958

959 **Figure 24.** Magnetic field on the surface caused by the upward current along geomagnetic field  
960 above the star (the center of the positive anomaly), equivalent to cause  $\sim 0.15$  of electron transport  
961 given in Figure 7b from altitude 330 km to 600 km. This makes disturbing field of  $\sim 3$  nT eastward  
962 at the Kakioka station, consistent with those reported in Heki and Enomoto (2013).

963           One external test of the model might come from the magnetic fields possibly generated by  
964 the upward current along B ( $i_{//}$  in Figure 23b). Such a current would make eastward magnetic fields  
965 on surface, mainly in the region to the south of the epicenter (Figure 24). As discussed above, the  
966 electron density anomalies as revealed by 3D tomography (Figures 17) only reflect the electron  
967 redistribution, and the net current would depend on the movements of positive ions. I drew Figure  
968 24 assuming an arbitrary current, to let  $4.5 \times 10^{26}$  electrons ( $\sim 0.15$  of the amount in Figure 22b)  
969 flow along a thin line extending from the center of positive electron density anomaly at 330 km  
970 altitude upward along the magnetic field to 600 km altitude in 40 minutes. Then the Bio-Savard's  
971 law predicts the eastward field of  $\sim 3$  nT in the Kanto District (Figure 24). This nearly coincides  
972 with the change in declination observed at the Kakioka observatory in Kanto (relative to Kanoya  
973 in Kyushu) starting  $\sim 40$  minutes before the earthquake as reported in Figure 4 of Heki and  
974 Enomoto (2013). Anyway, the assumption is arbitrary (the value 0.15 does not have a theoretical  
975 basis), and Figures 23 and 24 just provide a rough sketch illustrating how the induced polarization  
976 occurs.

977           It is also assumed that the declination change at Kakioka (Heki and Enomoto, 2013) was  
978 not a regular space weather phenomenon. It should be born in mind, however, that the 2011  
979 Tohoku-oki earthquake occurred during a magnetic storm. So, a careful study is needed to attribute  
980 the observed declination changes to the ionospheric electron redistribution process as proposed in  
981 this study. It would be also important to detect magnetic field changes immediately before many  
982 other large earthquakes to draw a more realistic picture of the whole process.

983

984 **Chapter 4: 3D Tomography of the Ionospheric Anomalies Before the 2010**

985 **Maule Earthquake, Chile: Comparison with the 2011 Tohoku-oki and 2015**

986 **Illapel Earthquake**

987

#### 988 **4.1 Introduction: Structure of preseismic ionospheric anomalies**

989 In this chapter, the short-term preseismic ionospheric anomalies before the 2011 Tohoku-  
990 oki earthquake is compare with other earthquakes for the sake of better understanding of their  
991 features. So far, we studied examples of the 3D distributions of ionospheric electron density  
992 anomalies immediately before two large earthquakes, i.e. 2011 Tohoku-oki ( $M_w$ 9.0, this thesis)  
993 and 2015 Illapel earthquake, central Chile ( $M_w$ 8.3, He and Heki, 2018). Both cases show a  
994 common structure, lower positive and higher negative electron density anomalies. Their vertical  
995 profiles suggest that the altitudes of the positive and negative anomalies before the 2011  
996 earthquake (~300 and ~600 km) are somewhat higher than those of the 2015 earthquake (~200 and  
997 ~500 km).

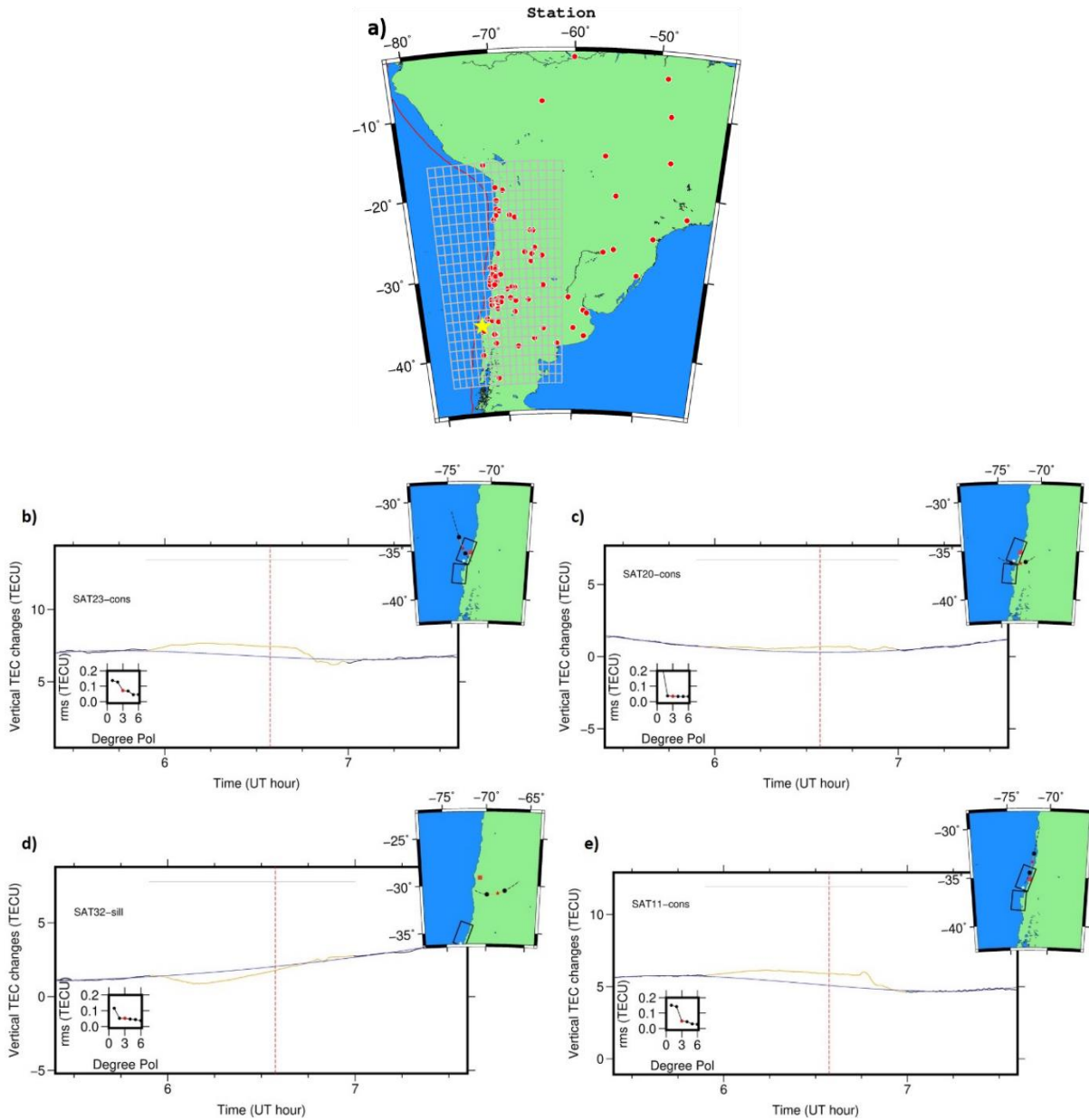
998 On the other hand, horizontal extents of anomalies are little different in the two cases, i.e.  
999 the positive anomalies of 2011 lie within circles with diameter of ~300 km above the land region  
1000 and not above the epicenter (off-shore). This strongly supports the physical model presented in the  
1001 previous chapter that electric charges on the land surface redistributed ionospheric electrons.  
1002 Regarding the 2015 Illapel earthquake, its epicenter is close to the coast, and such a feature, e.g.  
1003 lack of the anomaly above the ocean, is not clear.

1004 In this chapter, I analyze the 3D structure of the preseismic ionospheric anomaly of the  
1005 2010  $M_w$  8.8 Maule earthquake, another M9-class earthquake occurred in central Chile ~1 year  
1006 before the 2011 Tohoku-oki earthquake. I follow the same 3D tomography approach employed in  
1007 He and Heki (2018) and this thesis.

1008 **4.2 Data set**

1009           In the morning (03:34 in local time) of 27 February 2010, a Mw8.8 earthquake ruptured  
1010 the Topocalma, Carranza, and Arauco segments of the Chilean subduction zone (Jara-Munoz et  
1011 al., 2015). The epicenter of this Maule earthquake is located at the geographic latitude of 35.9°S  
1012 (geomagnetic latitude of 36.1°S), and He and Heki (2016) reported that the geomagnetic activity  
1013 was low before and after this earthquake. Here I use the GNSS-TEC data extracted from raw  
1014 RINEX data files obtained at 89 permanent GNSS stations in South America (Figure 25). The  
1015 TEC data from six GPS satellites (11, 13, 17, 20, 23 and 32) are used. The spatial coverage of  
1016 the GNSS stations is not so good as in the 2015 Illapel earthquake case (He and Heki, 2018)  
1017 because many of the stations used there were not operating in 2010. The station density is much  
1018 lower than the 2011 Tohoku-oki case (this thesis).

1019



1020

1021 **Figure 25.** Maps showing the GNSS station distribution (red dots) and the voxels for 3D  
1022 tomography above the middle South-America (a). Yellow star indicates the epicenter of the 2010  
1023 Maule ( $M_w$ 8.8) Earthquake. A red curve illustrates the Peru-Chile Trench, the boundary between  
1024 the Nazca and the South American Plates. Panels (b-e) show VTEC time series (yellow curves)  
1025 and reference curves by best-fit polynomials (blue curves) for satellite-receiver pairs with four  
1026 GPS satellites, i.e. Sat.23-CONS (b), Sat.20-CONS (c), Sat.32-SILL (d), and Sat.11-CONS (e).  
1027 Insets of (b-e) show the behaviour of the residuals for the change of the polynomial degrees (L-  
1028 curve method to optimize the degree). See the caption of Figure 11 for other symbols.

### 1029 **4.3 Data processing strategy**

1030           The 3D tomography input data are the STEC residuals (converted from VTEC) from  
1031 available station-satellite pairs with LoS penetrating the voxels. I followed the procedure  
1032 described in Chapter 3.3 of this thesis. I first calculate the absolute VTEC for each pair by  
1033 multiplying the de-biased STEC with the cosine of the incidence angle of LoS into a thin shell at  
1034 300 km altitude from the surface. The inter-frequency biases (station and satellite biases) are  
1035 removed beforehand. The satellite biases are extracted from the header of the Global Ionosphere  
1036 Maps (GIM) downloaded from [aiub.unibe.ch/CODE](http://aiub.unibe.ch/CODE). The receiver biases were estimated so that  
1037 the scatters of VTEC during the stable local time (from midnight to dawn) are minimized  
1038 (minimum scalloping).

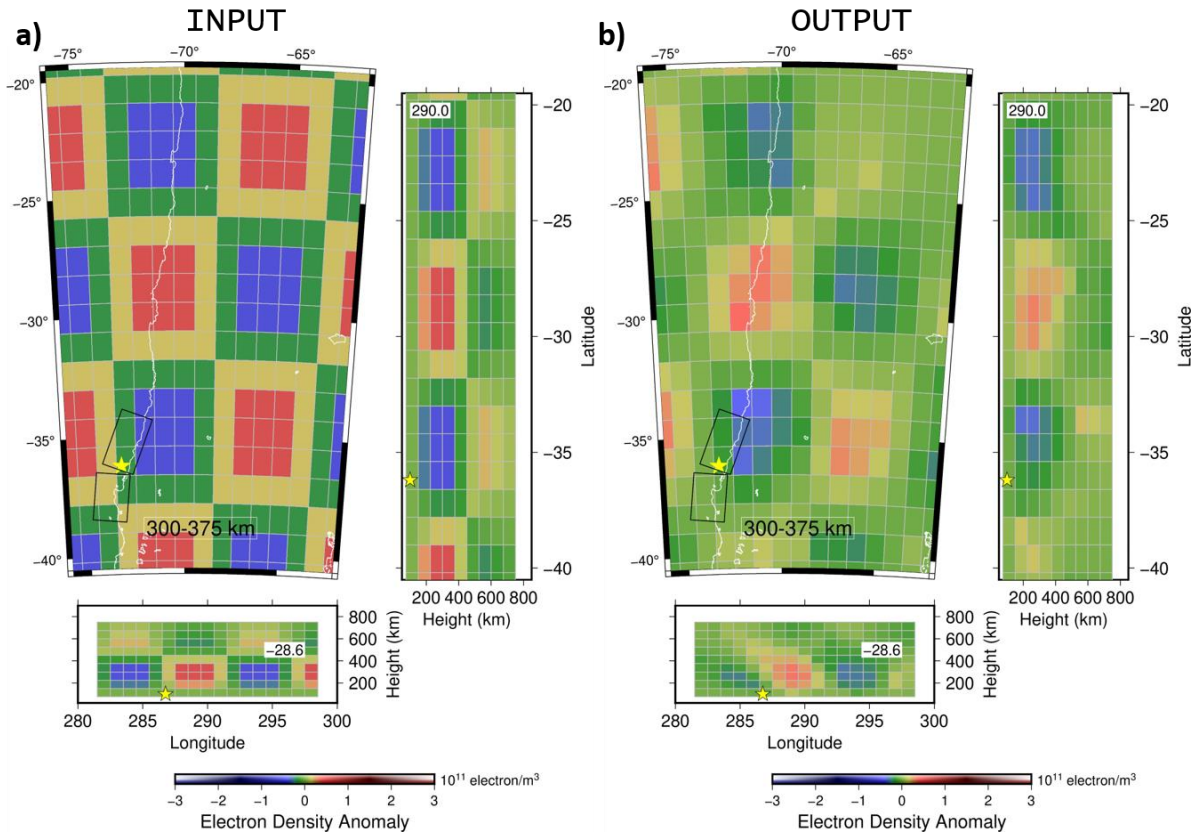
1039           The VTEC anomaly is obtained as the difference between the observed VTEC and  
1040 reference curves estimated as polynomials whose degree is optimized by the L-curve method  
1041 (selection of best degree of polynomial). The exclusion time-window was used in estimating the  
1042 reference curves. The window starts from 40 minutes before the main shock following the  
1043 detection of the bending done in Heki and Enomoto (2015) using AIC. As for the end time of the  
1044 exclusion window, I employed 07:00 UT when the SIP trajectories of GPS-23 and GPS-20 left the  
1045 focal region (Figure 25b and 25c), i.e. the position of the expected postseismic ionospheric hole.  
1046 For the remaining GPS satellites, I used the same settings because this window worked fine for  
1047 those satellite, too. VTEC residuals were converted back to STEC residuals by dividing with the  
1048 cosine of the incidence angle that were used to convert the de-biased STEC to VTEC.

1049 **4.4 Resolution test**

1050 I set up the voxels for the 3D tomography of the electron density anomalies before and  
1051 after the 2010 Maule earthquake. The 792 blocks are distributed above South America, with the  
1052 size of  $1.0^\circ$  (east-west)  $\times$   $1.2^\circ$  (north-south)  $\times$  75 km (vertical) for the altitude range 75-750 km  
1053 (Figure 25).

1054 The distribution of LoS and the block size are important factors for the accuracy of the  
1055 tomography results. Before performing 3D tomography using the real STEC residual data, I first  
1056 perform tests with synthetic data to recover artificial distribution of electron density anomalies to  
1057 evaluate the accuracy of the method. I employ the classical checkerboard pattern for the resolution  
1058 test. I assumed the same satellite and station geometry as the epoch 06:33 UT, 1 minute before the  
1059 earthquake, to synthesize the input STEC data for the 3D tomography. In recovering the 3D  
1060 distribution of electron density anomalies, I applied the same constraints as the 2011 Tohoku-oki  
1061 case (continuity constraint and constraint around zero with altitude-dependent tolerance) as  
1062 explained in the previous chapter.

1063 Figure 26a shows the assumed checkerboard pattern. It is composed of the electron density  
1064 anomalies of  $\pm 2.00 \times 10^{11}$  el/m<sup>3</sup>. I let the anomaly change gradually between the positive and  
1065 negative parts to make the pattern consistent with the continuity constraint. I also assumed the  
1066 amplitudes of the anomalies to decay in very high and low ionosphere to make it compatible with  
1067 the other constraint.



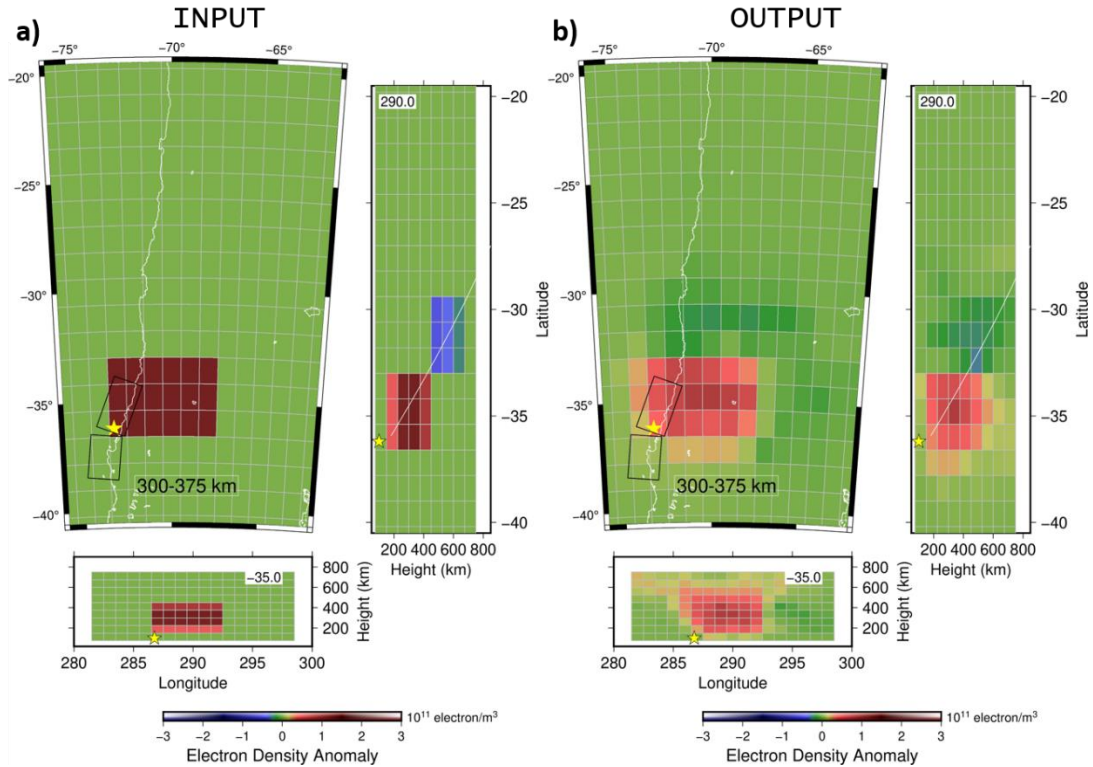
1068

1069 **Figure 26.** The resolution test of the 3D tomography of ionospheric electron density anomalies  
 1070 before the 2010 Maule earthquake, central Chile, with the classical checkerboard pattern. The  
 1071 assumed electron density anomalies (a) and the output of the 3D tomography (b) are given in map  
 1072 view and north-south, east-west profiles. The yellow stars indicate the position of the epicenter of  
 1073 the earthquake. Black rectangles is an approximate rupture area.

1074

1075 Figure 26b shows the recovered pattern for the blocks at the altitude range 300-375 km.  
 1076 The pattern is well recovered particularly over the land and the offshore area within ~100 km from  
 1077 the coast, including the area above the rupture. Similarly, in the vertical section the resolution  
 1078 remains good in the altitudes 150-525 km, although the amplitudes of the recovered anomalies are  
 1079 ~1/3 of the input model due possibly to the constraint around zero. On the other hand, resolution

1080 is poor where LoS do not penetrate the voxels (Figure 30). Such regions include the northeastern  
1081 part of the studied area.



1082

1083 **Figure 27.** The second resolution test for a pair of positive and negative anomalies above middle  
1084 of South America. The upper, bottom, and right panels are horizontal view, longitudinal and  
1085 latitudinal profiles of the anomalies of the assumed pattern (a) and the output of the 3D tomography  
1086 (b). Black rectangles is an approximate rupture area.

1087

1088 I next assessed the robustness of our result by recovering patterns composed of a pair of  
1089 positive and negative ( $\pm 2.30 \times 10^{11}$  el/m<sup>3</sup>) anomalies in low and high altitudes along the  
1090 geomagnetic field, respectively, in neutral background (Figure 27a). The results (Figure 27b) well  
1091 reproduced the assumed pattern of the positive anomaly again reduced to  $\sim 2/3$  amplitude of the  
1092 input model due to the constraint.

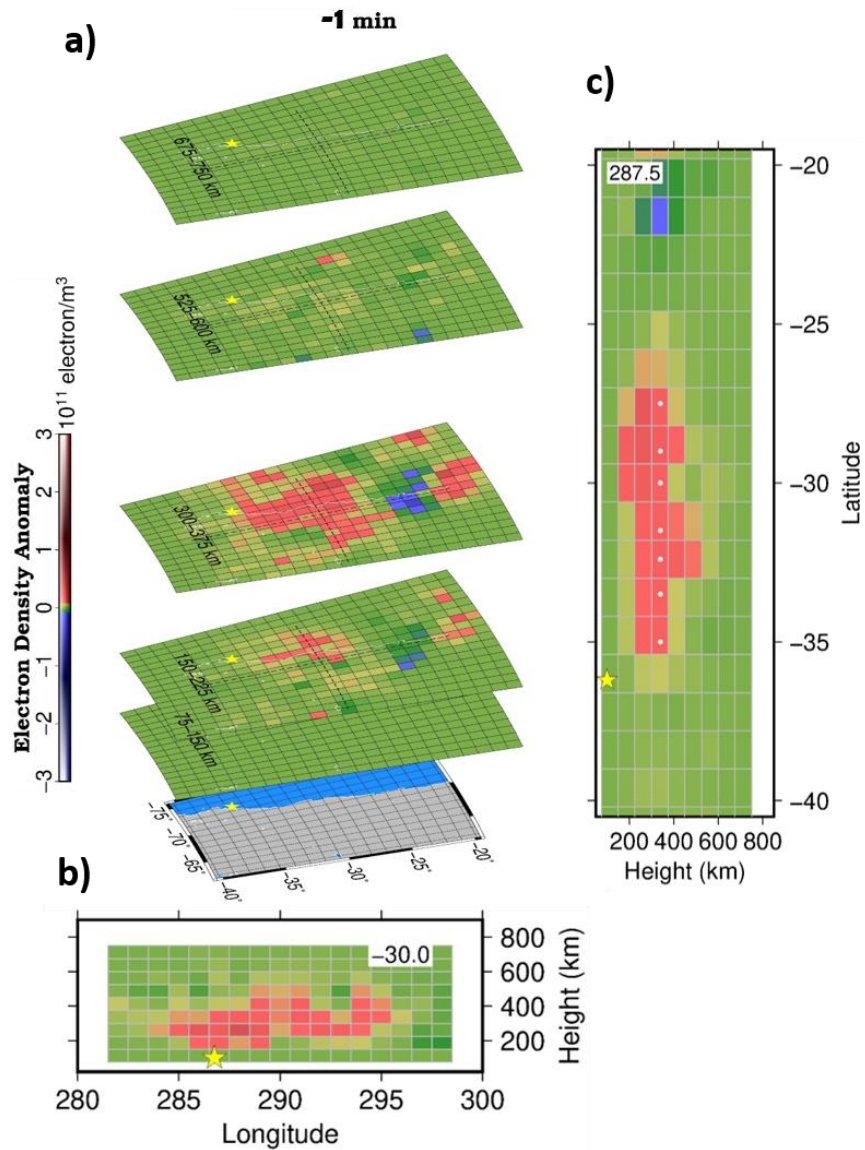
1093            However, the high-altitude negative anomaly pattern in the latitudinal profile is not well  
1094 recovered. This indicates the limited availability of LoS is in the region where the negative  
1095 anomaly is supposed to appear (Figure 30). The results of the two resolution tests show that our  
1096 3D tomography results are accurate enough in a part of the region of interest, i.e., where the  
1097 positive TEC anomalies are expected to emerge immediately before the 2010 Maule earthquake.  
1098 However, it would be difficult to identify the negative anomaly expected to emerge at a higher  
1099 altitude.

1100

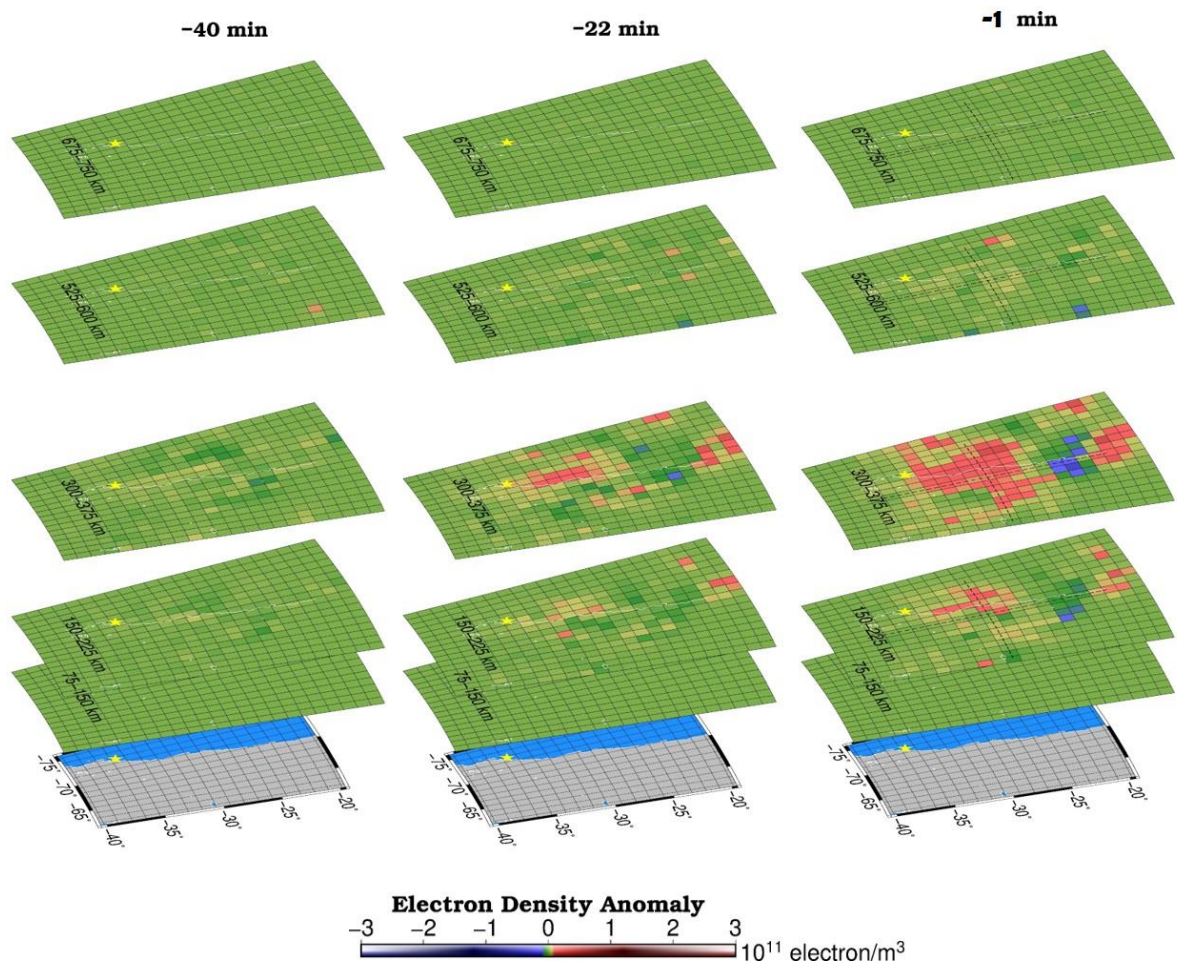
#### 1101     **4.5 Tomography result**

1102            Figure 28 shows the map view of the 3D tomography result for altitudes of 75-750km at  
1103 06:33 UT, 1 minute before the 2010 Maule earthquake, together with longitudinal and latitudinal  
1104 profiles. Figure 29 shows the results at three epochs before the earthquake (40, 22 and 1 minutes  
1105 before the earthquake). I confirmed beforehand that the performance of the tomography 40 and 22  
1106 minutes before earthquake remains comparable to that 1 minute before earthquake shown in  
1107 Figures 26 and 27. The results present that the strong positive electron density anomalies occurred  
1108 at the 225-375 km altitude layers and the anomalies grow large without notable pattern change or  
1109 spatial drifts toward the main shock. In fact, the latitude of the voxel showing the largest positive  
1110 anomaly stays around 28°N during the 40 minutes period. The high-altitude negative electron  
1111 density anomaly is not clear in this result. Figure 30 shows the LoS distributions in EW and NS  
1112 profiles where the negative anomaly is supposed to appear. In comparison with Figure 15 for the  
1113 2011 Tohoku-oki earthquake, it can be seen that there are not enough number of paths penetrating

1114 voxels in those areas. This is because the GNSS stations used here are fewer than the earlier study  
 1115 for the 2015 Illapel earthquake (station increased markedly after the 2010 earthquake), and they  
 1116 concentrate near the epicenter.



1117  
 1118 **Figure 28.** 3D tomography results of electron density anomalies 1 minute before the 2010 Maule  
 1119 earthquake (a). I also show the east-west (b) and north-south (c) profiles. Yellow stars show the  
 1120 latitude and longitude of the epicenter. White circles in (c) show selected positions used to draw  
 1121 Figure 31. The results for other epochs are given in Figure 29.



1122

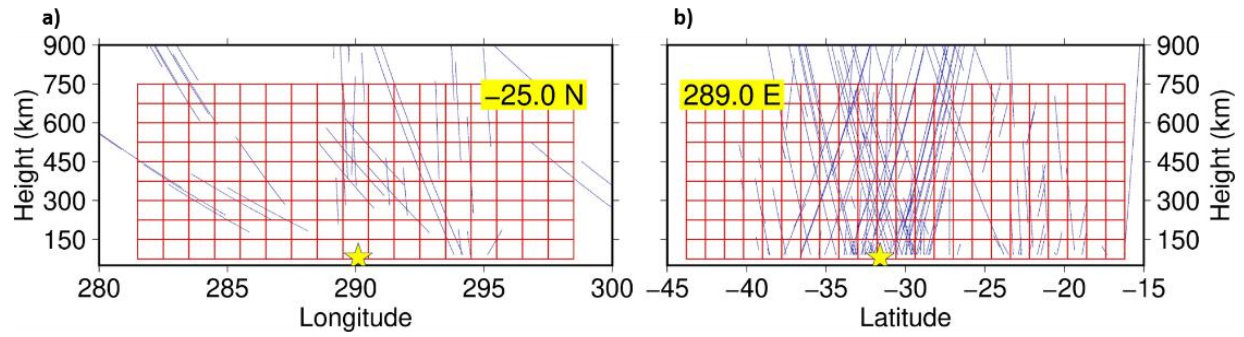
1123

1124

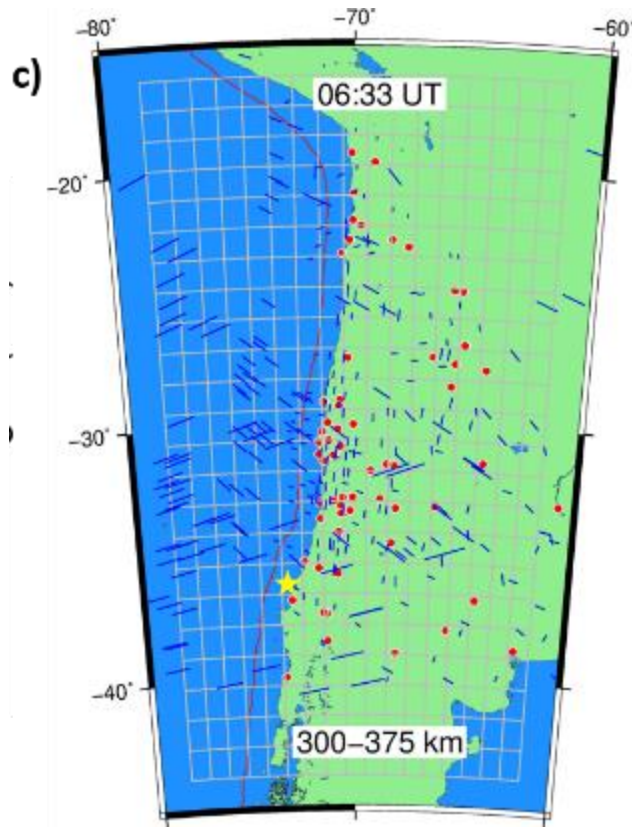
**Figure 29.** 3D tomography results of electron density anomalies from 75-750 km altitudes at three epochs, 40, 22, and 1 minute before the 2010 Maule earthquake.

1125

1126



1127

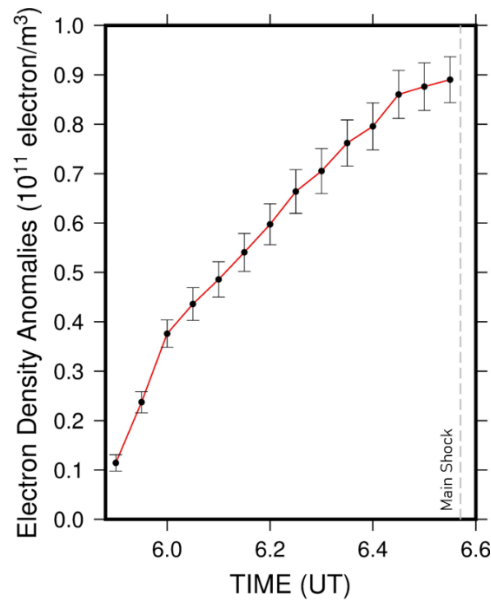


1128

1129 **Figure 30.** For vertical walls running east-west (a) and north-south (b) with the thickness of one  
 1130 block, the LoS penetrating those walls are plotted with blue lines. Blue short lines in the map (c)  
 1131 indicate the LoS of satellite-station pairs at the altitude 300-375 km (one layer of voxels) one  
 1132 minute before the earthquake. Sparseness of the data can be confirmed by comparing with Figures  
 1133 10 and 15 for the 2011 Tohoku-oki case.

1134

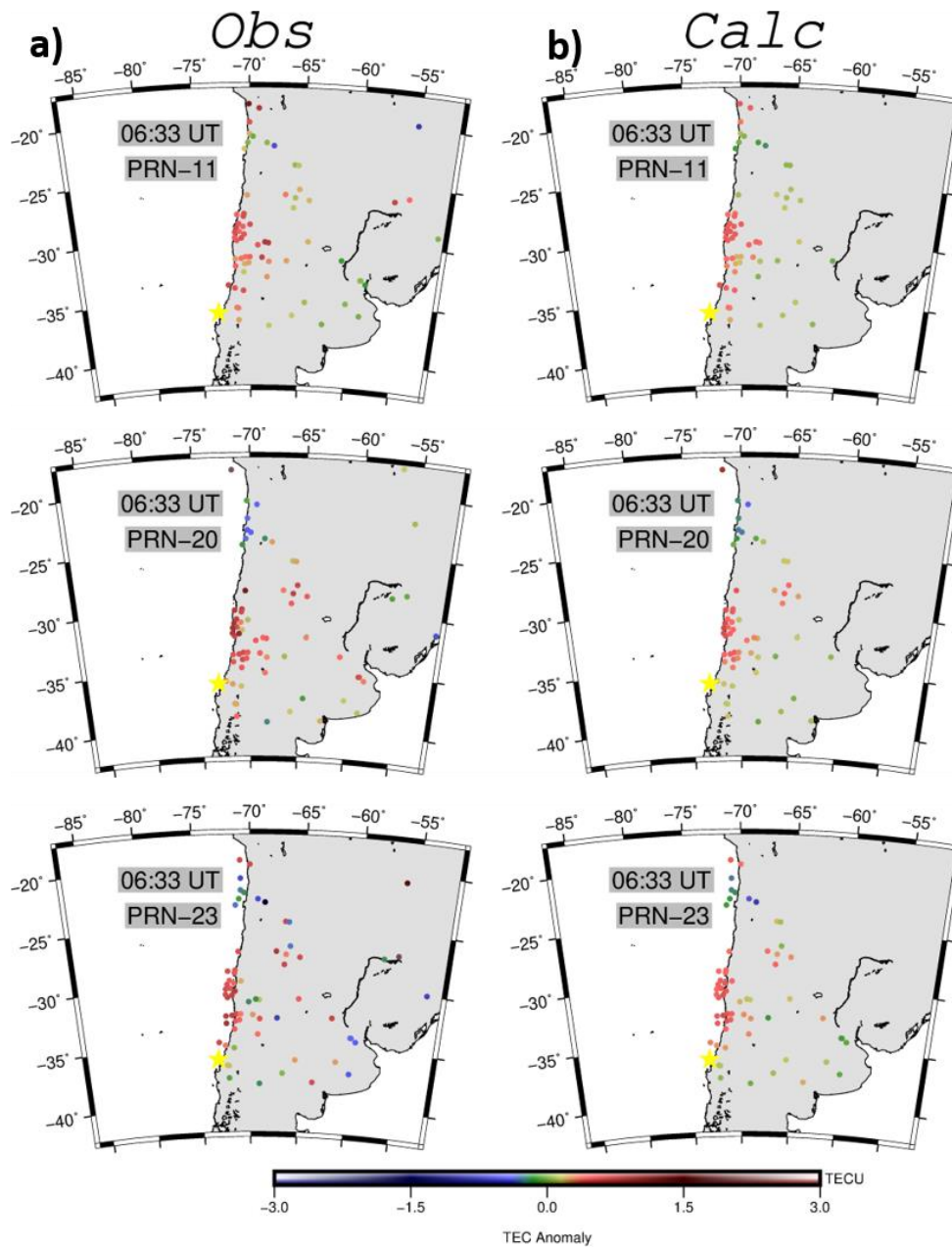
1135 In Figure 31, I plot the average estimated positive electron density anomalies of the three  
1136 different blocks at the altitudes of 300-375 km using 3D tomography result in Figure 28. This  
1137 corresponds to Figure 22 in the 2011 Tohoku-oki case. I could see the smooth growth of the  
1138 positive anomaly from 40 to 1 minutes, around 5.9-6.5 UT, before the mainshock. Unlike Figure  
1139 22, I did not include the growth curve for the negative anomalies. This is because the negative  
1140 anomalies at high altitudes are hard to identify due to unfavorable distribution of the available LoS  
1141 (Figure 30).



1142  
1143 **Figure 31.** The growth of the average values of positive electron density anomalies at the three  
1144 different blocks at the altitude of 300-375 km before the 2010 Maule earthquake. The error bars  
1145 show the standard deviation around the average of the 7 voxels. The positions of the 7 voxels are  
1146 indicated with white dots in Figure 28c.

1147  
1148 Figure 32 compares the observed and calculated anomalies for four satellites, 11, 20, and  
1149 23 at the epoch 1 minute before the main shock. The “observed” anomalies (Figure 32a) are those  
1150 obtained as the departure from the reference curves to VTEC time series, and I plotted them at  
80

1151 their SIP. On the other hand, the “calculated” anomalies (Figure 32b) were derived as the sum of  
1152 the products of the estimated electron density anomalies (Figure 28) and the penetration lengths of  
1153 voxels along the LoS. Such calculated STEC anomalies are converted to VTEC for comparison  
1154 with the observed anomalies. These two are expected to nearly coincide if the 3D tomography  
1155 inversion is successful. We can see that the observed TEC anomalies are well reproduced by the  
1156 estimated 3D electron density anomalies shown in Figure 28.



1157

1158 **Figure 32.** Comparison of the observed (a) and calculated (b) VTEC anomalies for three GPS  
 1159 satellites at the epoch at 06:33 UT, 1 minute before the earthquake. They are mostly consistent  
 1160 with each other demonstrating that the estimated 3D electron density anomaly structure well  
 1161 explains the observed TEC changes

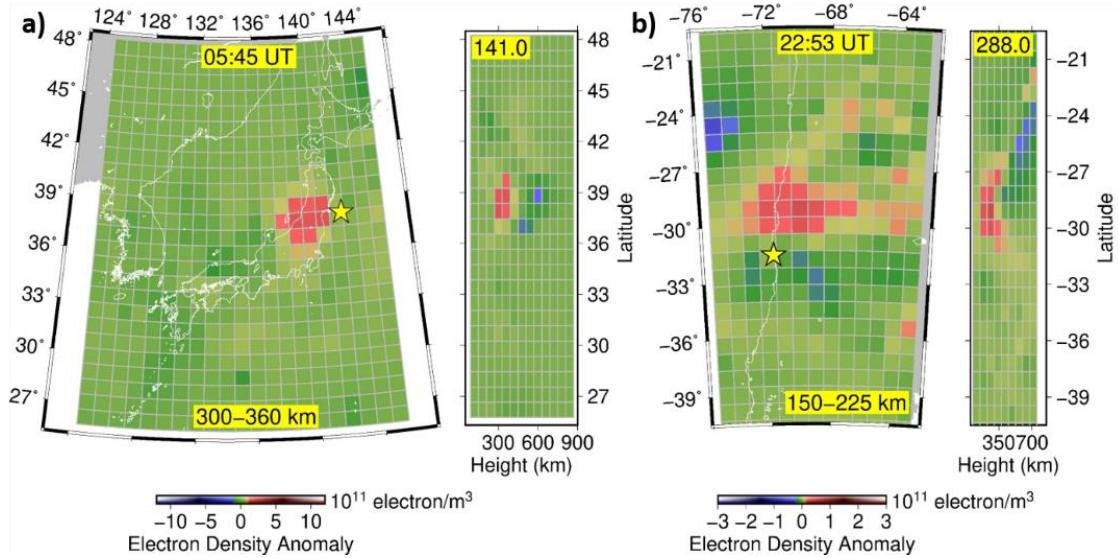
#### 1162 **4.6 Comparison with the 2011 Tohoku-oki and 2015 Illapel Earthquakes**

1163 Now, there are three examples of the 3D distributions of ionospheric electron density  
1164 anomalies immediately before large earthquakes, i.e. 2011 Tohoku-oki ( $M_w$  9.0, this thesis), 2015  
1165 Illapel ( $M_w$  8.3, He and Heki, 2018) and 2010 Maule earthquake (this thesis). They are compared  
1166 in Figure 33. At a glance, we could see their similarities. They are composed of low-altitude  
1167 positive anomalies and high-altitude negative anomalies. This does not apply for the 2010 Maule  
1168 earthquake, but it is due to insufficient coverage of LoS in the region (Figure 27). Regarding the  
1169 intensity of the anomaly, they largely differ (the two cases are drawn with different color palettes  
1170 in Figure 33), i.e., the positive anomalies of the 2011 Tohoku-oki are  $\sim 7$  times as strong as those  
1171 of the 2015 earthquake. This would possibly reflect the difference in their magnitudes,  $M_w$ 9.0 and  
1172 8.3, respectively.

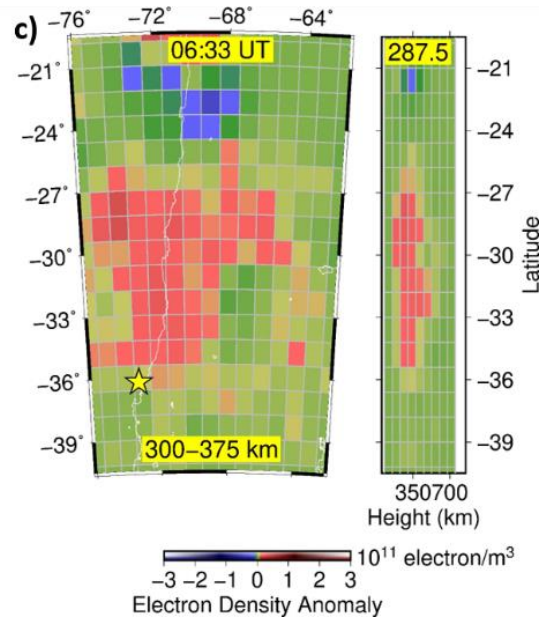
1173 The 2010 Maule earthquake has slightly stronger preseismic anomalies than the 2015  
1174 Illapel event ( $M_w$ 8.3), although its magnitude ( $M_w$ 8.8) is more similar to the 2011 Tohoku  
1175 earthquake ( $M_w$ 9.0). It might be because the background VTEC is low during the 2010 Maule  
1176 earthquake, which occurred very early in the morning (03:34 AM in local time). Smaller amount  
1177 of the original ionospheric electron density would result in smaller anomalies. Here I compare  
1178 them using the ratios of the anomalies observed as GPS-TEC to the background values using three  
1179 station-satellite pairs for each case. I found the ratio is  $9.2 \pm 0.74\%$  for 2010 Maule Earthquake,  
1180  $9.63 \pm 1.91\%$  for 2011 Tohoku Earthquake, and  $6.0 \pm 0.61\%$  for 2015 Illapel Earthquake. These  
1181 results suggest that the intensity of ionospheric anomalies depends on earthquake magnitudes.  
1182 Such  $M_w$  dependences are also seen in the leading times and the intensities of the initial bending  
1183 of the VTEC curves (Heki and Enomoto, 2015; He and Heki, 2017).

1184           As for the altitude where the anomalies appeared, their vertical profiles suggest that the  
1185 altitudes of the positive and negative anomalies before the 2011 earthquake (~300 and ~600 km)  
1186 are somewhat higher than the 2015 earthquake (~200 and ~500 km). The altitude of the positive  
1187 anomaly before the 2010 Maule earthquake is similar to that of the 2011 earthquake (~300 km).  
1188 Hence, it seems that the 3D structure of the anomalies spatially expands for earthquakes with larger  
1189 magnitudes.

1190           On the other hand, horizontal extents of the anomalies before the 2011 and 2015  
1191 earthquakes are little different in the three cases, i.e. the positive anomalies lie within circles with  
1192 diameter of ~300 km for 2011 Tohoku earthquake. The horizontal extent of the positive anomalies  
1193 before 2010 Maule ( $M_w$ 8.8) is much larger than the anomalies before 2015 Illapel ( $M_w$ 8.3). The  
1194 difference is almost twice in north-south and east-west dimensions (Figure 33b,c). It suggests that  
1195 magnitudes control the size of the anomaly if other conditions are similar. As I discussed in the  
1196 previous chapter, the strong positive anomalies of the 2011 Tohoku-oki earthquake did not occur  
1197 directly above the epicenter but emerged above land. This suggests that the electron redistribution  
1198 is due to electric fields made by surface electric charges. Such surface charges would be relatively  
1199 stable on land, but they diffuse rapidly in the ocean due to high electric conductivity of sea water.  
1200 Horizontal extent of the anomaly before the 2011 Tohoku-oki earthquake might have been limited  
1201 by the land-sea distribution in the Japanese Islands, i.e. the anomaly may have expanded larger if  
1202 NE Japan was a continental arc like Chile.



1203



1204

1205 **Figure 33.** The estimated 3D distributions of ionospheric electron density anomalies prior to the  
 1206 2011 Tohoku-oki earthquake (this thesis) (a), the 2015 Illapel earthquake (He and Heki, 2018) (b),  
 1207 and the 2010 Maule earthquake (this thesis) (c), drawn with the similar spatial scales. Each case is  
 1208 composed of two panels showing the plan view and the north-south profile at the longitude  
 1209 crossing the anomaly. (a) and (b,c) use different colour palettes, and the anomalies in (a) are ~7  
 1210 times as strong as in (b). The anomalies in (c) has larger horizontal extent than in (b) suggesting  
 1211 magnitude also controls the size of the anomaly if ambient land-ocean geometry is similar. The  
 1212 yellow stars are the epicenters of the three events.

1213 **Chapter 5: 3D Tomography of the Ionospheric Anomalies after Earthquakes:**

1214 **The 2011 Tohoku-oki Earthquake**

1215

1216 *The content of this chapter was published in Journal Geophysical Research Space Physics, Muafiry, I.N.and K. Heki, 3D*

1217 *tomography of the ionospheric anomalies immediately before and after the 2011 Tohoku-oki ( $M_w$ 9.0) earthquake, J. Geophys. Res.*

1218 *Space Phys., 125, e2020JA027993, doi:10.1029/2020JA027993, 2020*

1219

## 1220 **5.1 Introduction: Tsunamigenic ionospheric anomalies**

1221 Ionospheric electron density drops (formation of the tsunami hole) are considered to occur  
1222 right above the fault following the arrival of acoustic waves at the ionospheric F region ~10  
1223 minutes after the 2011 Tohoku-oki earthquake (Kakinami et al., 2012; Shinagawa et al., 2013;  
1224 Zettergren and Snively, 2019). The physics related to this ionospheric hole is discussed in Chapter  
1225 5.6. Here I estimate the 3D structure of this postseismic anomaly to study its difference in structure  
1226 and in position from the preseismic anomalies. This is expected to serve as a rebuttal to the  
1227 opponents who claim that this hole served as a source of artifact for the preseismic TEC increases  
1228 (Kamogawa and Kakinami, 2013; Masci et al., 2015).

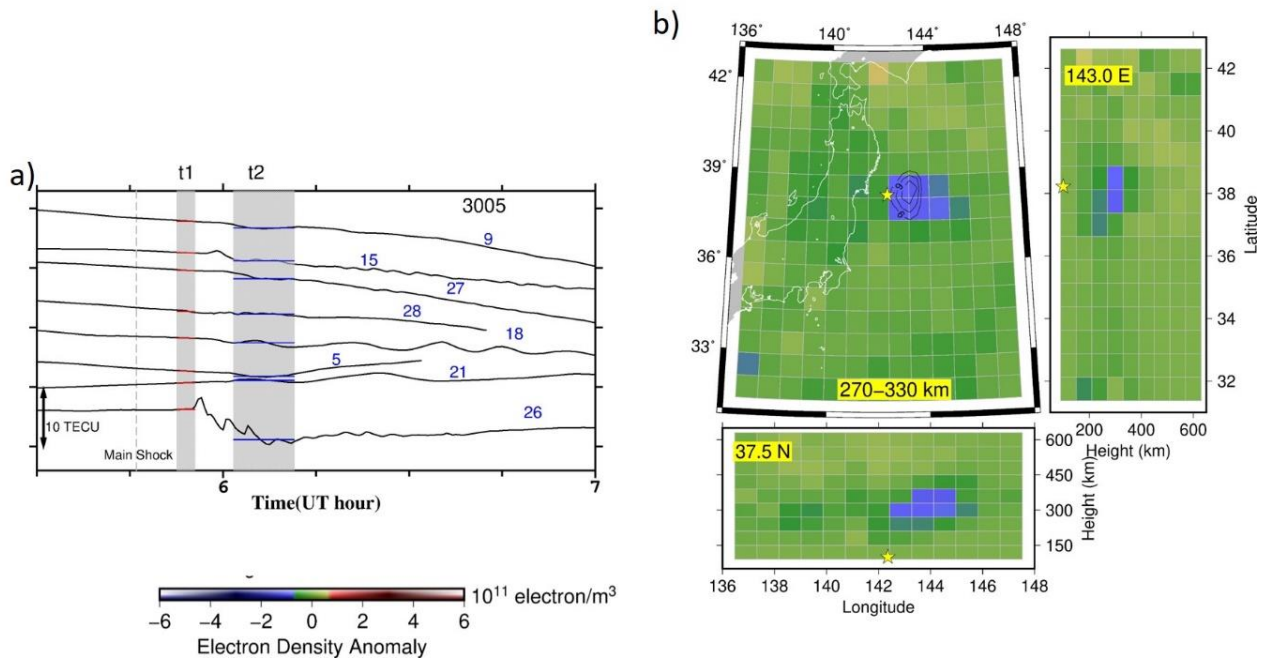
## 1229 **5.2 Data set**

1230 GNSS data from the entire GEONET is used, 1,231 GNSS stations, to study the post-  
1231 seismic anomalies of the 2011 Tohoku-oki earthquake. I used 8 GPS satellites (PRN 05, 09, 15,  
1232 18, 21, 26, 27, 28) visible from the studied region after the mainshock (05:46 UT). Unfortunately,  
1233 GEONET did not track GNSS other than GPS in 2011. See also Chapter 2 for the detail of the  
1234 input data. I did not use the GNSS data from Korea because of the remoteness of the Korean GNSS  
1235 stations from the anomalies to the east of Honshu.

## 1236 **5.3 Data processing strategy**

1237 In Chapter 2.5, I explained two strategies to isolated TEC anomalies related to earthquakes.  
1238 The first one is the modelling the temporal change of VTEC as a polynomial of time which is  
1239 determined by least-squares method. The estimated models will serve as reference curves, and  
1240 differences from these curves are defined as the anomalies. The other one is to make the difference

1241 between medians of VTEC from two periods (before and after the start of the anomalies). Here I  
 1242 used the second strategy, i.e., I subtract the VTEC median before the ionospheric hole formation  
 1243 from VTEC after the hole formation to isolate the VTEC changes associated with the generation  
 1244 of the ionospheric hole.



1245 **Figure 34.** (a) VTEC time series of 8 GPS satellites, observed at 3005 in Kanto. The VTEC drops  
 1246 are defined as the difference between the median VTEC values in the two periods (grey rectangles).  
 1247 The flat red and blue lines within the two periods indicate the VTEC medians in the two periods,  
 1248 and I used their differences as the input to the 3D tomography. (b) 3D tomography of the electron  
 1249 depletion induced by the coseismic uplift and subsequent drop of the sea surface after the 2011  
 1250 Tohoku-oki earthquake (yellow stars represent the epicenter). The contours in the plan view show  
 1251 the fault slips in the main shock (the contour interval is 3 meters). Spatially integrated amounts of  
 1252 negative and positive electron number changes are shown in Figure 22b in Chapter 3.  
 1253

1254  
 1255 At first, I get the medians of VTEC from the two periods, i.e. 5:52-5:55 UT and 6:03- 6:11  
 1256 UT (two grey rectangles in Figure 34a), in VTEC time-series of GNSS stations. These periods

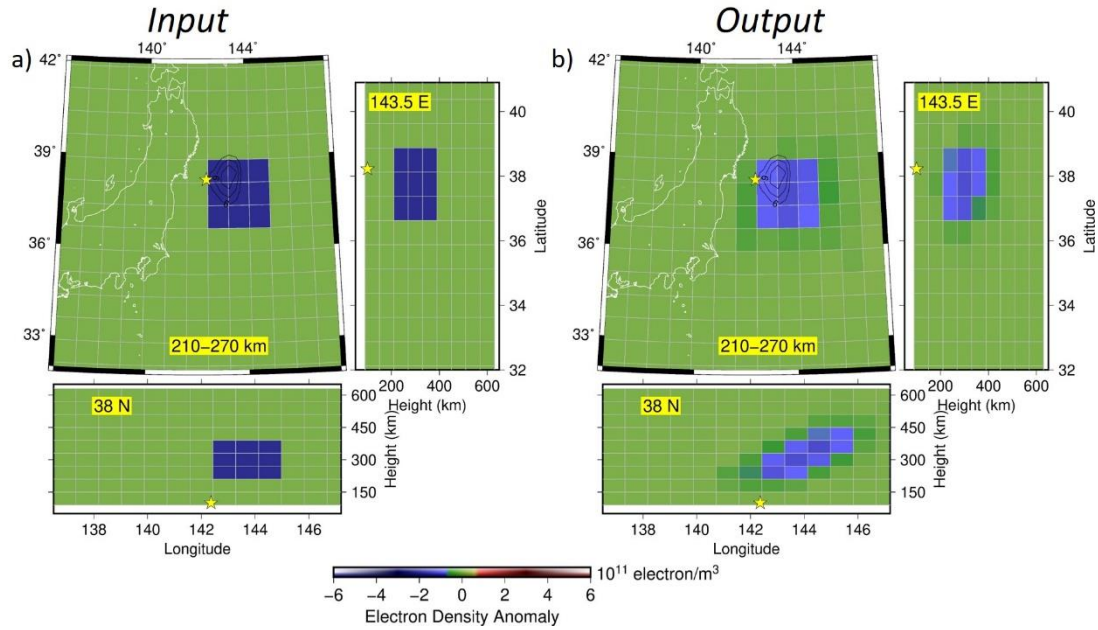
1257 correspond to times immediately before and after the ionospheric hole formation associated with  
1258 the acoustic disturbance arrival. I do not use reference curves because the two periods are separated  
1259 from each other by only ~10 minutes. The longer interval for the time window after the ionospheric  
1260 hole formation was used because of the variety of acoustic disturbances occurring during this time  
1261 window. In this method, we cannot remove the contribution from the long-term TEC decrease due  
1262 to the increasing solar zenith angle. However, it would make a negative bias of the whole region  
1263 and not as a localized anomaly.

1264 I converted the difference of VTEC between the two epochs into STEC and used them as  
1265 the input to our tomography program. I used the satellite positions at 6:00 UT, the time in the  
1266 middle of the two periods. This would not cause a problem because LoS movements during the 10  
1267 minutes period is much less than the voxel size. I applied the same constraints as in the preseismic  
1268 case to regularize the inversion.

#### 1269 **5.4 Resolution tests**

1270 I performed the resolution test, by recovering patterns composed of a negative ( $-3.00 \times$   
1271  $10^{11}$  el/m<sup>3</sup>) anomaly in the F-region above the fault in neutral background (Figure 35a). The 3D  
1272 tomography results (Figure 35b) well reproduced the assumed pattern of the negative anomaly.  
1273 Again, the recovered amplitude was reduced to  $\sim 2/3$  of the input model due to the constraints. In  
1274 the map view, we see only weak smears in surrounding blocks not exceeding a few percent of the  
1275 assumed anomaly. However, significant smears are seen in EW profile (lower panel of the output)  
1276 because the resolution is poor in the direction of LoS connecting the land and the anomaly. The  
1277 results of the two resolution tests show that our 3D tomography results are accurate enough in the

1278 region of interest where the postseismic ionospheric hole appeared after the 2011 Tohoku-oki  
1279 earthquake.



1280

1281 **Figure 35.** The resolution test for a compact negative anomaly off the Pacific coast of NE Japan.  
1282 The upper, bottom, and right panels are horizontal view, latitudinal and longitudinal profiles of the  
1283 anomalies of the assumed pattern (a) and the output of the 3D tomography with synthetic data (b).

1284

## 1285 **5.5 Tomography result**

1286 Figure 34b shows the 3D structure of the recovered electron density anomalies associated  
1287 with the formation of the postseismic ionospheric hole. The main part of the negative electron  
1288 density anomaly lies at height of ~300 km above the tsunami source area (the area of large vertical  
1289 crustal movements). An important point is that they occur offshore just above the area of large  
1290 coseismic slips (contours in Figure 34b), which makes a clear contrast to the preseismic anomalies  
1291 that occurred above land (Figure 17a, Chapter 3). Another important point is that the anomaly is  
1292 composed only of the negative anomalies in contrast to the pair of positive and negative preseismic  
1293 anomalies (Figure 17c Chapter 3). This suggests that the loss of electrons due to their  
1294 recombination with positive ions is the main mechanism for the negative anomaly. Next, I will  
1295 discuss the physical mechanism of the postseismic ionospheric hole based on these 3D tomography  
1296 results.

## 1297 **5.6 Physical mechanism of post-seismic anomalies**

1298 The negative postseismic anomaly extends offshore beyond the large slip region as far as  
1299 ~145E (Figure 34b). However, this is considered be due to the smearing as seen in the resolution  
1300 test (Figure 35). An important point is that the post-seismic anomalies are mainly composed of  
1301 negative changes. This makes a sharp contrast with the preseismic anomalies whose positive and  
1302 negative changes are nearly balanced throughout their growth as shown in Figure 22b in Chapter  
1303 3.

1304 These contrasts would reflect the different physical mechanisms responsible for the pre-  
1305 and postseismic anomalies, i.e. the former is caused by electron transport, but the latter is caused

1306 by the recombination of the electrons displaced downward by the acoustic disturbance as modelled  
1307 by Kakinami et al. (2012) and Shinagawa et al. (2013). We also see that the dimension of the hole  
1308 is consistent with the numerical simulation by Zettergren and Snively (2019).

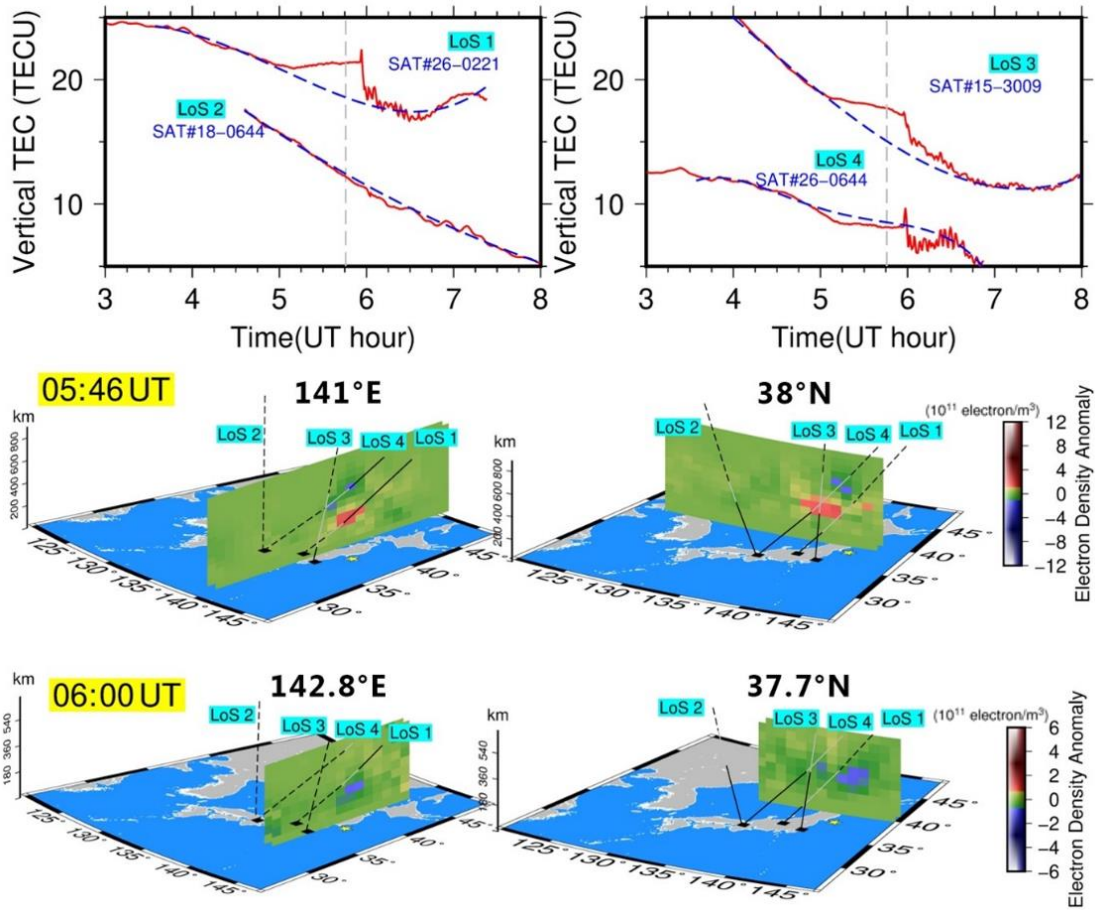
## 1309 **5.7 Origin of variety of waveforms**

1310 In Chapters 3 and 5, I showed two different kinds of anomalies of the ionospheric electron  
1311 density, the preseismic and the postseismic anomalies. Now I identified three electron density  
1312 anomalies different in time and polarity, i.e. #1 the preseismic positive anomaly, #2 the preseismic  
1313 negative anomaly, and #3 the postseismic negative anomaly. #1 and #2 start to grow  
1314 simultaneously at low and high ionosphere ~40 minutes before the earthquake and decay after the  
1315 earthquake, while #3 emerges shortly after the acoustic disturbance arriving 8-10 minutes after the  
1316 earthquake and last for tens of minutes.

1317 Heki (2011) noticed diversity of signatures of TEC disturbances related to earthquakes. For  
1318 example, some LoS show only gradual growth and decay of positive signals (e.g. Sat.15- 3009  
1319 shown in Figure 11a) while other LoS show sudden decrease after the acoustic disturbances (e.g.  
1320 Sat.26-0946 shown in Figure 11b). On the other hand, some LoS, like the cyan time series in Figure  
1321 11 top, show negative changes during the preseismic period. These varieties reflect the difference  
1322 in the penetration of those LoS with the anomalies #1, #2, and #3. For example, Sat.15-3009  
1323 penetrated only #1, while Sat.26-0946 penetrated both #2 and #3.

1324 Figure 36 explains the variety of waveforms of VTEC changes before and after the  
1325 earthquake coming from the diversity in the penetrations of LoS with these three anomalies. There  
1326 are four typical VTEC signatures observed in different satellite-station pairs, (1) LoS penetrating

1327 both the preseismic positive and postseismic negative anomalies, (2) LoS without penetrating any  
 1328 anomalies, (3) LoS penetrating only preseismic positive, and (4) LoS penetrating only the  
 1329 postseismic negative anomalies. In Figure 36, I also show tomography profile before and after the  
 1330 earthquake and how the four LoS penetrate them. The VTEC time series are shown on top.



1331  
 1332 **Figure 36.** The 4 types of VTEC waveforms from different station-satellite pairs (upper panels),  
 1333 LoS 1 (Sa.26-0221) penetrating both the preseismic positive and postseismic negative anomalies,  
 1334 LoS 2 (Sat.18-0644) without penetrating any anomalies, LoS 3 (Sat.15-3009) penetrating only  
 1335 preseismic positive anomaly, and LoS 4 (Sat.26-0644) penetrating only the postseismic negative  
 1336 anomaly. Bottom panels are the 3D tomography result of preseismic and postseismic anomalies  
 1337 overlain with the LoS of the four examples. Black and grey lines indicate LoS in front of and  
 1338 within the profile (one block thick). Black dashed lines correspond to the LoS behind the profile.

## 1340 **Chapter 6: Conclusions and Recommendation**

### 1341 **6.1 Conclusions**

1342 I studied the 3D structure of the ionospheric electron density anomalies immediately before  
1343 the 2011 Tohoku-oki ( $M_w$  9.0) and 2010 Maule ( $M_w$  8.8) earthquakes by using GNSS-TEC data  
1344 taken in Japan, South Korea, and South America in order to contribute to the understanding of the  
1345 physical processes responsible for the preseismic ionospheric anomalies found by Heki (2011).

1346 I paid special attention to the detail of the method to obtain the TEC anomalies as the input  
1347 to the 3D tomographic inversion program. I optimized the polynomial degrees for the reference  
1348 curves using the L-curve method. The exclusion windows were set up to estimate the reference  
1349 curves without being influenced by ionospheric disturbances due to earthquakes. The start of the  
1350 window was defined by the positive bending of the TEC time series detected by statistical  
1351 techniques in an earlier study (Heki and Enomoto, 2015). The end of the window was selected  
1352 carefully to avoid the interference from the postseismic ionospheric hole.

1353 The linear inversion is stabilized by continuity and altitude-dependent constraints, and the  
1354 performance of the method was confirmed by trying 3D tomography to artificial patterns, a  
1355 classical checkerboard pattern and a realistic pattern of a pair of positive and negative anomalies.  
1356 The tests showed that I can resolve electron density anomalies in the ionosphere above regions  
1357 with enough number of ground stations. However, it is not expected that we can identify the upper  
1358 negative anomaly before the 2010 Maule earthquake.

1359 The 3D tomography results of the two cases, together with another study for the 2015  
1360 Illapel earthquake (He and Heki, 2018), showed that the preseismic ionospheric anomaly has

1361 following similarities; (1) They are composed of pairs of low-altitude positive and high-altitude  
1362 negative (not detected for the 2010 Maule earthquake due to limited LoS distribution) electron  
1363 density anomalies. (2) They occur above the land area close to the submarine faults. (3) They have  
1364 clear onsets a few tens of minutes before earthquakes (~40 min before 2011 Tohoku-oki, and  
1365 Maule, and ~20 minutes before the Illapel earthquakes) and grow with decaying rates.

1366 I compared strengths of the electron density anomalies before these three earthquakes. For  
1367 example, the positive electron density anomalies before the 2011 Tohoku-oki case was seven times  
1368 as strong as that for the 2015 Illapel case. The strength of the preseismic anomalies was also found  
1369 to be controlled by the background electron density on the earthquake days. For example, the  
1370 positive electron density anomaly before the 2010 Maule earthquake was only as strong as in the  
1371 2015 Illapel case. This might be due to smaller electron density in the 2010 earthquake that  
1372 occurred after the midnight.

1373 I also compared the dimensions of the electron density anomalies before these three  
1374 earthquakes. The 2011 earthquake showed positive anomalies lying above the land, and not above  
1375 the submarine epicenter. On the other hand, the 2010 Maule and 2015 Illapel earthquakes showed  
1376 positive anomalies located above the coast (i.e. both above land and above ocean close to the  
1377 coast). This means that the anomaly partly smears out to the ocean, but it is difficult to tell if it  
1378 comes from inadequate density and distribution of the ground GNSS stations. The areal extent of  
1379 the anomaly before the 2015 case was similar to the 2011 case. This would be due to the different  
1380 situation of land-ocean distribution for the two cases, e.g., the land area is limited in NE Japan, an  
1381 island arc, in the 2011 Tohoku-oki case. The 2010 Maule earthquake showed the largest horizontal  
1382 extent. This might reflect a larger proportion of land in a continental arc like Chile.

1383 I presented the model for the physical process of the preseismic ionospheric anomalies  
1384 consistent with such 3D structure proposed in Muafiry and Heki (2020). Micro-scale cracks and  
1385 dislocations could mobilize positive electric charges shortly before large earthquakes. They would  
1386 concentrate near the land surface and generate upward electric fields. The field would then reach  
1387 the ionosphere and generates electromotive forces to make electrons move down along the  
1388 geomagnetic fields. This would continue until the induced downward electric field cancels the  
1389 upward fields due to crustal electric charges, making the electric potential uniform along the  
1390 magnetic field.

1391 The current will depend on the along-B component of the external electric field and the  
1392 density of free electrons as a function of altitude. The nonuniform electric currents would result in  
1393 convergence/divergence of electrons and make positive/negative electron density anomalies at the  
1394 lower/higher ionosphere along the magnetic field, the structure consistent with those found for  
1395 these three earthquakes by 3D tomography. This upward current (downward electron migration)  
1396 would also make eastward/westward magnetic field in regions to the south/north of the epicenter  
1397 before earthquakes in northern/southern hemisphere.

1398 I also studied the 3D structure of the postseismic anomalies of 2011 Tohoku-oki earthquake  
1399 and found that the negative electron density anomaly emerged offshore just above the submarine  
1400 fault. Variety of TEC change patterns observed before and after the 2011 Tohoku-oki earthquake  
1401 is understood by different combinations of the penetrations of LoS with such electron density  
1402 anomalies.

1403 **6.2 Recommendation**

1404 1. There are variety of features of scientific importance in the ionosphere. Conventional  
1405 sensors, such as satellite in-situ observations and ionosondes, used to require a lot of efforts and  
1406 resources to observe ionosphere. Recent launch of GNSS satellite and deployment of ground  
1407 networks of continuous GNSS receivers made such studies much easier for everyone to start. Such  
1408 ionospheric studies using GNSS data are especially suitable for university laboratories with limited  
1409 human and financial resources.

1410 2. In comparison with the analysis of total electron content (TEC) along line-of-sights  
1411 (LoS), 3D tomography provides a robust way to study the 3D structure of various ionospheric  
1412 disturbances. The targets of 3D tomography are not limited to those related to surface phenomena  
1413 such as earthquakes. It can be applied for various space weather phenomena including various  
1414 traveling ionospheric disturbances and sporadic-E irregularities. 3D tomography technique gives  
1415 opportunity for human to understand the earth's upper atmosphere better.

1416 3. Ionospheric anomalies occurring immediately before large earthquake, found by Heki  
1417 (2011), can become a key phenomenon toward practical earthquake prediction and mitigation of  
1418 earthquake disasters in the future. 3D tomography for the electron density anomalies for such  
1419 phenomena provides important insight into the physical processes responsible for them. Based on  
1420 the 3D structure of the preseismic ionospheric anomalies, I proposed one such model assuming  
1421 that surface electric charge redistribute ionospheric electrons through electric fields. In the future,  
1422 detailed observations of the ground electric charges might give a conclusive evidence for the  
1423 validity of such models.

1424 4. Regarding the practical aspect, sophisticated statistical techniques would be necessary  
1425 to detect preseismic ionospheric anomalies as discussed in this thesis, together with automated  
1426 real-time analyses of GNSS-TEC data to establish operational early warning system of large  
1427 earthquakes.

1428

1429

1430 **References**

- 1431 Astafyeva, E. and K. Heki (2009), Dependence of waveform of near-field coseismic ionospheric  
1432 disturbances on focal mechanisms, *Earth Planet. Space*, *61*, 939-943.
- 1433 Astafyeva, E., K. Heki, V. Kiryushkin, E. Afraimovich, S. Shalimov (2009), Two-mode long-  
1434 distance propagation of coseismic ionosphere disturbances, *J. Geophys. Res.*, *114*, A10307,  
1435 doi:10.1029/2008JA013853.
- 1436 Astafyeva, E., P. Lognonné, and L. Rolland (2011), First ionospheric images of the seismic fault  
1437 slip on the example of the Tohoku-oki earthquake, *Geophys. Res. Lett.*, *38*, L22104.  
1438 [doi:10.1029/2011GL049623](https://doi.org/10.1029/2011GL049623)
- 1439 Astafyeva, E. and K. Shults (2019), Ionospheric GNSS imagery of seismic source: Possibilities,  
1440 difficulties, and challenges, *J. Geophys. Res. Space Phys.*, *124*, 534-543.  
1441 doi:10.1029/2018JA026107.
- 1442 Austen JR, Franke J, Liu CH (1988) Ionospheric imaging using computerized tomography. *Radio*  
1443 *Sci.*, *23*:299–307, doi:10.1029/RS023i003p00299
- 1444 Cahyadi, M. N., and K. Heki (2015), Coseismic ionospheric disturbance of the large strike-slip  
1445 earthquakes in North Sumatra in 2012:  $M_w$  dependence of the disturbance amplitudes, *Geophys.*  
1446 *J. Int.*, *200(1)*, 116-129, doi:10.1093/gji/ggu343.
- 1447 Calais, E. and J. B. Minster (1995), GPS detection of ionospheric perturbations following the  
1448 January 17, 1994, Northridge earthquake, *Geophys. Res. Lett.*, *22*, 1045–1048,  
1449 doi:10.1029/95GL00168.

- 1450 Chen, C. H. A. Saito, C. H. Lin, M. Yamamoto, S. Suzuki, G. K. Seemala (2016), Medium-scale  
1451 traveling ionospheric disturbances by three-dimensional ionospheric GPS tomography, *Earth,*  
1452 *Planets and Space*, 68:32, DOI 10.1186/s40623-016-0412-6
- 1453 Choi, B.-K., and J. Hong (2019), Observation of the fast-traveling ionospheric disturbances  
1454 induced by the 2017 North Korean missile, *Adv. Space Res.*, 63, 2598-2608,  
1455 doi:10.1016/j.asr.2018.12.033.
- 1456 Coster, A., J. Williams, A. Weatherwax, W. Rideout, and D. Herne (2013), Accuracy of GPS total  
1457 electron content: GPS receiver bias temperature dependence. *Radio Science*, 48, 190–196.  
1458 doi:10.1002/rds.20011
- 1459 Freund, F. T. (2011), Pre-earthquake signals: Underlying physical processes. *Journal Asian Earth*  
1460 *Sci.*, 41(4-5), 383–400. [doi:10.1016/j.jseaes.2010.03.009](https://doi.org/10.1016/j.jseaes.2010.03.009)
- 1461 Freund, F. (2013), Earthquake forewarning - A multidisciplinary challenge from the ground up to  
1462 space, *Acta Geophys.*, 6(14), 775-807, doi:10.2478/s11600-013-0130-4.
- 1463 Garcia, R., F. Crespon, V. Ducic, P. Lognonné (2005), Three-dimensional ionospheric tomography  
1464 of post-seismic perturbations produced by the Denali earthquake from GPS data, *Geophys. J.*  
1465 *Int.*, 163, 1049–106, doi: 10.1111/j.1365-246X.2005.02775.x
- 1466 He, L., and Heki, K. (2016). Three-dimensional distribution of ionospheric anomalies prior to three  
1467 large earthquakes in Chile. *Geophys. Res. Lett.*, 43, 7287–7293. doi:10.1002/2016GL069863
- 1468 He, L., and K. Heki (2017), Ionospheric anomalies immediately before  $M_w$  7.0–8.0 earthquakes. *J.*  
1469 *Geophys. Res. Space Phys.*, 122, 8659–8678. [doi:10.1002/2017JA024012](https://doi.org/10.1002/2017JA024012)

1470 He, L., and K. Heki (2018), Three-dimensional tomography of ionospheric anomalies immediately  
1471 before the 2015 Illapel earthquake, Central Chile, *J. Geophys. Res. Space Phys.*, 123, 4015–4025.  
1472 [doi:10.1029/2017JA024871](https://doi.org/10.1029/2017JA024871)

1473 He, L., K. Heki, and L. Wu (2018), Three-dimensional and trans-hemispheric ionospheric electron  
1474 density changes by the great Solar eclipse in North America on 21 August 2017, *Geophys. Res.  
1475 Lett.*, 45, 10,933-10,940, doi:10.1029/2018GL080365.

1476 Heki, K. and J.-S. Ping (2005), Directivity and apparent velocity of the coseismic ionospheric  
1477 disturbances observed with a dense GPS array, *Earth Planet. Sci. Lett.*, 236, 845–855,  
1478 doi:10.1016/j.epsl.2005.06.010.

1479 Heki, K. (2006), Explosion energy of the 2004 eruption of the Asama Volcano, Central Japan,  
1480 inferred from ionospheric disturbances, *Geophys. Res. Lett.*, 33, L14303,  
1481 doi:10.1029/2006GL026249

1482 Heki, K. (2011), Ionospheric electron enhancement preceding the 2011 Tohoku-oki earthquake.  
1483 *Geophys. Res. Lett.*, 38, L17312. doi:10.1029/2011GL047908

1484 Heki, K. and Y. Enomoto (2013), Preseismic ionospheric electron enhancements revisited, *J.  
1485 Geophys. Res.*, 118, 6618-6626, doi:10.1002/jgra.50578.

1486 Heki, K. and Y. Enomoto (2014), Reply to comment by K. Heki and Y. Enomoto on "Preseismic  
1487 ionospheric electron enhancements revisited", *J. Geophys. Res. Space Phys.*, 119,  
1488 doi:10.1002/2014JA020223.

- 1489 Heki, K., and Y. Enomoto (2015),  $M_w$  dependence of the preseismic ionospheric electron  
1490 enhancements. *J. Geophys. Res. Space Phys.*, *120*, 7006–7020, doi:10.1002/2015JA021353.
- 1491 Heki, K. (2021), Chapter 5-3: Ionospheric disturbances related to earthquakes in *Advances in*  
1492 *ionospheric research: Current understanding and challenges*, Wiley/AGU Book Space Physics  
1493 and Aeronomy, Volume 3, edited by C. Huang and G. Lu, pp.320, ISBN:978-1-119-50755-0.
- 1494 Iwata, T. and K. Umeno (2016), Correlation Analysis forpreseismic Total Electron Content  
1495 Anomalies around the 2011 Tohoku-oki Earthquake, *J. Geophys. Res. Space Phys.*, *121*, 8969-  
1496 8984, doi:10.1002/2016JA023036
- 1497 Jara-Munoz, J., D. Melnick, D. Brill, M. R. Strecker (2015), Segmentation of the 2010 Maule  
1498 Chile earthquake rupture from a joint analysis of uplifted marine terraces and seismic-cycle  
1499 deformation patterns, *Quaternary Science Reviews*, *113*:171-192,  
1500 doi:10.1016/j.quascirev.2015.01.005
- 1501 Kakinami, Y., M. Kamogawa, Y. Tanioka, S. Watanabe, A. R. Gusman, J.-Y. Liu, Y. Watanabe,  
1502 and T. Mogi (2012), Tsunamigenic ionospheric hole, *Geophys. Res. Lett.*, *39*, L00G27,  
1503 doi:10.1029/2011GL050159
- 1504 Kamogawa, M., and Y. Kakinami (2013), Is an ionospheric electron enhancement preceding the  
1505 2011 Tohoku-oki earthquake a precursor? *J. Geophys. Res. Space Phys.*, *118*, 1751–1754,  
1506 doi:10.1002/jgra.50118.
- 1507 Kelley, M.C. (2009), *The Earth's Ionosphere: Plasma Physics and Electrodynamics*, Elsevier, 2nd  
1508 ed.

1509 Kelley, M. C., W. E. Swartz, and K. Heki (2017), Apparent ionospheric total electron content  
1510 variations prior to major earthquakes due to electric fields created by tectonic stresses, *J.*  
1511 *Geophys. Res. Space Phys.*, *122*, doi:10.1002/2016JA023601.

1512 Kundu, B., B. Senapati, A. Matsushita, and K. Heki (2021), Atmospheric wave energy of the 2020  
1513 August 4 explosion in Beirut, Lebanon, from ionospheric disturbances, *Sci. Rep.*, *11*, 2793,  
1514 doi:10.1038/s41598-021-82355-5.

1515 Kuo, C. L., L. C. Lee, and J. D. Huba (2014), An improved coupling model for the lithosphere-  
1516 atmosphere-ionosphere system, *J. Geophys. Res. Space Phys.*, *119*, 3189-3205,  
1517 doi:10.1002/2013JA019392.

1518 Kwon, J. (2012), Korea Geodetic Framework for Sustainable Development, Nineteenth United  
1519 Nations Regional Cartographic, Conference for Asia and the Pacific, E/CONF.102/IP.17.

1520 Le, H., Liu, J. Y., and Liu, L. (2011), A statistical analysis of ionospheric anomalies before 736  
1521 M6.0+ earthquakes during 2002–2010. *Journal of Geophysical Research*, *116*, A02303.  
1522 doi:10.1029/2010JA015781

1523 Li, M., and Parrot, M. (2013), Statistical analysis of an ionospheric parameter as a base for  
1524 earthquake prediction. *Journal of Geophysical Research*, *118*, 3731–3739. doi:10.1002/  
1525 jgra.50313

1526 Liu, J.-Y., Y.-B. Tsai, K.-F. Ma, Y.-I. Chen, H.-F. Tsai, C.-H. Lin, M. Kamogawa, C.-P. Lee,  
1527 (2006), Ionospheric GPS total electron content (TEC) disturbances triggered by the 26 December

- 1528 2004 Indian Ocean tsunami. *Journal of Geophysical Research*, *111*, A05303,  
1529 doi:10.1029/2005JA011200
- 1530 Liu, J. Y., Chen, Y. I., Chuo, Y. J., and Tsai, H. F. (2001), Variations of ionospheric total electron  
1531 content during the Chi-Chi earthquake. *Geophysical Research Letters*, *28*, 1383–1386.
- 1532 Masci, F., J. Thomas, F. Villani, J. Secan, and N. Rivera (2015), On the onset of ionospheric  
1533 precursors 40 min before strong earthquakes, *J. Geophys. Res. Space Phys.*, *120*(2), 1383-1393,  
1534 doi:10.1002/2014JA020822.
- 1535 Muafiry, I. N. and K. Heki (2020), 3D tomography of the ionospheric anomalies immediately  
1536 before and after the 2011 Tohoku-oki (Mw9.0) earthquake, *J. Geophys. Res. Space Phys.*, *125*,  
1537 e2020JA027993, doi:10.1029/2020JA027993.
- 1538 Muafiry, I. N., K. Heki, and J. Maeda (2018), 3D tomography of midlatitude sporadic-E in Japan  
1539 from GNSS-TEC data. *Earth, Planets Space*, *70*(1). [doi:10.1186/s40623-018-0815-7](https://doi.org/10.1186/s40623-018-0815-7)
- 1540 Němec, F., Santolik, O., Parrot, M., and Berthelier, J. J. (2008), Spacecraft observations of  
1541 electromagnetic perturbations connected with seismic activity. *Geophysical Research Letters*,  
1542 *35*, L05109. doi:10.1029/2007GL032517
- 1543 Occhipinti, G., P. Lognonné, E. A. Kherani, and H. Hébert (2006), Three-dimensional waveform  
1544 modeling of ionospheric signature induced by the 2004 Sumatra tsunami, *Geophys. Res. Lett.*,  
1545 *33*, L20104, doi:10.1029/2006GL026865.
- 1546 Otsuka Y, Kotake N, Shiokawa K, Ogawa T, Tsugawa T, Saito A (2011), Statistical study of  
1547 medium-scale traveling ionospheric disturbances observed with a GPS receiver network in Japan.

1548 In: *Aeronomy of the earth's atmosphere and ionosphere, IAGA Special Sopron Book Series, vol*  
1549 *2, part 3*, pp 291–299. doi:10.1007/978-94-007-0326-1\_21

1550 Ozawa, S., T. Nishimura, H. Suito, T. Kobayashi, M. Tobita, and T. Imakiire (2011), Coseismic  
1551 and postseismic slip of the 2011 magnitude-9 Tohoku-Oki earthquake. *Nature*, 475, 373-376.  
1552 doi:10.1038/nature10227

1553 Rideout, W., and A. Coster (2006), Automated GPS processing for global total electron content  
1554 data, *GPS Solut.*, 10, 219–228, doi:10.1007/s10291-006-0029-5.

1555 Rolland, L. M., G. Occhipinti, P. Lognonné, A. Loevenbruck (2010), Ionospheric gravity waves  
1556 detected offshore Hawaii after tsunamis, *Geophys. Res. Lett.*, vol. 37, L17101,  
1557 doi:10.1029/2010GL044479.

1558 Rolland, L. M., M. Vergnolle, J.-M. Nocquet, A. Sladen, J.-X. Dessa, F. Tavakoli, H. R. Nankali,  
1559 and F. Cappa (2013), Discriminating the tectonic and non-tectonic contributions in the  
1560 ionospheric signature of the 2011,  $M_w$ 7.1, dip-slip Van earthquake, Eastern Turkey, *Geophys.*  
1561 *Res. Lett.*, 40, 2518–2522, doi:10.1002/grl.50544.

1562 Saito S, S. Suzuki, M. Yamamoto, C.H. Chen, A. Saito (2016), Real-time Ionosphere Monitoring  
1563 by Three-dimensional Tomography Over Japan. In: *Proc. 29th int. tech. meeting, Satellite*  
1564 *Division of the Institute of Navigation (ION GNSS+2016), Portland, Oregon. pp 706–713*

1565 Sakai, T. (2005), Bias error calibrations for observing ionosphere by GPS network, *IEICE Trans.*  
1566 *Comm., J88-B*, 2382-2389. (in Japanese)

- 1567 Seemala G. K., M. Yamamoto, A. Saito, C. H. Chen (2014), Three-dimensional GPS ionospheric  
1568 tomography over Japan using constrained least squares. *J. Geophys Res Space Phys* 119:3044–  
1569 3052. <https://doi.org/10.1002/2013JA019582>
- 1570 Shinagawa, H., T. Tsugawa, M. Matsumura, T. Iyemori, A. Saito, T. Maruyama, H. Jin, M.  
1571 Nishioka, and Y. Otsuka (2013), Two-dimensional simulation of ionospheric variations in the  
1572 vicinity of the epicenter of the Tohoku-oki earthquake on 11 March 2011, *Geophys. Res. Lett.*,  
1573 40, 5009-5013, doi:10.1002/2013GL05762
- 1574 Song, R., K. Hattori, X. Zhang, S. Sanaka (2020), Seismic-ionospheric effects prior to four  
1575 earthquakes in Indonesia detected by the China seismo-electromagnetic satellite, *Journal of*  
1576 *Atmospheric and Solar-Terrestrial Physics* 205, 105291,  
1577 <https://doi.org/10.1016/j.jastp.2020.105291>
- 1578 Tang, J., Y. Yao, L. Zhang, J. Kong (2015), Tomographic reconstruction of ionospheric electron  
1579 density during the storm of 5-6 August 2011 using multi-source data, *Sci. Rep.* 5, 13042, doi:  
1580 10.1038/srep13042
- 1581 Thomas, J.N., Huard, J., and Masci, F. (2017). A statistical study of global ionospheric map total  
1582 electron content changes prior to occurrences of  $M \geq 6.0$  earthquakes during 2000–2014. *Journal*  
1583 *of Geophysical Research*, 122, 2151–2161. doi:10.1002/2016JA023652
- 1584 Tsuji, H., and Hatanaka, Y. (2018). GEONET as Infrastructure for Disaster Mitigation. *J. Disaster*  
1585 *Res.*, 13(3), 424-432.

1586 Utada, H., and H. Shimizu (2014), Comment on “Preseismic ionospheric electron enhancements  
1587 revisited” by K. Heki and Y. Enomoto, *J. Geophys. Res. Space Phys.*, *119*(7), 6011-6015,  
1588 doi:10.1002/2014JA020044.

1589 Zettergren, M. D. and J. B. Snively (2019), Latitude and longitude dependence of ionospheric TEC  
1590 and magnetic perturbations from infrasonic-acoustic waves generated by strong seismic events,  
1591 *Geophys. Res. Lett.*, *46*, 1132–1140, doi:10.1029/2018GL081569.

1592